EVIDENCE FOR MERGER-INDUCED AGN FUELING USING INTEGRAL FIELD SPECTROSCOPY

by

Joshua L. Steffen

A thesis submitted in partial fulfillment of the
requirements for the Doctor of Philosophy
degree in Physics
in the Graduate College of
The University of Iowa

April 2022

Committee: Hai Fu, Thesis Supervisor
Julia M. Comerford
Casey T. DeRoo
Keri Hoadley
Philip Kaaret

Wise he is deemed who can question well,
and also answer back
-Hávamál

ACKNOWLEDGEMENTS

I would like to acknowledge my friends and colleagues; Arran Gross, Dylan Paré, and Sanjay Chepuri whose friendship kept me in good health while writing the thesis. I would also like to acknowledge my advisor, Dr. Hai Fu, whose guidance and support made this thesis possible. Finally, I would like to acknowledge my family, Pamela Bird, Ryan Steffen, and Amanda Steffen, whose love and support I cherish deeply.

ABSTRACT

Hydrodynamical simulations of galaxy mergers have suggested that merger-induced gas-inflows may be able to fuel the central supermassive black hole (SMBH), triggering an active galactic nucleus (AGN). Despite the results of these simulations, observational studies disagree on whether or not there is merger-induced AGN. We use the recently completed integral field spectroscopic (IFS) survey, MaNGA (Mapping Nearby Galaxies at Apache Point Observatory), to study the volume densities and [O III] luminosities of AGN in paired galaxies. We build a sample of 387 spectroscopically confirmed galaxy pairs of which 102 host an AGN and a sample of 24 dual AGN (dAGN). We find that the volume density of AGN in galaxy pairs is higher than what would be expected by the random pairing of stochastically triggered AGN. At close separations, the volume density of AGN in pairs is 2.5× what is expected from the random pairing of AGN. We further find that the volume density of dAGN under separations of 4 kpc is 40× what we would expect from the random pairing of stochastically triggered AGN. We find that neither correlated AGN activity nor merger-induced fueling can fully explain the excess AGN volume density. Instead, we find that a model that includes stochastic fueling, merger-induced fueling, and correlated AGN activity is required to fully explain the excess AGN in our sample of galaxy pairs. We also find that the AGN in our galaxy pairs feature enhanced levels of [O III] luminosity in comparison to the AGN in isolated control galaxies to the order of $0.1-0.4$ dex. The enhanced volume density and [O III] luminosity demonstrates the impact that galaxy interactions have on the development of the supermassive black holes (SMBH) found in the centers of galaxies.

PUBLIC ABSTRACT

Simulations have predicted that the merging of two galaxies should induce gas-inflows which can fuel the central supermassive black hole (SMBH) causing an active galactic nucleus (AGN). Despite the results of these simulations, past observational studies have found conflicting evidence for merger-driven AGN activity in galaxy pairs. I use the recently completed MaNGA (Mapping Nearby Galaxies at Apache Point Observatory) survey to study this phenomena. MaNGA uses bundles of fiber-optic cables to capture the spectra of its targets allowing for spatially resolved data. With this survey, I build a sample of merging and interacting galaxies and a sample of galaxies hosting an AGN. I also build a sample of isolated galaxies since there are also internal processes which may stochastically induced AGN activity. With these samples, I find a higher rate of AGN in our paired galaxies compared to what would be expected from the random pairing of stochastically induced AGN. We also study the [O III] luminosities in these AGN as a tracer of the SMBH's mass accretion rate and find that the AGN in our pairs feature stronger [O III] luminosities than the AGN in isolated galaxies. This gives us strong evidence for merger-driven AGN activity which is in agreement with the predictions of past simulations. These results also demonstrate that galaxy mergers play a significant role in the mass growth of the SMBHs found in the centers of the galaxies in the present universe.

TABLE OF CONTENTS

LIST OF TABLES

Table

LIST OF FIGURES

Figure

CHAPTER 1

INTRODUCTION

1.1 Active Galactic Nuclei

1.1.1 History

Some of the earliest observations of what we now call active galactic nuclei (AGN) happened in the early twentieth century with the detection of unusual emission lines in the centers of galaxies. Seyfert (1943) studied a set of spiral galaxies, still refered to as "spiral nebulae" at the time, which had luminous cores with unusually broad emission lines.

Later on in the 1950's, unknown radio sources were found with star-like objects in the optical regime. The physical origin of these objects were unknown at the time so they were named quasi-stellar objects (QSOs or quasars). Schmidt (1963) collected optical spectroscopy from one of these quasars, 3C 273, and noted that the source had a strong blue continuum, broadened emission lines, and a redshift of 0.158 which indicated that the source was extragalactic. These results were accompanied by the works of Greenstein (1963), Hazard, Mackey, and Shimmins (1963), and Oke (1963), who also studied the quasars 3C 272 and 3C 48 and were published in the same issue of *Nature*.

For some time, the physical mechanism behind these observations remained unknown. Many theories were presented from supernovae chain reactions (Burbidge, 1961) to supermassive stars, $\sim 10^8$ $M_\odot$ (Hoyle and Fowler, 1963a; Hoyle and Fowler, 1963b). The basic model for the energy production in AGN was originally presented in Salpeter (1964) and Zeldovich (1964). Here the energy source is from matter accreting onto a massive compact object in the centers of these galaxies. This would be later supported by the work,

Lynden-Bell (1969), which showed that most galaxies should host a supermassive black hole (SMBH) in their center and that these objects may be responsible for high energy activities like quasars and Seyferts. More recent works have supported that idea that most if not all massive galaxies today possess a SMBH in their centers (Magorrian et al., 1998; Kormendy and Kennicutt, 2004).

1.1.2 Unified Model of AGN

AGN feature strong emission across the whole electromagnetic spectrum from radio to gamma rays. The emission in each of these spectral regions highlights different processes which happen in the region around the accreting black hole. Differences in observed spectral features have led astronomers to create several subcategories of AGN. One of the goals of AGN studies has been to create a "unified model" of AGN in which many of the AGN subcategories that we observe can be reduced down to a handful of physical scenarios (Antonucci, 1993; Ho, 2008; Heckman and Best, 2014).

The review article of Heckman and Best (2014) presents of model of radiative AGN in which there are several regions which are responsible for different spectral features. First is the accretion disk around the black hole. The size of the accretion disk depends on the mass of the black hole, but they are typically the size of our solar system ($\sim 5 \times 10^{-6}$ parsecs). This accretion disk is the driving mechanism for the large amounts of energy expended by the AGN and is directly responsible for the strong ultraviolet continuum, known as the "Big Blue Bump." Further out is the the dusty torus which is also orbiting the black hole but at a larger radii than the accretion disk. The dusty torus is optically thick and reprocesses the UV light from the accretion disk into infrared light through thermal emission.

Within the dusty torus, there is the broad-line region which consists of gases orbiting at high velocities due to their close distance to the black hole. These gases are photoionized by the UV photons produced in the accretion disk and emit strong optical emission lines. Due to the high gas velocities, the emission lines show broadened line profiles. Further from the black hole is the narrow-line region which can extend out to 100 parsecs from the SMBH. This region also contains photoionized gases; however, the gases lack the high velocities of the broad-line regions. As a result, the emission lines from this region are narrow in opposition to the broad-line region. The difference between seeing a narrow-line AGN (Type II Seyfert) and a broad-line AGN (Type I Seyfert) depends on the orientation of the torus with respect to the observer. When broad-lines are seen, the observer is looking down the dusty torus and witnessing the high velocity gases tucked inside the torus. When only narrow-lines are seen, the optically thick torus is obscuring the broad-line region from the observer.

Some AGN show collimated radio jets, which propagate away from the black hole. Here, electrons are being accelerated off of the accretion disk and collimated by the black hole's magnetic field. The electrons spiral around and along the magnetic field lines with relativistic velocities and as a result emit synchrotron radiation in the radio regime. At the radio wavelengths, the jet, a radio core, and in some cases radio "lobes" at the end of radio jets can be seen. AGN can be split into two categories by their radio emission; radio-quiet and radio-loud. Radio-quiet AGN have weak radio emission relative to their optical emission and radio-load AGN have strong radio emission relative to their optical emission.

Finally, X-ray emission can also be seen in AGN. The X-ray emission may be caused by the Inverse-Compton scattering of photons in the corona of hot particles around the accretion

disk (Liang and Price, 1977). These high energy X-ray photons are able to penetrate through the surrounding optically thick Strömgren sphere and ionize forbidden lines in the diffuse partially ionized zone. These forbidden lines play an important role in distinguishing between regions ionized by AGN from those ionized by OB stars.

1.1.3 AGN Fueling

Now that we have discussed the mechanics of the AGN's central engine, we want to understand how that engine receives the necessary fuel to operate. Transporting material from the disk to the center of a galaxy is no easy matter and requires massive reductions in the angular momentum of the material. There are a number of proposed mechanisms for transporting material into the innermost parsecs of a galaxy. These theories include bars, oval distortions, and spiral arms (Kormendy and Kennicutt, 2004; Athanassoula, 2008; Sellwood, 2014); however, there is still little observational evidence for these theories. Studies using SDSS (Sloan Digital Sky Survey) have shown that there is no correlation between AGN activity and the presence of barred structures (Lee et al., 2012; Cisternas et al., 2013); however, there is evidence for a correlation between galaxy pseudobulges (disk-like bulges) and AGN activity (Malkan, Gorjian, and Tam, 1998; Kormendy and Ho, 2013). It has been suggested that these pseudobulges are a consequence of the secular evolution induced by spiral arms or bars (Kormendy and Kennicutt, 2004; Athanassoula, 2005; Athanassoula, 2008). Jogee (2006) suggests that asymmetries like bars and spirals may be able to transport material down to a few 100 parsecs but that other processes are still needed to move that material down to the inner few parsecs of the galaxy. This suggests that the process of random, or stochastic, AGN fueling in isolated galaxies is dependent on a number of iterative

processes.

There are also external processes in the form of galaxy interaction and mergers which may also be able to transport material into a galaxy's central region (Barnes and Hernquist, 1996; Mihos and Hernquist, 1996). This process will be explored in more detail in the following sections.

1.2 Galaxy Interactions

1.2.1 Galaxy Evolution

Galaxy-to-galaxy interactions and galaxy mergers play a fundamental role in galaxy evolution. The event that two galaxies collide is not just a random coincidence but a commonplace event during a galaxy's lifetime. This is because galaxies are often tightly clustered with other galaxies. The galaxy merger starts with the merging of the two galaxies' dark matter halos. Due to dynamical friction (Chandrasekhar, 1943), the stellar components of the galaxies in the merged halo lose angular momentum and fall towards the center of the dark matter halo where they interact with each other. Massive galaxies are more susceptible to the effects of dynamical friction and as such they fall into the center of the halo first where they often become a massive central galaxy for a set of smaller satellite galaxies. The dynamical timescale for a merger event to occur is on the order of 1 Gyr, meaning that today's massive galaxies may have undergone multiple merger events over their lifetime. Cosmological hydrodynamical simulations have shown that massive galaxies may have received as much as 60% of their stellar mass through past merger events (Rodriguez-Gomez et al., 2016; Pillepich et al., 2018), demonstrating that galaxy merging plays an essential role in the development of galaxies.

1.2.2 Galaxy Merger Simulations

Hydrodynamical simulations show that when two similar mass galaxies merge, the tidal torques between the two galaxies induce the formation of large stellar bars (Barnes and Hernquist, 1991). The gravitational torques from these bars can drive gases from the disk of the galaxy into the central region of the galaxy. These inflowing gases impact upon the gases already present in the galaxy's center, triggering new star formation (Barnes and Hernquist, 1996; Mihos and Hernquist, 1996; Di Matteo et al., 2007; Scudder et al., 2012; Moreno et al., 2015; Moreno et al., 2021). These gas-inflows are also predicted to bring the relatively metal-poor gases from the disk to the metal-rich nucleus, thereby diluting the metal content of the galaxy's center (Rupke, Kewley, and Chien, 2010; Perez, Michel-Dansac, and Tissera, 2011; Torrey et al., 2012; Scudder et al., 2012).

It has also been speculated that these gas-inflows may be able to make it into the innermost kiloparsec (kpc) of these galaxies to feed the SMBH found there, triggering AGN activity (Kauffmann and Haehnelt, 2000; Hopkins et al., 2006; Hopkins et al., 2008; Capelo et al., 2017). As previously mentioned, the material within 1 kpc still has too much angular momentum to reach the central SMBH and a secondary mechanism is required to funnel the gases down into the central few parsecs of the galaxy. Unfortunately, these simulations are not capable of resolving parsec scale structures, so the process of fueling the central SMBH remains unknown. While these simulations have provided valuable insight on the physical mechanisms within a galaxy while it is interacting with another galaxies, we want to use observational studies to constrain the results of these simulations.

1.2.3 Galaxy Pair Studies with Single-Fiber Spectroscopy

Galaxy pairs have been extensively studied in past observational studies. Large samples of paired galaxies have been assembled using large single-fiber spectroscopic surveys like SDSS. SDSS has taken more than 4 million spectra of galaxies and stars. The survey accomplishes this by drilling holes into targeting plates over the targets it wishes to observe. Optical fibers are plugged into these holes which allows for the light to be moved to a spectrograph on the back of the telescope. This configuration allows the light from each target in the field to be dispersed without overlapping over other targets. Each fiber has a collision radius of 55″ which poses a problem for finding close galaxy pairs in the survey. Fortunately, there is some overlap between tiling plates and there are some repeat observations of some fields. This allows for some galaxy pairs to be found; however, it introduces a selection bias. Pairs with angular separations under 55″ can only be found in these overlapping observations, but pairs with separations above 55″ can be drawn from the full sample. This bias is typically handled by randomly culling some fraction of the pair sample in pairs with angular separations above 55″ (Ellison et al., 2008).

Despite these angular separation limits, pair surveys like those in Ellison et al. (2008) have been able to identify ∼1700 pairs in SDSS. The pairs are selected by searching for galaxies with similar line-of-sight velocities and close projected separations (the distance between two objects assuming that they are at the same redshift). Pair surveys may also set a stellar mass ratio limit so that the galaxies in the pairs have similar stellar masses. Once the pair sample is made, features like the star formation rate, the metallicity, and AGN activity can be inferred from the spectroscopic data.

Studies can estimate the star formation rate (SFR) in a galaxy by measuring the Hα luminosity as a tracer of OB stars in the spectra. Ellison et al. (2008) studies the relative SFR between paired galaxies and isolated control galaxies. The SFR can depend on the stellar masses and redshifts of the galaxies, so Ellison et al. (2008) matches each pair to a set of ∼20 control galaxies with similar stellar masses and redshifts. They find that pairs feature higher SFRs than the control galaxies and that this enhanced SFR increases with closer pair separations. They also find that pairs whose mass ratios are close to 1:1 feature higher SFR enhancements than those with wider mass ratios.

Measuring relative metallicities is more difficult to do in galaxy pair studies. The direct method for measuring the metallicity in a region involves a flux ratio between auroral lines and strong lines as a measurement of the electron temperature in a gas. This works because metals are the main coolants in an HII region. The problem is that auroral lines are often too weak to observe in many extragalactic sources. To work around this limitation, studies often use strong line ratios which are calibrated to metallicities measured with the direct method. The most common strong line method is the R_{23} method which calibrates the ratio between the [O II] and [O III] fluxes to the Hβ flux to measurements using the direct method. Scudder et al. (2012) uses the R_{23} method to study the difference in metallicities between galaxy pairs and control galaxies. The work uses an updated pair sample from Ellison et al. (2008) and uses a pair-control matching method that is also similar to Ellison et al. (2008) except that the control galaxies are also being matched to pairs based on the environment's density. Scudder et al. (2012) finds that paired galaxies have diluted metallicities in comparison to control galaxies and this this dilution increases with closer

separations.

While many past observational studies have confirmed the enhanced star formation and diluted metallicities predicted from simulations, merger-driven AGN activity remains a hotly debated topic. These works compare the fraction of AGN in pairs and compare them to the fraction of AGN in control galaxies. This initially seems simple, but the measurement of the AGN fraction can be highly dependent on the survey's selection biases. Some works have found higher AGN fractions in pairs than in controls (Ellison et al., 2011; Silverman et al., 2011; Ellison et al., 2013; Satyapal et al., 2014), while other works have found no excess of AGN in pairs (Shah et al., 2020; Silva et al., 2021). These discrepancies may be due to a number of reasons including; the pair selection method, the survey's wavelength regime, or how paired galaxies are matched with control galaxies.

Studies often try to study the rate of mass accretion onto the SMBH for the AGN in pairs in comparison to AGN in isolated galaxies. The total luminosity output by the AGN is proportional to the rate of mass accretion onto the black hole. Bolometric luminosities are difficult to calculate for AGN since they emit across the whole electromagnetic spectrum. Instead, surveys use proxies for the bolometric luminosity that allow them to estimate the accretion rate using a single wavelength regime. The [O III] luminosity is linearly proportional to the bolometric luminosity so it is a good proxy for the black hole accretion rate in optical spectroscopic surveys. Studies have found that the AGN in pairs tend to have higher [O III] luminosities compared to the AGN in unpaired galaxies (Liu, Shen, and Strauss, 2012; Ellison et al., 2013; Alonso et al., 2018), suggesting that these AGN in pairs are accreting material at a higher rate than the AGN in isolated galaxies. Surveys have also found that the most

luminous quasars are often in galaxy pairs with clear tidal features (Urrutia, Lacy, and Becker, 2008; Veilleux et al., 2009; Glikman et al., 2015).

1.2.4 Dual AGN in Galaxy Pairs

Hydrodynamical simulations tracing the mass accretion rates onto the SMBH in mergers have also predicted that there should be window of time during the merger in which both cores feature enhanced nuclear activity (Van Wassenhove et al., 2012; Capelo et al., 2017). This window is towards the later stages of the merger, just before the two galaxy begin to coalesce into a single galaxy, and is predicted to be between 1-10 Myr long. This window is very short in terms of astronomical timescales, which means that these objects should be quite rare.

There have been a number of serendipitous discoveries of these dual AGN (dAGN) in observational works (Owen et al., 1985; Moran et al., 1992; Junkkarinen et al., 2001; Komossa et al., 2003; Ballo et al., 2004; Stockton et al., 2004; Rodriguez et al., 2006; Bianchi et al., 2008; Fabbiano et al., 2011; Mazzarella et al., 2012; Secrest et al., 2017). With new large spectroscopic surveys, groups have been able to make systematic surveys for these objects. One such method for finding dAGN in optical spectroscopy is to look for double-peaked [O III] emission lines (Zhou et al., 2004; Wang et al., 2009; Liu et al., 2010; Smith et al., 2010). The idea was that a single-fiber would simultaneously capture the optical spectra from two closely separated AGN in a galaxy pair. This is particularly relevant as simulations predict that dAGN activity is most likely at very close separations. If the two AGN have significantly different line-of-sight velocity differences, the two AGN could be separately resolved in the spectra by dispersing emission lines like [O III] into a double peaked profile.

Followup studies have confirmed that some of these are confirmed dAGN (Comerford et al., 2011; Fu et al., 2012; Liu et al., 2013; Comerford et al., 2013; Comerford et al., 2015; McGurk et al., 2015; Comerford et al., 2018); however, only a small fraction, ∼2%-5%, of these objects have been confirmed to be actual dAGN (Fu et al., 2011; Shen et al., 2011; Comerford et al., 2012; Fu et al., 2012; Müller-Sánchez et al., 2015; Rubinur, Das, and Kharb, 2019). It is likely that a majority of the double-peaked [O III] emission lines observed in the previous studies are either from rotating disks or AGN outflows from the narrow line region as opposed to actual dAGN (Fu et al., 2011; Shen et al., 2011; Fu et al., 2012; Smith et al., 2012; Nevin et al., 2016; Comerford et al., 2018).

These large spectroscopic surveys have allowed for the construction of large samples of paired galaxies. Unfortunately, they also come with biases that are hard to control for, like the spectroscopic incompleteness issue. The double peaked [O III] method used in these surveys have also enabled the discovery of many very close galaxies pairs, but the success rate of the method is still low. The rise of large scale integral field spectroscopic (IFS) surveys may be able to fill in the gaps from the previous generation of single-fiber spectroscopic surveys.

1.3 Integral Field Spectroscopy

These single-fiber and single-slit spectroscopic studies have their limitations. While these methods are good at building very large spectroscopic surveys of objects, like SDSS's spectroscopic survey, they often suffer from fiber collision issue which sets a lower limit on the allowed galaxy pair separation. The use of a single fiber also limits the spatial extent of the survey to the central $1''-1.''5$ radius of the survey's galaxies. This means that the data

is restricted to studying the nucleus of these galaxies and gives us little information on their disks. There is also an issue with maintaining consistent physical aperture sizes between objects as an optical fiber with a fixed aperture size will not cover the same physical portion of a lower redshift galaxy as it will for a higher redshift galaxy. These issues can be resolved with IFS surveys.

IFS surveys employ large bundles of fiber optic cables to perform spectroscopy across a two dimensional spatial area. The fiber bundles allows us to collect spectra for both the centers of the galaxies and their disks, allowing us to study galaxies with increased spatial extent and resolution. The most recent large IFS surveys are SAMI (Sydney-AAO Multi-object Integral-Field) which has observed 3068 galaxies in their final data release (Croom et al., 2021), CALIFA (Calar Alto Legacy Integral Field Area) which has observed ∼200 galaxies in their second data release (García-Benito et al., 2015), and MaNGA (Mapping Nearby Galaxies at Apache Point Observatory) which has finished observing ∼10,000 galaxies in its most recent public data release (DR17, Abdurro'uf et al. (2021)).

These IFS surveys are particularly valuable for galaxy pair studies for a number of reasons. First, the spatially resolved spectroscopy allows us to study very close pairs which may be missed in other single-fiber spectroscopic surveys due to issues like fiber collisions or the survey selection methods. Second, IFS offers us increased spatial extent, allowing us to simultaneously study how the nucleus of a galaxy and its disk is affected by the merger event. Third and finally, the high spatial resolution of the IFUs (Integral Field Units; the bundle of optical fibers) allows us to construct physically based aperture sizes (like a 1 kpc radius aperture) as opposed to being limited to using fixed sky apertures (like 1 arcsecond

apertures). IFS vastly increases the level of analysis that we are capable of performing for both pair and AGN studies.

1.4 Previous Works with IFS

Work has already begun using IFS surveys to study galaxy pairs. Barrera-Ballesteros et al. (2015) studied central and extended star formation and metallicity in galaxy pairs using the CALIFA survey. They utilized the capabilities of the IFS by using variable aperture sizes from which the SFR and metallicity is extracted from. Doing this they found that the SFR is enhanced in the centers of pairs in comparison to controls, but also that the SFR is moderately suppressed in spatially extended regions. The metallicity was found to be consistent with controls in the centers of paired galaxies, but a deficit of metallicity was found in their outskirts.

Thorp et al. (2019) studied a sample of visually identified post-merger galaxies in MaNGA. Post-merger galaxies are the final stage of a galaxy merger when the two galaxies begin to coalesce into a single galaxy while still showing tidal distortions. Thorp et al. (2019) finds that the SFR is centrally enhanced in post-merger galaxies in comparison to control galaxies. They also find a moderate enhancement to the SFR at wider galaxy radii.

Pan et al. (2019) built a sample of galaxy pairs in MaNGA by doing a position search between the MaNGA target galaxies and the galaxies in the parent catalog, the NSA catalog. The NSA catalog tends to have an under-deblending issue such that close pairs are often missed by the catalog. This means that a majority of this sample will consist of pairs with wider separations and that the MaNGA IFUs will only cover one of the two galaxies. Pan et al. (2019) makes up for this by visually identifying pairs which are contained within a

single IFU that display clear tidal features like; tidal tails, bridges, or warped disks. They study the enhancement to the specific star formation rate (sSFR; sSFR = SFR/M, where SFR is the star formation rate and M is the galaxy's stellar mass) in pairs in comparison to control galaxies as a function of galaxy radius. They find that their paired galaxies feature centrally enhanced star formation and that they feature a moderate enhancement of star formation at extended radii.

Jin et al. (2021) used the pair sample from Pan et al. (2019) to study the sSFR in pairs hosting an AGN. They found that the pairs hosting an AGN feature no enhancement to the sSFR in comparison to control galaxies. Jin et al. (2021) also finds that there is no enhancement to the fraction of AGN in pairs in comparison to control galaxies; however, they do not account for the fact that the MaNGA survey is not a volume limited sample.

Our group has also studied galaxy pairs with the MaNGA survey in two previous works. In Fu et al. (2018) (hereafter Paper I) we studied the galaxy pair fraction and merger-induced AGN activity in MaNGA. In Steffen et al. (2021) (hereafter Paper II) we studied the radial profiles of star formation in MaNGA galaxy pairs. I briefly summarize the two papers in the following sections to motivate this thesis.

1.4.1 Fu et al. 2018: AGN in MaNGA Galaxy Pairs

In Paper I, we built a sample of paired galaxies in MaNGA's fourteenth public data release, DR14 (Abolfathi et al., 2018), which included 2618 unique galaxies. From this, we built a sample of 105 spectroscopically confirmed close galaxy pairs (210 total galaxies in pairs), where both pair components are contained within a single MaNGA IFU. This made the study unique as previous pair studies in MaNGA focused on galaxy pairs in which

one component is outside of the MaNGA IFU, which imposes a close separation limit on the sample. We studied the pair fraction in MaNGA and found that it increases linearly with the IFU size and the logarithm of the stellar mass of the MaNGA target galaxy. We found that the cumulative pair fraction in MaNGA is 3.4%, taking into account MaNGA's luminosity dependent volume.

We further studied the rate of AGN in pairs and dAGN in pairs. Out of the 2618 MaNGA target galaxies, we found 391 AGN classified by BPT analysis. We found that 50 out of the 210 paired galaxies contain AGN. Out of the 50 pairs with AGN, we found that there are 14 dAGN. We found that isolated galaxies and paired galaxies have similar AGN duty cycles when matched in stellar mass and redshift, but that dAGN are more common than what may be expected from random pairing. It was found that the observed excess was likely due to correlated AGN activity or synchronous black fueling predicted, as by hydrodynamical simulations.

1.4.2 Steffen et al. 2021: Star Formation in MaNGA Galaxy Pairs

In Paper II, we updated our pair sample for the eighth MaNGA Product Launch (MPL-8), an internal data release to the SDSS collaboration which covered 6142 unique galaxies. The newer data release allowed us to build a larger pair sample to study than what we had in Paper I. With this we were able to expand our pair sample to include 404 close galaxy pairs. We further supplemented this sample of inside-IFU pairs with a set of 492 outside-IFU pairs in which one component of the pair was the MaNGA target galaxy and the other was a galaxy in the NSA catalog.

With the expanded pair sample, we studied star formation in galaxy pairs. We used

MaNGA's spatial resolution to construct radial profiles of the sSFR. We then studied how the radial profiles of the sSFR in pairs compared with those in a set of control galaxies. We found that galaxy pairs generally show a central enhancement to the sSFR of 0.2 dex and a moderate suppression to the sSFR of 0.1 dex beyond 1.0 effective radius ($R_{\rm eff}$; the half-light radius of the galaxy).

We then studied how the radial sSFR profiles are affected by typical merger parameters, including the stellar mass, mass ratio, and projected separation. We found that the enhancement to the radial sSFR profiles in pairs is unaffected by the stellar mass of the MaNGA target but that there is a dependence on the ratio between the stellar masses of the MaNGA target and its companion galaxy. We found that pairs with similar stellar masses showed the greatest sSFR enhancements in comparison to pairs with larger mass ratios. We also found that in pairs with wider mass ratios, the less massive galaxy featured higher levels of sSFR enhancement in their centers in comparison to the more massive galaxy. We also saw that at wider radii, $>$1.5 $R_{\rm eff}$, the more massive component of a pair showed a moderate enhancement to the sSFR while the less massive component of the pair showed a suppression of the sSFR. Finally, we saw that the enhancement to the central sSFR is a strong function of projected separation where close pairs show the strongest enhancements to their star formation.

1.5 Purpose of the Work

As mentioned in Section 1.2.3, there is no consensus on whether or not galaxy interactions are correlated with AGN activity. In our previous work Paper I we saw evidence for correlated AGN in the dAGN sample; however, pairs hosting a single AGN showed no

evidence for merger-induced fueling. This work was done when MaNGA had only finished about a quarter of its observations and MaNGA has now finished its observation goals of observing 10,000 galaxies in its final data release, DR17 (Abdurro'uf et al., 2021). This along with our improved pair selection methodology from Paper II, we will be able to utilize a much larger sample of close galaxy pairs. This larger sample will not only give us better statistics, but also allow us to set stricter limitations on the galaxy pair and AGN selection criteria.

The specific goals of this thesis are the following;

1. We provide a complete catalog of all spectroscopic objects found within the fields-of-view of the MaNGA survey, including galaxies, stars, and quasars.

2. We compile a complete set of spectroscopically confirmed galaxy pairs within the MaNGA survey.

3. We identify a set of optically selected dAGN in the MaNGA survey. These objects are notoriously rare and will be good candidates for future study in other wavelength regimes. Along with this sample, we also present a potential dual broad-line AGN found in the MaNGA survey.

4. We use our galaxy pairs and a set of control galaxies to estimate the relative rates of stochastically-induced, merger-induced, and correlated AGN in the MaNGA sample

5. We test if the AGN found in galaxy pairs show stronger [O III] luminosities in comparison to the AGN in our control galaxies as a proxy of the black hole accretion rate.

This work will not only serve as a useful starting point for future pair studies with IFS but will also help us understand the role of galaxy interactions in galaxy evolution and black hole accretion.

1.6 Organization

This thesis is organized as follows. In Chapter 2, I will describe the MaNGA survey from which we draw our data along with our spectral fitting routine and how we derive galaxy properties from the spectral models. In Chapter 3, I will discuss how we construct our sample of paired galaxies, control galaxies, and AGN. In Chapter 4, I will calculate the volume density of AGN in galaxy pairs and compare them with the expected volume density from stochastically induced AGN. In Chapter 5, I will discuss the relative [O III] luminosities between the AGN in paired galaxies and the AGN in control galaxies. In Chapter 6, I will discuss the results of this work in the context of previous works and in Chapter 7, I will summarize the results of this work. Throughout the thesis, I will assume a ΛCDM cosmology with $\Omega_{\rm m} = 0.3$, $\Omega_\Lambda = 0.7$, and $H_0 = 70$ km s^{-1} Mpc^{-1} such that $h = H_0/100$ km s^{-1} Mpc^{-1} $= 0.7$.

CHAPTER 2

DATA

2.1 SDSS-IV MaNGA

Previous spectroscopic studies have often been spatially limited to either the galaxy's center with an optical fiber or a slice across their disk with a long slit. Acquiring full spectroscopic coverage of a galaxy would take multiple observations such that large surveys of galaxies would not be logistically feasible. SDSS's newest and recently completed IFS survey, MaNGA, solves this problem by employing bundles of compact fiber optic cables which can simultaneously capture spectra across the surfaces of galaxies.

MaNGA uses SDSS's 2.5-meter telescope at Apache Point Observatory (APO) along with two dual-channel BOSS spectrographs (Drory et al., 2015). The spectrographs cover the optical spectrum from 3600−10300Å with a resolution of R∼2000. MaNGA has 17 fiber bundles or integral field units (IFUs) which have variable sizes from 19, 37, 61, 91, and 127 fibers which cover hexagonal areas with diagonal lengths of 12.″5, 17.″5, 22.″5, 27.″5, and 32.″5 on the sky respectively. The survey has a point spread function (PSF) of 2.″5 FWHM from its expected seeing and MaNGA's three-point dithering pattern (Bundy et al., 2015). MaNGA has its own dedicated Data Reduction Pipeline (DRP; Law et al. (2016)) which provides us with fully calibrated and reduced datacubes of spectra for each observation with a pixel size of $0.''5 \times 0.''5 \times 10^{-4}$ dex in α, Δ, and log λ. MaNGA enforces a collision radius of $120''$ between IFUs; however, with the IFU's high spatial resolution and broad spatial coverage closely separated galaxy pairs can be found within the fields-of-view of individual IFUs.

The goal of the MaNGA survey is to observe 10,000 nearby galaxies. This has been accomplished and all data products are published in its seventeenth data release (DR17, Abdurro'uf et al. (2021)). MaNGA's parent catalog is the NASA-Sloan Atlas (NSA) catalog which contains 641,490 galaxies with a redshift, z, below 0.15. The MaNGA survey selects 41,154 of these galaxies within a redshift range of $0.01 < z < 0.15$, a luminosity range of $-17.7 < \mathcal{M} < -24.0$ (where $\mathcal{M}$ is the rest-frame i-band absolute magnitude within a half light elliptical Petrosian aperture), and a tiling area of 7362 deg^2. MaNGA then selects ∼10,000 galaxies out of this targeting catalog such that the sample has a flat stellar mass distribution from $9.5 < \log(M/M_\odot) < 11.5$ and two spatial coverages of 1.5 and 2.5 effective radii ($R_{\rm eff}$; the half-light radius).

The MaNGA sample is split up into a few subsamples. The Primary sample contains the galaxies which are covered out to 1.5 $R_{\rm eff}$ and represents ∼47% of the survey. The Secondary sample contains the galaxies which are covered out to 2.5 $R_{\rm eff}$ and represents ∼37% of the survey. These two samples are made as a compromise between maximal spatial coverage and the number of IFUs which can be made from a limited number of optical fibers. The Color Enhanced sample represents ∼16% of the sample and is designed to select rare galaxy types like massive star forming galaxies or low-mass retired galaxies. The Color Enhanced sample has spatial coverage of 1.5 $R_{\rm eff}$ and can be combined with the Primary sample to create the Primary+ sample. Finally, MaNGA has a few ancillary targets which were not randomly selected like the previous samples but were specifically selected to satisfy other science goals. Some of these ancillary targets include galaxy pairs and AGN; however, if the goal of this work is to study the rates of AGN in galaxy pairs, these ancillary targets

should be avoided. For this work, we will be using both the Primary+ sample and the Secondary sample, which we will refer to as the Main sample.

MaNGA's unique sample design is important to consider when working with it. Since MaNGA wants a flat stellar mass distribution and a semi-uniform spatial coverage, more luminous galaxies will have to be selected over a larger volume so that they will fit within the IFUs. This gives MaNGA a "banana" shaped distribution in redshift and luminosity, which can be seen in Figure 2.1. In the figure, we can also see that there is an offset in redshift between the Primary+ and Secondary subsamples. This exists because the secondary subsample needs to observe higher redshift objects to spatially cover the objects out to 2.5 $R_{\rm eff}$. This distribution of luminosity and redshift means that MaNGA is not a volume limited survey, which makes population statistics more difficult to calculate.

2.2 MaNGA's $1/V_{max}$ Weights

The MaNGA sample has a "banana" shaped distribution in stellar mass and redshift. This means that the comoving volume over which galaxies are selected, which I will refer to as the volume hereafter, is a function of the absolute magnitude. If we want to make comparisons between the prevalence of various populations, we will need to deal with MaNGA's unique distribution. To do this, we use the $1/V_{max}$ weight method (Schmidt, 1968) to recover a volume limited sample. These $1/V_{max}$ weights are defined as,

$$W_j \equiv \frac{N_{\rm tiled}}{N_{\rm obs}} \frac{10^6\,{\rm Mpc}^3}{V_{\rm tiled}\left[z_{\rm min}\left(\mathcal{M}_j\right), z_{\rm max}\left(\mathcal{M}_j\right)\right]}, \tag{2.1}$$

where $N_{\rm tiled}$ is the total number of galaxies from MaNGA's targeting catalog which covers an area of 7362 deg^2 with 1800 plates and $N_{\rm obs}$ is the number of observed galaxies (Wake et al., 2017). As mentioned in Section 2.1, MaNGA's targeting catalog contains 41,154 galaxy but

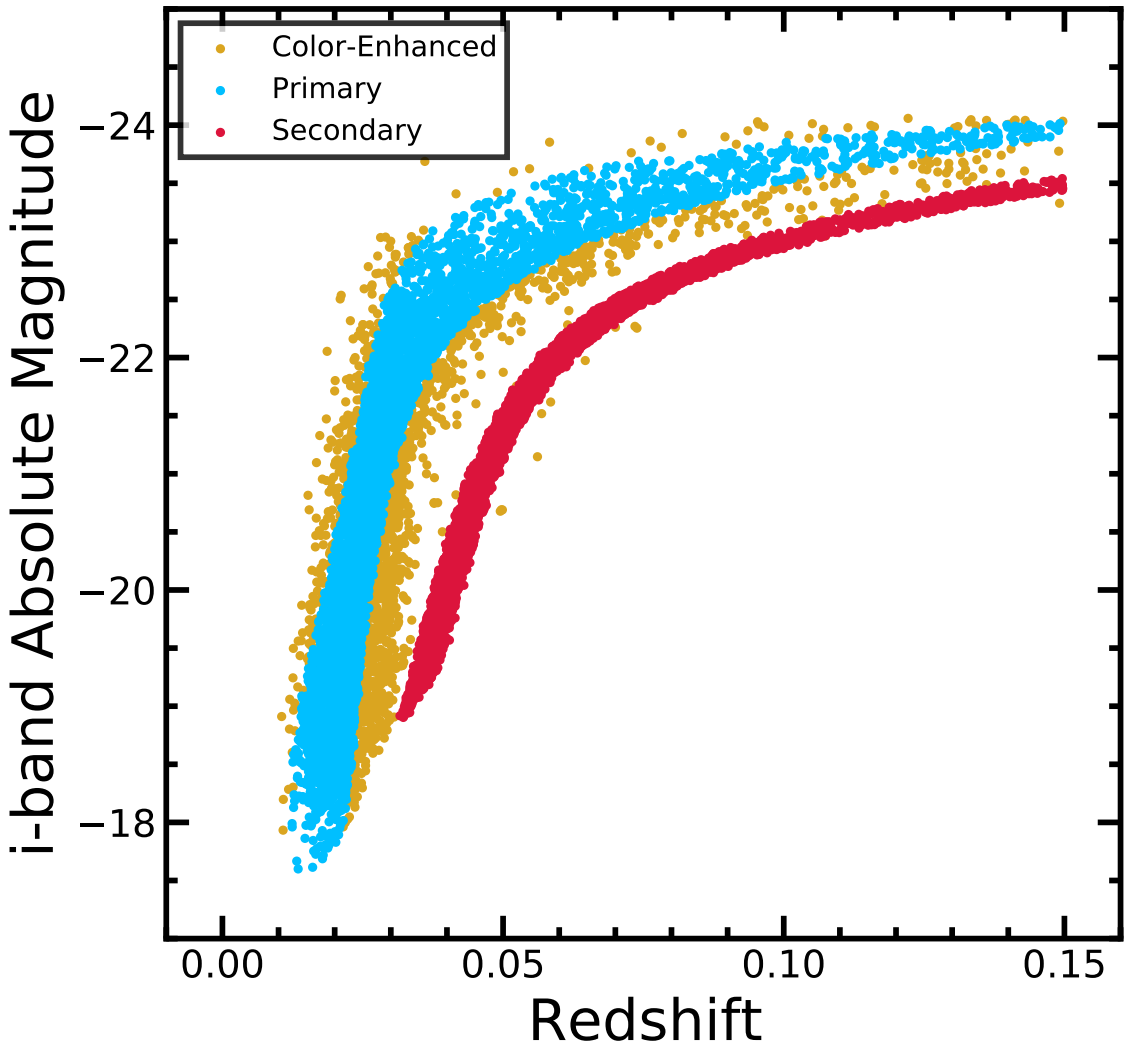

Figure 2.1. The distribution of luminosity and redshift in the MaNGA survey. The Primary sample is shown in blue, the Secondary sample is shown in red, and the Color-Enhanced sample is shown in gold. Here we can see a "banana" shaped distribution which is a consequence of MaNGA targeting strategy.

only ∼10,000 will be actually observed by the survey's completion. The ratio between $N_{\rm tiled}$ and $N_{\rm obs}$ is used to scale the survey's volume by the area actually covered by the survey and $V_{\rm tiled}\left[z_{\rm min}\left(\mathcal{M}_j\right), z_{\rm max}\left(\mathcal{M}_j\right)\right]$ is the volume from the survey's area multiplied by the distance from the galaxy's redshift range determined by its absolute magnitude, $\mathcal{M}$. We use these weights to calculate the volume density, n,

$$n\left(\mathcal{M}_{\rm min}, \mathcal{M}_{\rm max}\right) \simeq \sum_{j=1}^{N_{\rm obs}} W_j / 10^6\,{\rm Mpc}^3. \tag{2.2}$$

The above weights are provided in MaNGA's DRP summary file; however, these values are calculated from the targeting catalog's 1800 tiling plates. In its final data release, MaNGA has only used 609 plates, so we recalculate these weights using our cosmology and using a $N_{\rm obs}$ calculated from the 609 used MaNGA plates. We separately calculate these weights for each of the MaNGA samples; Primary, Secondary, Primary+, etc. Since we will be using the Main sample, we will be using the weights calculated from the footprint of the Primary+ and Secondary samples.

Now that we have recalculated the $1/{\rm V}_{\rm max}$ weights, we want a way to check that they were calculated correctly. We do this by constructing a luminosity function with our weights and then comparing it against a previously calculated luminosity function. We take the volume densities calculated from the $1/{\rm V}_{\rm max}$ weights calculated in Section 2.2 and plot them as a function the r-band absolute magnitude, provided in the MaNGA DRP summary file, in Figure 2.2. We then sum the volume densities in 0.5 magnitude width bins and plot them as a function of the absolute magnitude, forming our luminosity functions.

As a check, we compare our observed luminosity function to the Schechter luminosity function calculated on the SDSS DR6 photometric data from Montero-Dorta and

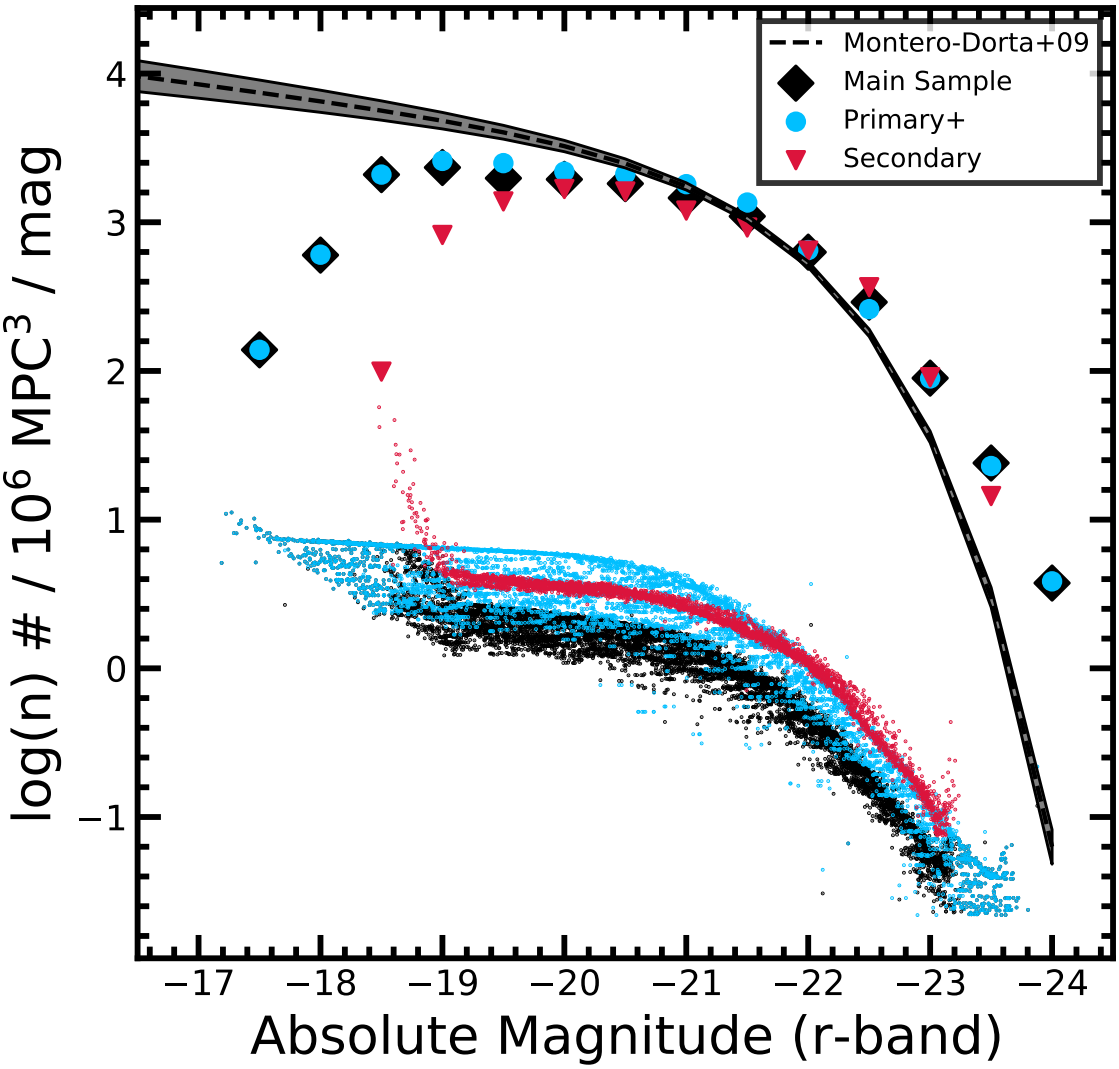

Figure 2.2. The luminosity function of the Main, the Primary+, and Secondary samples. The individual $1/V_{max}$ weights are shown in the small scatter points in black for the Main sample, blue for the Primary+ sample, and red for the Secondary sample. The large black diamonds (Main), blue circles (Primary+), and red triangles (Secondary) show the summed $1/V_{max}$ weights within bins of 0.5 magnitude widths. The black dashed line shows a fit to the Schechter function using SDSS DR6 photometric data from Montero-Dorta and Prada (2009). The grey region around the blacked dashed line represents the upper and lower errors of the fit.

Prada (2009), where the fitted parameters are recalculated for our cosmology. We define the Schechter function, $\Phi(\mathcal{M})$, as,

$$\Phi(\mathcal{M}) = \frac{\mathrm{d}N}{\mathrm{d}V d\mathcal{M}} = 0.4 \log(10)\, \Phi_* \, 10^{-0.4(\mathcal{M}-\mathcal{M}_*)(\alpha+1)} \exp\left[-10^{-0.4(\mathcal{M}-\mathcal{M}_*)}\right], \tag{2.3}$$

where N is the number of galaxies, V is the volume, Φ_* is the normalization factor, $\mathcal{M}_*$ is the characteristic luminosity, and α is the slope for the faint end of the luminosity function. In Figure 2.2, we see that our luminosity function is in rough agreement with Montero-Dorta and Prada (2009). Our faint end slope, α is flatter than what is found in Montero-Dorta and Prada (2009) and our Characteristic Luminosity, $\mathcal{M}_*$, or turn-off point, is somewhat brighter. We also see that our work under-samples faint galaxies below $\mathcal{M}_r$ = -19 in the secondary sample and $\mathcal{M}_r$ = -19.5 in the Primary+ sample. To account for this we will apply a low-end magnitude cutoff at $\mathcal{M}_r$ = -19 for the galaxies that we use in this work.

2.3 Spectral Fitting

The MaNGA team provides fully reduced 3-D datacubes of spectra for each observation. This means that much of the data processing has already been done for us; however, we still need to extract a number of derived quantities from spectral fitting, including; stellar masses, stellar kinematics, emission-line fluxes, emission-line equivalent widths, and gas kinematics. We accomplish this with our own spectral fitting routine, SPFIT, which was introduced in Paper I. SPFIT is designed to simultaneously fit the stellar continuum and emission lines in the spectra based on the Penalized Pixel-Fitting method (pPXF; Cappellari and Emsellem (2004), Cappellari (2017)) and the Gas AND Absorption Line Fitting (GANDALF; Sarzi et al. (2006)) method using MUISCAT's simple stellar populations (SSPs) (Vazdekis et al., 2012).

SPFIT is not the only spectral fitting routine that has been run on the MaNGA datacubes. Other data analysis products include the Data Analysis Pipeline (DAP) (Westfall et al., 2019; Belfiore et al., 2019) and Pipes3d (Sánchez et al., 2017; Sánchez et al., 2017), which are publicly available. We choose to use our own spectral fitting routine, since it allows us to co-added spectra drawn from variable aperture sizes before performing the fitting process. This gives us the freedom to have spectral properties derived from the original $0.''5 \times 0.''5$ spaxel grids, $1''$ radius circular apertures, or apertures fixed to a 1 kpc radius on the galaxy's surface.

We show an example of SPFIT's fitting quality in Figure 2.3. We can also emphasize the utility of separately fitting the stellar continuum and emission lines in Panel (c) of the figure showing the Hα and [N II] doublet. Underneath the emission lines, there is a pair of absorption lines at the same wavelength. If the emission lines were extracted by interpolating the continuum from the red and blue sides of the emission lines, the measured fluxes would be underestimated as the absorption feature underneath would not have been accounted for.

SPFIT is able to extract stellar mass measurements for galaxies. The code does this by fitting the stellar continuum of the galaxy's spectra with a SSP. The stellar mass is then the stellar mass of the SSP that is used to fit the stellar continuum of the galaxy.

We will use the kinematics of the galaxies to check that they are gravitationally bound to each other. SPFIT gives us both stellar and gas kinematics for each fitted spectra, which we may use to make a relative velocity cut between the galaxies. The gas kinematics may offer a better velocity measurement; however, it is dependent on the presence of observable emission lines in the spectra, while the stellar kinematics do not depend on the presence of

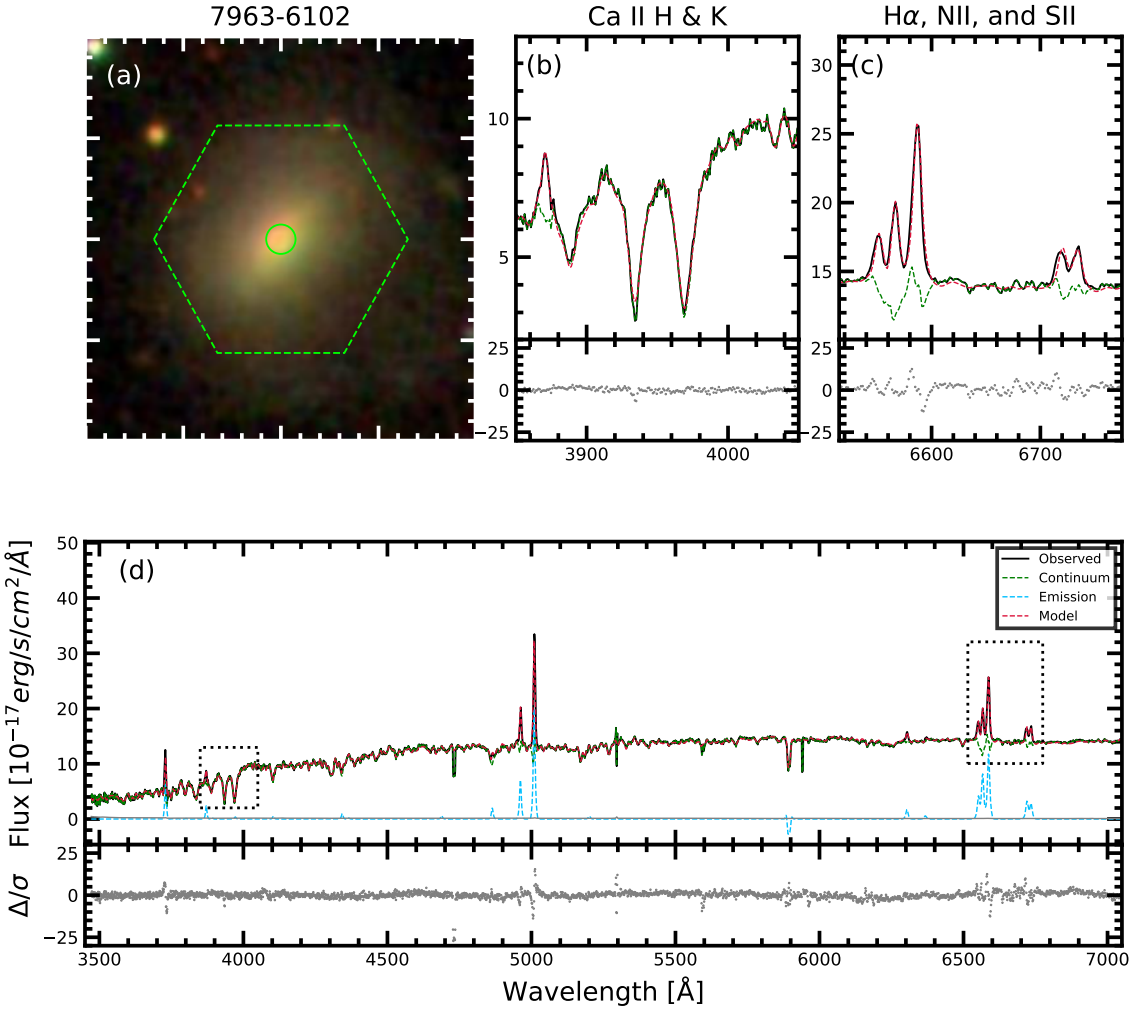

Figure 2.3. An example of SPFIT's spectral fitting capability on a MaNGA target galaxy. Panel (d) shows the observed galaxy spectra extracted from the MaNGA datacubes from a 1″ radius aperture (black) along with the modelled stellar continuum (green) and emission lines (blue). The total model (red) is the sum of the stellar continuum and emission lines. The grey curve shows the error array for the model fit. Underneath the spectra we show the model's residuals which is the observed spectra minus the model spectra and then all divided by the error array. The SDSS pseudocolor image of the MaNGA target is shown in Panel (a) with the MaNGA target highlighted with a green circle and the extent of MaNGA's IFU shown with a green hexagon. Panel (b) shows a zoomed in look at the CaII H and K lines and Panel (c) shows the Hα, [N II], and [S II] emission lines.

emission lines. We decided to come up with a way to use both kinematic measurements. In objects with strong emission lines, we use the gas kinematics and in objects without strong emission lines, we use the stellar kinematics. We use the Hα equivalent width (EW(Hα)) to differentiate between emission-line galaxies and lineless galaxies. Specifically, we use gas kinematics where EW(Hα) $\geq$ 3Å and stellar kinematics where EW(Hα) $<$ 3Å.

The difference can be seen in Figure 2.4, where we plot the stellar kinematics against the gas kinematics for the whole galaxy sample. When the EW(Hα) is greater than 3 Å, the gas and stellar kinematics have a roughly 1:1 relation. When the EW(Hα) falls below 3Å, the measurement of the gas kinematics becomes unbound. In Figure 2.4, we see a large spike in the gas kinematics where the stellar kinematics are near zero in galaxies with EW(Hα) below 3Å. This is because these galaxies have no significant emission lines from which to measure the gas velocity from, which demonstrates the need to use stellar velocities for galaxies with weak emission lines.

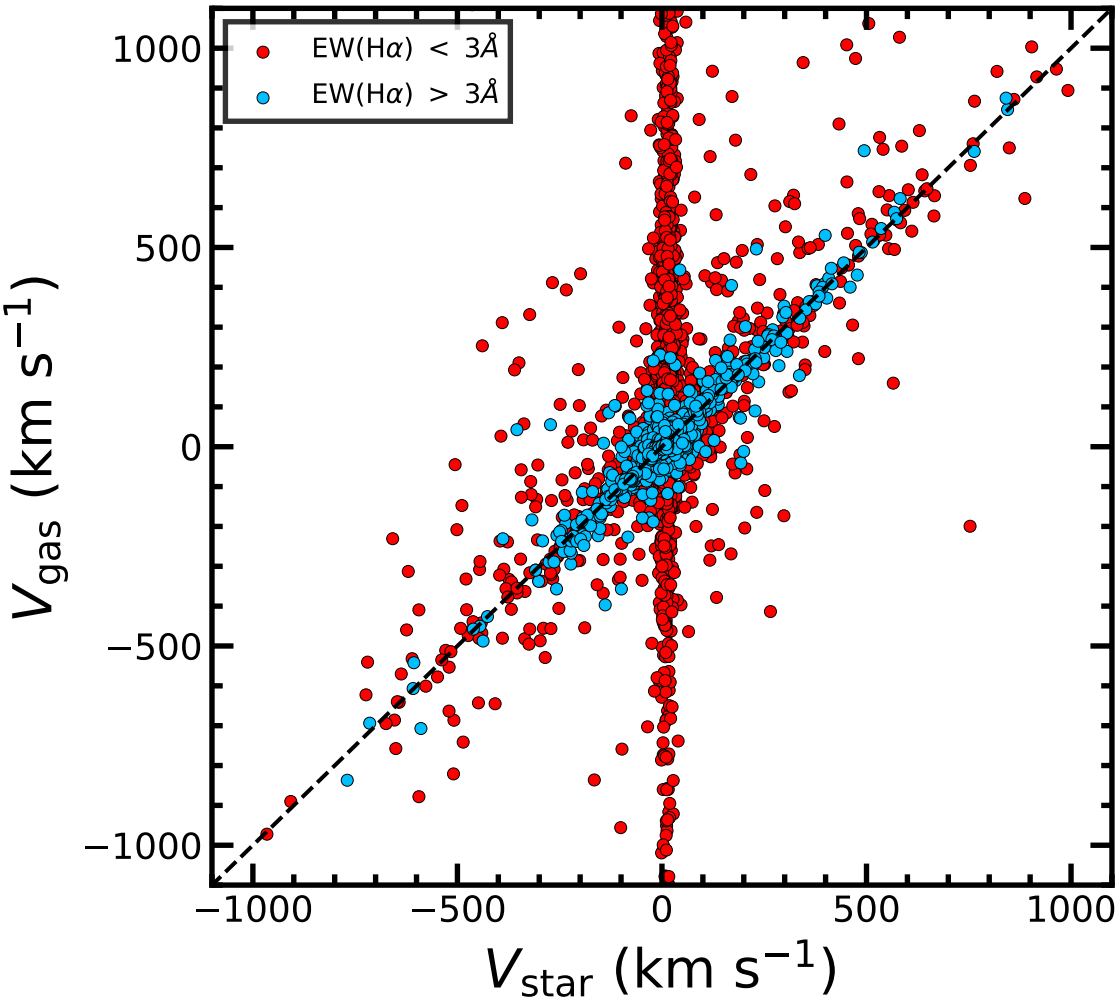

Figure 2.4. The stellar kinematics versus the gas kinematics split into lineless galaxies, EW(Hα) < 3Å (Red), and emission-line galaxies, EW(Hα) > 3Å(Blue). The spectra from which the kinematics are extracted from are a circular aperture with a radius of 1.0 kpc.

CHAPTER 3

PAIR, CONTROL, AND AGN SAMPLES

3.1 Identifying Ancillary Objects in MaNGA

The MaNGA survey is designed to target specific galaxies following the requirements that were outlined in Section 2.1; however, when we look through the MaNGA fields, we find several extra objects in the fields-of-view of the IFUs (see Figure 3.1). While many of these objects are just foreground or background stars or galaxies, a few of these objects are bound to be at the same redshift as the MaNGA target. The MaGNA survey provides a catalog of the observed MaNGA targets, but there is no catalog of all objects which happen to fall within MaNGA's fields-of-view.

While MaNGA doesn't have a full object catalog, there are other more comprehensive catalogs that we can use. The obvious choice is to use one of SDSS's photometric or spectroscopic catalogs as they will share a common footprint with MaNGA. SDSS's spectroscopic catalog suffers from fiber collisions, as mentioned in Section 2.1, which means that the catalog will be incomplete. The photometric catalog is constructed from imaging data and will not be constrained by the fiber placement in a targeting plate. The photometric catalog uses an object deblending algorithm, which identifies objects in the collected images. Unfortunately, this algorithm often "over-deblends" extended objects such that a galaxy may have several photometric objects allocated around its disk.

In Figure 3.1 we overlay the SDSS photometric catalog onto a MaNGA field. We see that the catalog does a good job of identifying all of the major objects in the field, but it does include a few sources that are apparently empty or at least have very dim magnitudes.

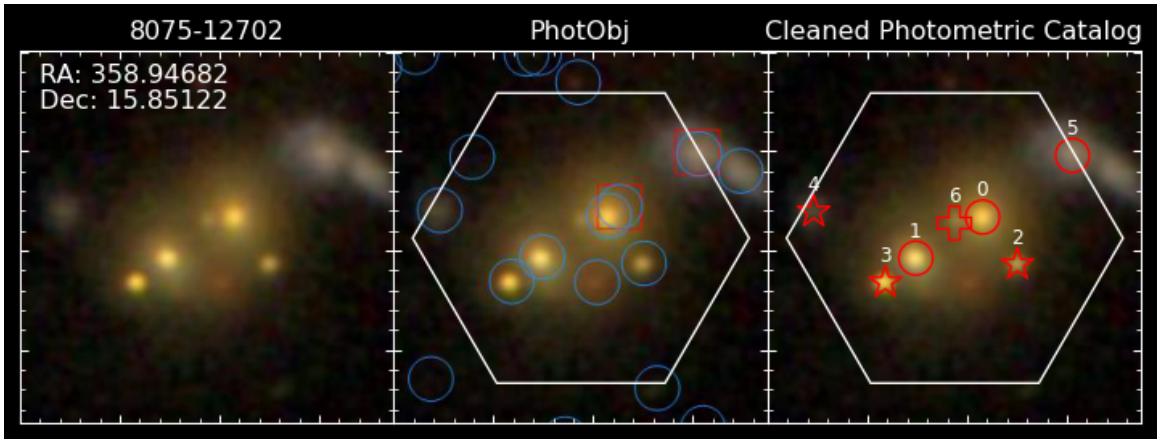

Figure 3.1. MaNGA Plate-IFU: 8075-12702. Each frame shows a pseudocolor image queried from SDSS of the MaNGA field. The left panel is just the empty MaNGA field. The middle panel is the MaNGA field with the coverage of the MaNGA IFU overlaid in the white hexagon and with SDSS photometric objects overlaid in the blue circle and SDSS spectroscopic objects overlaid in red squares. The right panel shows our cleaned set of objects where we removed low S/N objects and over-deblended objects and added missing objects. The red circles represent objects flagged as galaxies by SDSS, the red stars represent objects flagged as stars by SDSS, and the red crosses represent objects manually added to the catalog by us.

We go through and inspect every MaNGA field, with the exception of MaNGA's tiling plates that observe the deep coma cluster, IC342, and M31. We remove over-deblended objects out of our catalog and add in any missing objects into our catalog. This gives us a catalog of the right ascensions and declinations of all objects within the MaNGA IFUs. In total, we find 15,592 objects within the MaNGA fields, including the MaNGA targets.

With a list of objects made, we now want to classify these objects. We extract spectra from the MaNGA datacubes for each object through a $1''$ circular aperture. We then fit the spectra with our spectral fitting routine, SPFIT, mentioned in Section 2.3. We visually inspect and classify each extracted spectrum into the following categories;

- Good - Well modeled galaxy spectra whose redshift is similar to the MaNGA target,

$\Delta v \leq 2000$ km s^{-1}.

- Border - Spectra which almost has a good fit but is somewhat off, typically due to poorer signal-to-noise or that the extracted spectra has contributions from two or more sources.

- $z_{\rm off}$ - Background or foreground galaxies whose redshift is substantially different from the MaNGA target, $\Delta v > 2000$ km s^{-1}.

- QSO - Background high redshift quasars.

- BLAGN - Type I Seyferts, or broad-line AGN (BLAGN), which have substantial emission-line broadening.

- Star - Foreground stars.

- Low S/N - Objects with low signal-to-noise such that they cannot be classified.

- Other - Ambiguous or defective spectra.

An example of our spectral fitting and classification is shown in Figure 3.2. With these categories we find; 10,988 good objects, 189 borderline objects, 451 foreground/background galaxies, 23 QSOs, 84 BLAGN, 1385 stars, 2178 objects with low S/N, and 294 objects with other/ambiguous spectra. This gives us a complete catalog of all objects within the MaNGA fields from which we can now select for paired galaxies.

3.2 Galaxy Pair Sample

With a catalog of all ancillary objects within the MaNGA fields, we can now create a galaxy pair catalog. The first requirement that we set is that the MaNGA plate-IFU is in

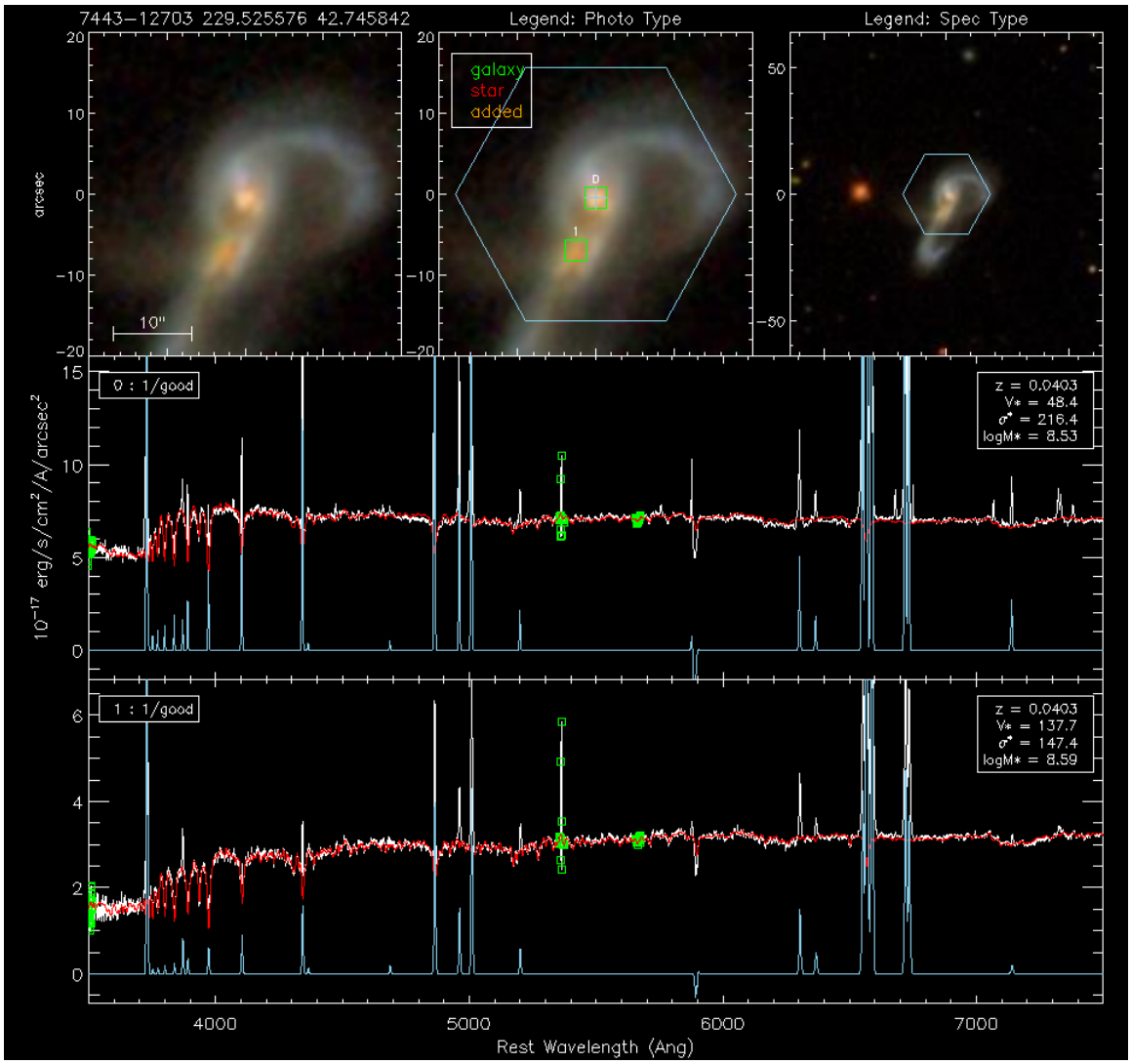

Figure 3.2. MaNGA Plate-IFU: 7443-12703. In the top row we show SDSS pseudocolor images. On the Left we show a 40″ field of the MaNGA target and in the middle we show the same field but with the hexagonal IFU highlighted in blue and with the identified objects highlighted in green squares. The green cross highlights the MaNGA target. The numbers above the objects refers to the object's position in the Plate-IFUs catalog and corresponds to the numbers shown in the text box at the top left of the spectra below. On the right is the field seen in a wider 120″ field-of-view. Below the initial row are the spectra of the identified objects. The white spectra is the observed spectra extracted from the MaNGA datacube and the red spectra is the SPFIT model spectra. The extracted emission-line spectra is shown in blue.

the Main sample as defined in Section 2.1. We also impose a r-band absolute magnitude cut on the MaNGA target galaxies of $\mathcal{M}_r \leq$ -19 based on Figure 2.2. Next, we require that the object's spectra is classified as either "good" or as a BLAGN, as described in Section 3.1. This gives us 11,072 galaxies whose redshift is similar ($\Delta v \leq 2000$ km s^{-1}) to their MaNGA target or who are the MaNGA targets themselves.

3.2.1 Relative Velocity Cuts

Next, we want to set a relative line-of-sight velocity cut to ensure that the two objects are near each other along the observer's line of sight. We describe each pair candidate with a line-of-sight velocity based on stellar or gas kinematics following the procedure in Section 2.3. We define the relative velocity between them as $\Delta v = |v_{\rm t} - v_{\rm c}|$, where $v_{\rm t}$ is the velocity of the MaNGA target galaxy and $v_{\rm c}$ is the velocity of the companion galaxy. We set a relative velocity cut of $\Delta v \leq 500$ km s^{-1} between the MaNGA target and its companion. In the literature, relative velocity cuts tend to be between 300 km s^{-1} and 1000 km s^{-1}, though we find that a more or less strict relative velocity cut does not have a substantial impact on the resulting pair selection.

3.2.2 Mass Ratio Cuts

The MaNGA survey provides stellar masses derived through r-band elliptical Petrosian apertures from the NSA catalog. Unfortunately, these are only provided for the MaNGA targets and most of the identified companion galaxies will not have measurements in the NSA catalog because of the catalog's incompleteness. The NSA catalog's algorithm often under-deblends sources, such that the Petrosian aperture will attempt to cover multiple nearby galaxies in crowded fields. For our paired galaxies, the NSA catalog's Petrosian

apertures often cover both pair components so the given stellar mass measurement is really the stellar mass of the pair. If we want to find the stellar masses of the individual galaxies, we need a way to partition the given stellar masses from the NSA catalog between the two paired galaxies.

SPFIT provides us an estimate of the stellar mass by matching a SSP to the observed stellar continuum. As a first order approximation of the stellar mass, we extract the spectra of each object through a 1.0 kpc radius circular aperture, using the MaNGA target's redshift to scale the aperture size. The spectra within the circle is then co-added and a stellar mass is estimated from the SPFIT model. With the size of the aperture, we are only estimating the mass of the galaxy's nucleus; however, these masses may be useful as a mass ratio between the paired galaxies. We define the mass ratio between the masses in the nucleus of the galaxies as;

$$\mu = M'_{\rm t}/M'_{\rm c} \tag{3.1}$$

where $M'_{\rm t}$ is the nuclear stellar mass of MaNGA target galaxy and $M'_{\rm c}$ is the nuclear stellar mass of the companion galaxy.

Ideally, we want to measure stellar masses from apertures that sit the sizes of both of the paired galaxies in the IFU. The photometry for both the MaNGA target galaxies and their companions are not readily available. We use the source extraction code, SExtractor[1], to calculate r-band magnitudes from isophote apertures for the galaxies in our MaNGA fields using the r-band field images from SDSS. A useful feature of the SExtractor algorithm is that it can deal with foreground objects in front of the target by mirroring the flux from the

[1]SEXTRACTOR; https://sextractor.readthedocs.io/en/latest/Introduction.html

other side of the target. This is useful as many of our objects will be within crowded fields. We can now use these magnitudes to calculate a magnitude ratio, $\Delta\mathcal{M}$, defined as;

$$\Delta\mathcal{M} = -0.4\,(\mathcal{M}_{\rm t} - \mathcal{M}_{\rm c})\,, \tag{3.2}$$

where $\mathcal{M}_{\rm t}$ and $\mathcal{M}_{\rm c}$ are the r-band magnitudes of the MaNGA target and identified companion galaxy respectively.

We now compare the two measurements in Figure 3.3. We see that the mass ratios extracted from circular apertures with SPFIT and the magnitude ratios extracted from elliptical Petrosian apertures in SExtractor are in good agreement. While we are temped to use the magnitude ratios, our magnitude ratio measurements are not complete over our galaxy catalog as the SExtractor algorithm misses some objects with lower signal-to-noise. We therefore decide to use our mass ratios calculated from SPFIT with 1.0 kpc radius circular apertures for our pair sample construction.

With the mass ratios between the paired galaxies defined, we can now partition the stellar masses from the NSA catalog between the two paired galaxies. The mass of the MaNGA target, $M_{\rm t}$, is;

$$M_{\rm t} = \frac{M_{\rm NSA}}{1 + 1/\mu}, \tag{3.3}$$

where $M_{\rm NSA}$ is the stellar mass from the NSA catalog. The stellar mass of the companion galaxy, $M_{\rm c}$, is then calculated as,

$$M_{\rm c} = \frac{M_{\rm NSA}}{1 + \mu} \tag{3.4}$$

We now define the logarithmic mass ratios which we will be using throughout this

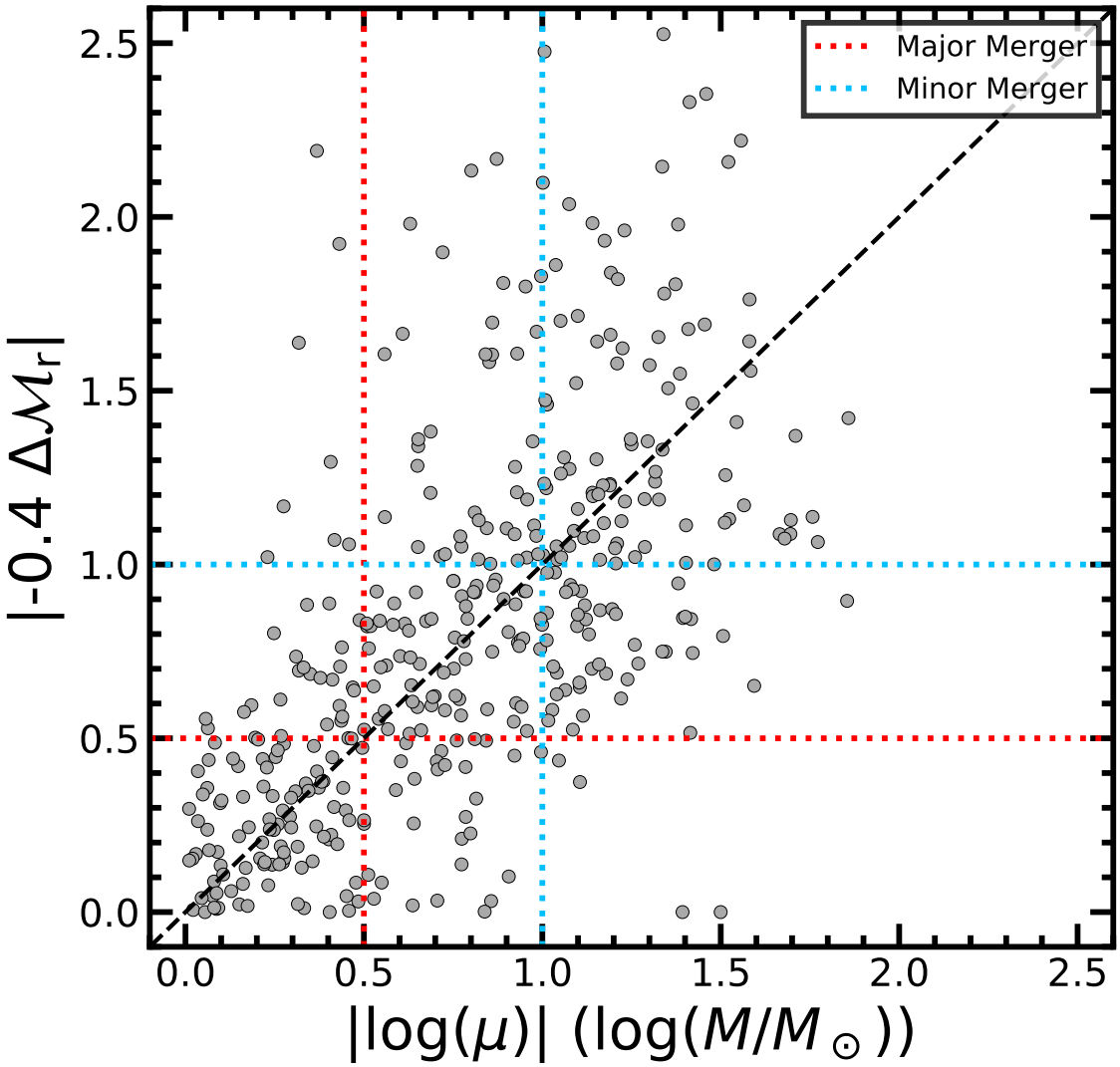

Figure 3.3. The nuclear mass ratio, $\log(\mu)$, versus the r-band Elliptical Petrosian magnitude ratio, -0.4 $\Delta\mathcal{M}$. The ratios for individual galaxy pairs are shown in the grey circles. The dashed black line shows the 1:1 ratio between the measurements, the dotted red line shows the definition of a major merger, 3:1, and the dotted blue line shows the definition of a minor merger, 10:1.

work as;

$$\Delta \log(M) = \log(M_{\rm t}) - \log(M_{\rm c}) = \log(\mu) \tag{3.5}$$

Traditionally, major mergers are defined as pairs under a 3:1 mass ratio and minor mergers are defined as pairs under a 10:1 mass ratio, so we set our logarithmic mass ratio cut at $|\log(M/M_{\odot})| \leq 1.0$. We define major and minor mergers in log space such that $|\log(M/M_{\odot})| \leq 0.5$ is the definition of a major merger and $0.5 < |\log(M/M_{\odot})| \leq 1.0$ is the definition of a minor merger.

3.2.3 Separation Cuts

Galaxy pair surveys often set an upper limit on the allowed projected separation between the galaxies. The MaNGA sample imposes a natural projected separation limit from its redshift bounds and IFU size. If we take $\rm H_0$ = 70 km $\rm s^{-1}$ $\rm Mpc^{-1}$, MaNGA's upper redshift limit, $z = 0.15$, and MaNGA's largest IFU size, $32.5''$, the maximum possible projected separation is $\sim$50 kpc. The typical projected separation limits used in previous galaxy pair studies are about 50 kpc $\rm h^{-1}$ (about 70 kpc using h = 0.7), so we see that the MaNGA survey conveniently imposes a projected separation limit that is roughly consistent with previous galaxy pair studies.

While we don't need to impose any physical separation limits, we will set a couple of angular separation requirements. We impose a requirement that a paired galaxy must be within the inscribed circle that is $1''$ from the hexagonal IFU boundary, thus excluding objects that fall in the corner of an IFU. We do this to eliminate a position angle selection bias. Continuing with this position angle issue, we also only want MaNGA targets that are in the center of the IFU by requiring that the MaNGA target is within 10% of the radius of the

MaNGA IFU. In the case of an off-center MaNGA target, the position angle for a companion is limited to a small range of angles and the allowed separation between the pairs can also be higher, since the two pairs can be located at either ends of the IFU. Requiring that the MaNGA target is in the center of the IFU effectively cuts the 50 kpc maximum separation limit down to 25 kpc. A results of this is that our pair sample's projected separation range will be much shorter than many other galaxy pair samples.

3.2.4 Pair Sample Selection Summary

For convenience, I will summarize all of our pair selection requirements here;

1. We require that the MaNGA field be in the Main galaxy sample.
2. We require that the MaNGA target galaxy has a r-band absolute magnitude less than $\mathcal{M}_r \leq$ -19.
3. We require that the spectra of the galaxies have either been visually classified as "good" or as a BLAGN as described in Section 3.1.
4. We require that the relative velocity between the galaxies be within $\Delta v \leq 500$ km s^{-1}.
5. We require that the mass ratio between the galaxies be within $\Delta \log(M) \leq 1.0$.
6. We require that the galaxy be within a $1''$ inscribed circle within the hexagonal IFU.
7. We require that the MaNGA target be within 10% of the radius of the MaNGA IFU.

Doing this, we find 426 galaxy pair systems containing 894 objects, such that we have 387 pairs, 37 triplets, 1 quadruplet, and 1 quintuplet. To keep our analysis simple later on, we only make use of the pair systems and remove the multipole systems from the sample.

3.2.5 MaNGA Pair Fraction

In Figure 3.4 we show the distribution of paired galaxies in the MaNGA sample as a function of the MaNGA target's stellar mass and the redshift-dependent, physical IFU size. The figure shows that the paired galaxies in MaNGA are biased to high stellar masses and large IFU sizes. The bias towards large IFU sizes is obvious as there is a larger field in which to capture a paired galaxy. The bias towards high mass galaxies is also to be expected as massive galaxies tend to be more tightly grouped in galaxy clusters. This is due to the dynamical friction between a galaxies' dark matter halo and the dark matter in the cluster. The strength of the dynamical friction is mass dependent such that more massive galaxies experience larger amounts of friction (Chandrasekhar, 1943). The friction removes momentum from the galaxy and it moves towards the gravitational center of the halo, resulting in the most massive galaxies residing in the halo's center, where they have a higher chance of interacting with each other.

Since MaNGA is not a simple volume limited survey, we cannot describe the rate of pairs as a simple fraction of pairs to non-pairs. Instead, we model the two dimensional pair fraction, $f_{\rm pair}^{\rm mod}$, with a linear function in both IFU radius, $R_{\rm IFU}$, and stellar mass, M,

$$f_{\rm pair}^{\rm mod}(R_{\rm IFU}, M) = 10.0\% \left(\frac{R_{\rm IFU}}{30\ {\rm kpc}}\right)\left(\frac{M}{10^{11}\ M_{\odot}}\right). \tag{3.6}$$

This best-fit model is useful as it can be compared with the results from cosmological simulations like Illustris (Nelson et al., 2015) and can be used to constrain these simulations. Using the best fit model, the cumulative pair fraction, $F_{\rm pair}$, can then be given as,

$$F_{\rm pair} = \frac{\sum_{j=1}^{N_{\rm gal}} W_j f_{\rm pair}^{\rm mod}(r_{\rm max}, M_j)}{\sum_{j=1}^{N^{\rm gal}} W_j}, \tag{3.7}$$

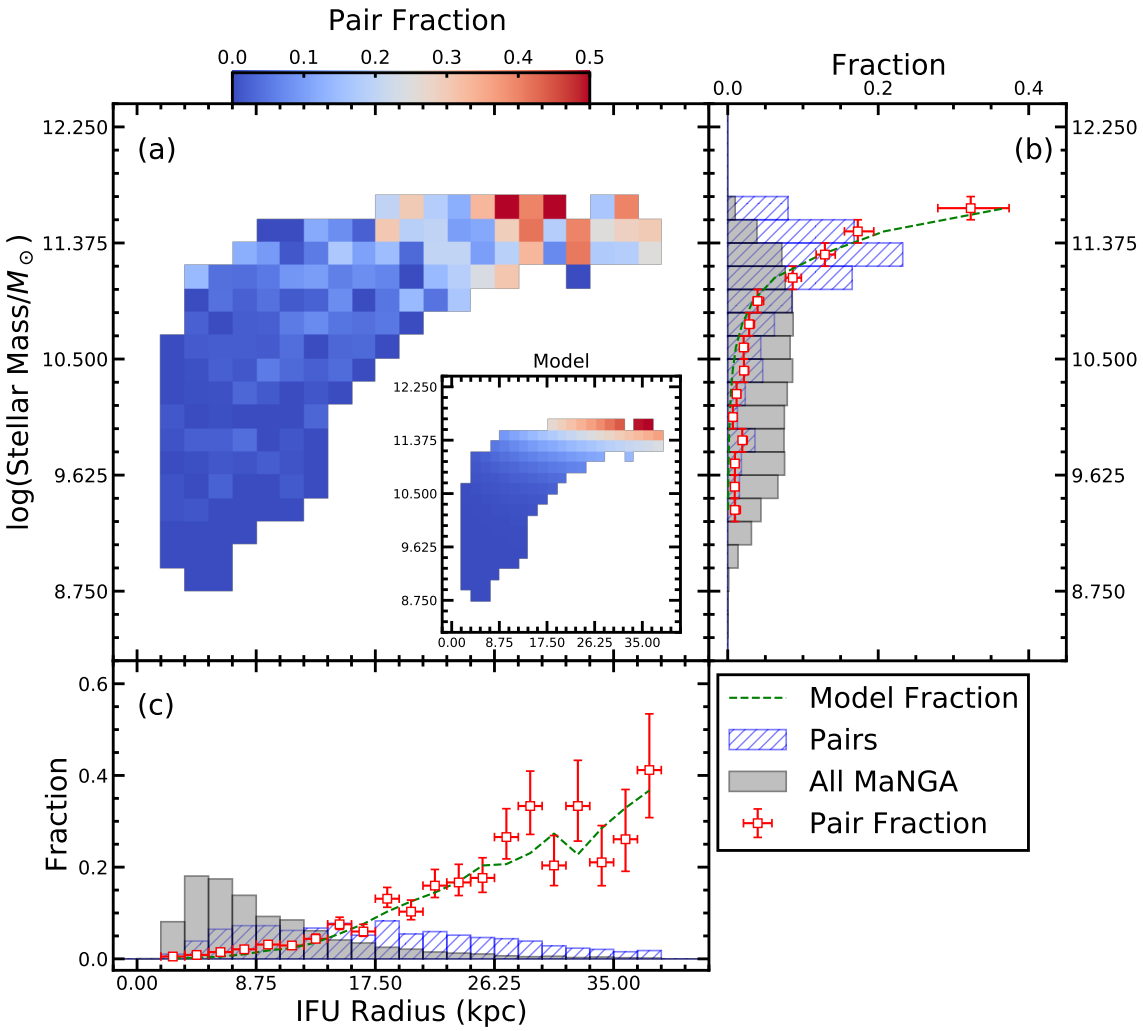

Figure 3.4. An updated pair fraction based on Figure 1 from Paper I. Panel (a) shows the observed pair fraction as a function of IFU radius in kpc (based on the target galaxies redshift) and stellar mass. The inset shows the best-fit model pair fraction from Equation 3.6. Panel (b) shows the the normalized histogram of stellar mass for the MaNGA sample (grey) and paired galaxies (blue) along with the observed pair fraction as a function of stellar mass (red squares) and the modeled pair fraction (green dashed line). Panel (c) is the same as Panel (b) but for the pair fraction as a function of IFU radius in kpc.

where W_j is the $1/V_{max}$ weights from Equation 2.1 and r_{max} is the maximum projected separation in the pair selection. The maximum projected separation for a pair in our sample is $r_{max} = 20$ kpc $h^{-1} = 28.6$ kpc. If we use $r_{max} = 28.6$ kpc, we find a cumulative pair fraction of $F_{pair} = 4.33\% \pm 0.29\%$. This result is in agreement with our results from Paper I and those found in Robotham et al. (2014).

3.3 Selecting Active Galactic Nuclei

An AGN can be identified through its strong optical emission lines; however, there is another possible source of photoionization in galaxies: OB stars. The ionizing spectra from OB stars contains few photons with energies above 13.6 eV, which results in a thin partially ionized zone. This means that the low-ionization forbidden lines like [N II] will be weak relative to Hα. AGN produce a strong power-law spectra, which extends into the far-UV and X-ray. These high energy photons are capable of penetrating through the Strömgren sphere and create a larger partially ionized zone. This results in strong low-ionization forbidden lines relative to Hα. AGN also produce high thermal energies which increases the gas temperature which enhances the production of collisionally excited forbidden lines.

The ionization level of a region can be determined by the relative strength of ionized oxygen lines, though [O III]/Hα is typically used instead as Hα and [O I] have similar ionization energies and [O III] and Hα have similar wavelengths which minimizes the effects of reddening. We plot the line ratios [N II]/Hα and [O III]/Hβ in the left panel of Figure 3.5 in what is called a BPT diagram (Baldwin, Phillips, and Terlevich, 1981). In the plot we see a "v" shaped distribution where the left branch are the regions ionized by OB stars, or star formation, and the right branch are the regions ionized by AGN.

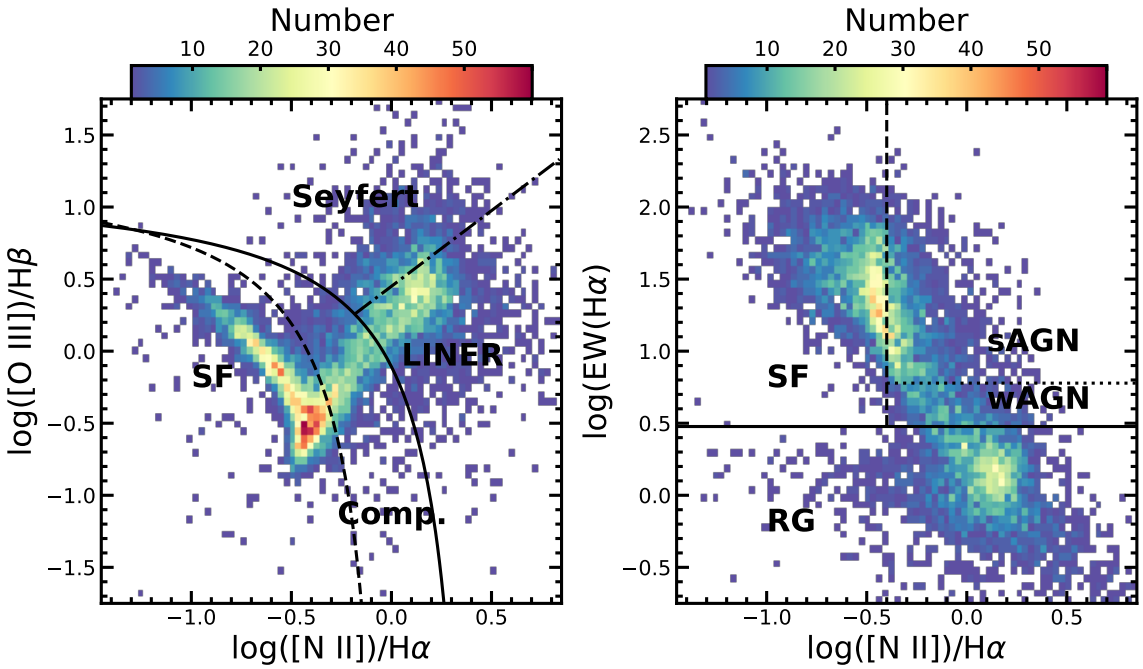

Figure 3.5. Left: The BPT diagram for MaNGA galaxies where the emission line measurements are extracted from a 1 kpc radius circular aperture. The data is binned in a 2-D histogram where the color corresponds to the number of galaxies in that bin. The dashed line is the K03 line (Equation 3.9), the solid line is the K01 line (Equation 3.8), and the dot-dashed line is the S07 line (Equation 3.10). Right: The WHAN diagram for the same sample. Retired galaxies (RG) are shown under EW(Hα) = 3Å, weak AGN (wAGN) are shown under EW(Hα) = 6Å, strong AGN (sAGN) are above EW(Hα) = 6Å, and star forming galaxies (SF) are shown to the left of log([N II]/Hα) = -0.4.

While we can tell that both branches on the BPT diagram represent different ionization sources, we need a way to objectively separate the two branches. There are two commonly used methods for splitting the two branches. The first is the theoretical maximum starburst line from Kewley et al. (2001) (K01),

$$\log([\mathrm{O\,III}]/\mathrm{H}\beta) = \frac{0.61}{\log([\mathrm{N\,II}]/\mathrm{H}\alpha) - 0.47} + 1.19, \tag{3.8}$$

which is shown as the solid line in the left hand panel of Figure 3.5. The second is the empirical separation between AGN and star forming galaxies from Kauffmann et al. (2003) (K03),

$$\log([\mathrm{O\,III}]/\mathrm{H}\beta) = \frac{0.61}{\log([\mathrm{N\,II}]/\mathrm{H}\alpha) - 0.05} + 1.30, \tag{3.9}$$

which is shown as the dashed line in left hand panel of Figure 3.5. We define the region beneath Equation K03 as star forming galaxies, the region between Equations K03 and K01 as composite starbust/AGN, and the region above Equation K01 as AGN.

The AGN region can now be subdivided between LINERs (Low Ionization Nuclear Emission-line Region) and Seyferts with the empirical separation from Schawinski et al. (2007) (S07),

$$\log([\mathrm{O\,III}]/\mathrm{H}\beta) = 1.05\log([\mathrm{N\,II}]/\mathrm{H}\alpha) + 0.45 \tag{3.10}$$

which is shown as the dot-dashed line in the left panel of Figure 3.5.

This would almost give us a complete classification method; however, it has been shown by Stasińska et al. (2008) that the ionization spectra from hot low-mass evolved stars (HOLMES) in retired galaxies can produce emission-line ratios that mimic other classifications, especially LINERS, on the BPT diagram. The emission lines that these HOLMES

produce are weak in comparison to those produced by OB stars and AGN. Cid Fernandes et al. (2011) showed that the EW(Hα) is a good tracer of HOLMES such that these retired galaxies can be selected out using an EW(Hα) cut, which can be seen in the WHAN diagram in the right panel of Figure 3.5. We reclassify any galaxy with an EW(Hα) < 6Å as a retired galaxy regardless of its previous BPT classification. Previous studies have often used EW(Hα) < 3Å as the cut for retired galaxies; however, we find that a stricter 6Å cut eliminates much of the noise in the subsequent results sections in Chapters 4 and 5.

3.3.1 AGN in Galaxy Pairs

With our pair sample defined, we want to identify AGN within these pairs. We apply our AGN classification scheme from Section 3.3 to the pair sample. Within the 387 galaxy pairs, we have: 525 retired galaxies, 141 star forming galaxies, 59 composite starburst/AGN galaxies, 18 LINERs, 17 Type II Seyferts, 8 Type I Seyferts, and 6 galaxies with an ambiguous BPT classification.

With our set of AGN in pairs identified, we will now create three subsamples. The first is the dAGN sample containing pairs in which both galaxies host an AGN. The second is the single AGN sample containing pairs in which only a single galaxy hosts an AGN. The third is the single+dual AGN sample, which is the combination of the previous two samples, i.e. one or both galaxies may host an AGN. The dAGN sample contains 24 pairs, the single AGN sample contains 54 pairs, and the combined single+dual AGN sample contains 78 pairs.

We depict the AGN selection in pairs and dAGN on the BPT and WHAN diagrams in Figure 3.6. The full dAGN sample is shown in Table 3.1 and in Figure 3.7 with their SDSS pseudocolor images, BPT maps, and BPT diagrams. Our dAGN sample is only twice

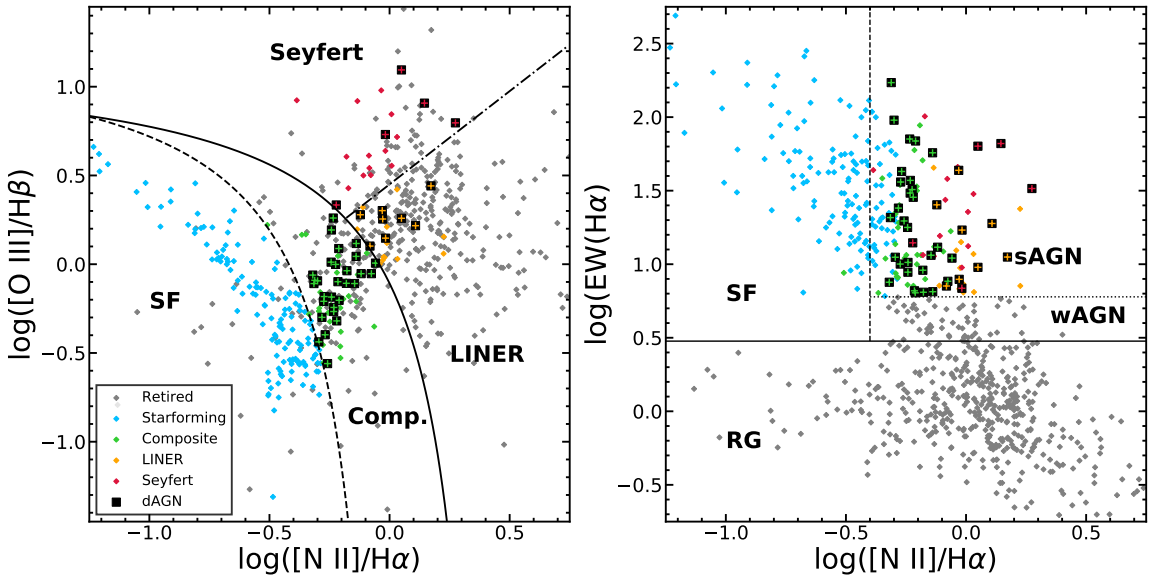

Figure 3.6. Left: The BPT diagram for the galaxies in our pair sample where the emission line measurements are extracted from a 1 kpc radius circular aperture. The dashed line is the K03 line (Equation 3.9), the solid line is the K01 line (Equation 3.8), and the dot-dashed line is the S07 line (Equation 3.10). The emission line classifications are color coded diamonds such that retired galaxies are grey, star forming galaxies are blue, composite galaxies are green, LINERs are orange, and Seyferts are red. The black squares represent the galaxies in our dAGN sample and the color of the embedded cross represents its emission line classification. Right: The WHAN diagram for the same sample. The color coding here is identical to what is shown in the Left panel.

as large as the one defined in our previous work, Paper I, where MaNGA had only finished about a quarter of its observations; however, we use more restrictive requirements for our AGN selection. In Paper I we imposed an EW(Hα) $\geq$ 3Å requirement for AGN, while in this work we raise the requirement to 6 Å.

3.3.2 Dual Broad-Line AGN

In MaNGA plate-IFU 9892-6102 (also known as Mrk 883), we find what may be a dAGN in which both components feature broadened emission lines. We show the spectra for both components in Figure 3.8 where we can also see that the pair shows significant tidal

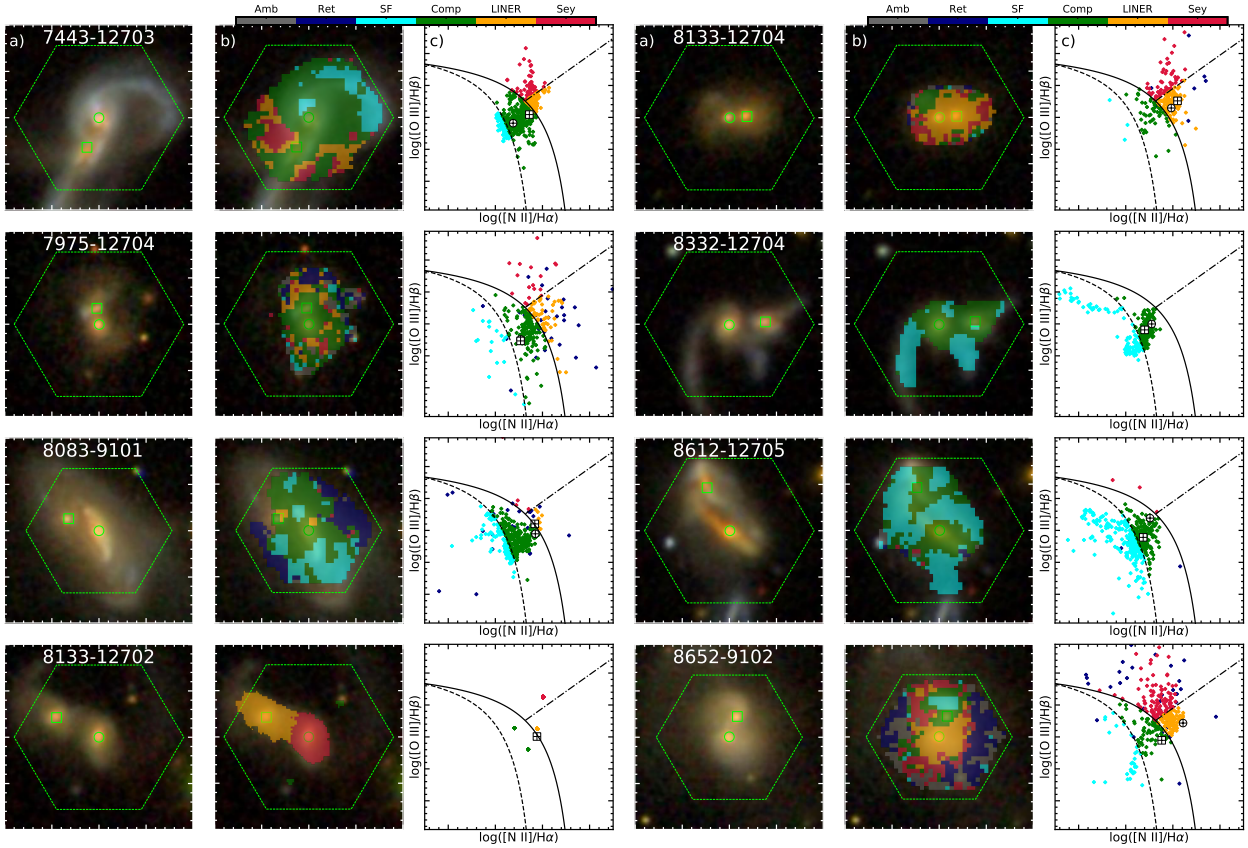

Figure 3.7. **Column A:** SDSS pseudocolor images of the dAGN sample with the components highlighted with green circles and squares (The circle is the MaNGA target and the square is the companion galaxy). **Column B:** BPT classification map for each MaNGA spaxel rebinned to a 1″× 1″ grid. (Each tick in the columns A and B represents 2 arcseconds). **Column C:** BPT diagram for the MaNGA plate-IFU. The white circles and squares represents the emission-line ratios extracted from a 1″ aperture over the centers of each dAGN component. The shapes correspond to the green shapes which highlight the objects in the left column. The solid line represents the maximum starburst line from K01, the dashed line represents the empirical star-forming demarcation from K03, and the dashed-dotted line represents the empirical separation between LINERs and Seyferts from S07. In plate-IFUs - 8133-12702, 9039-9101, 9892-6102, 10218-12703, and 10518-12704, one or both of the galaxies host an AGN with a broad-line component. We did not fit for broad-line components in our run with SPFIT so the emission line ratios for individual spaxels are likely underestimated and the line ratios for these cores were not calculated for the 1 kpc radius circular extraction.

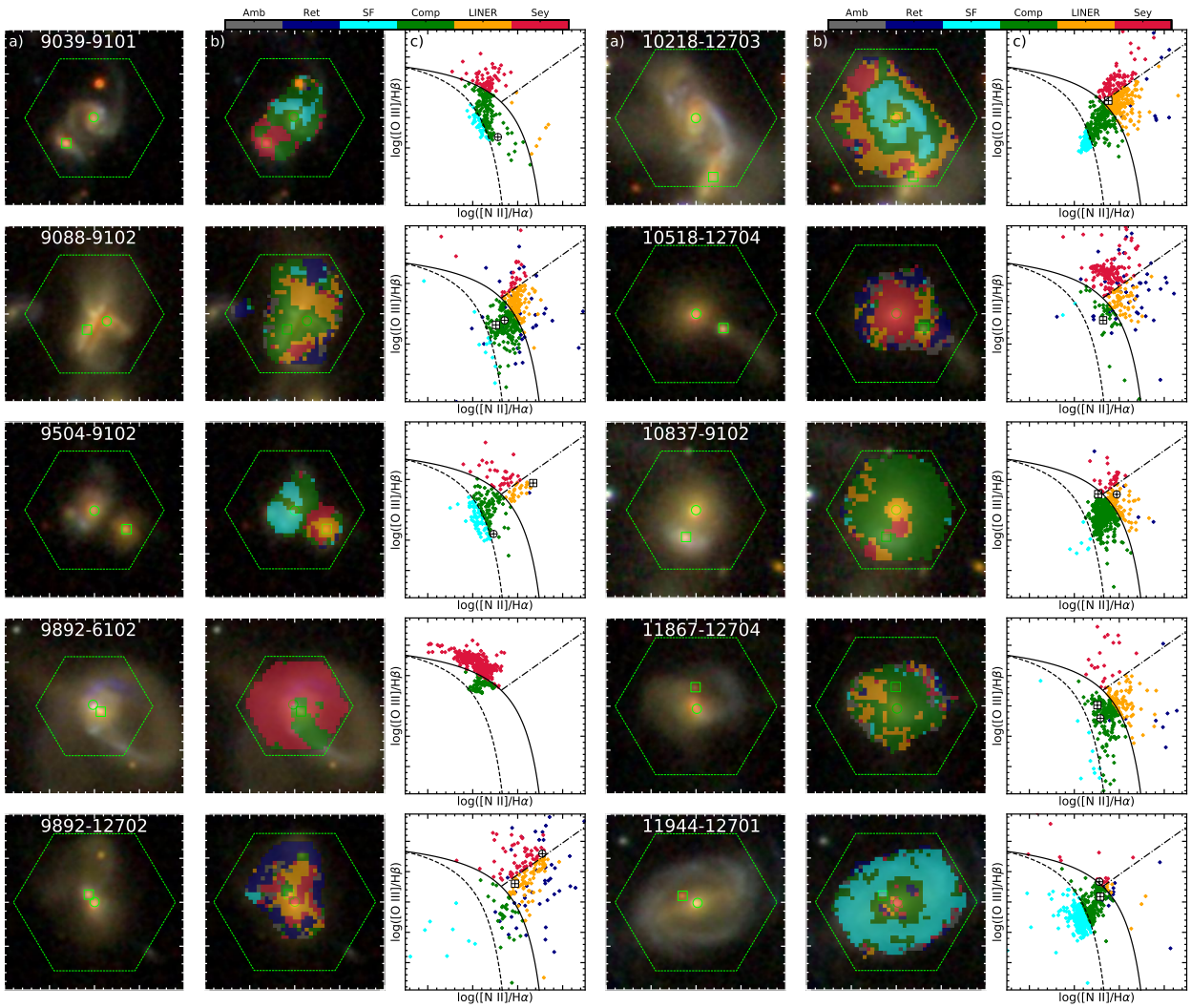
Amb
Ret
SF
Comp
LINER
Sey
a) 9039-9101
b)
c)
a) 10218-12703
b)
c)
9088-9102
10518-12704
9504-9102
10837-9102
9892-6102
11867-12704
9892-12702
11944-12701
log([O III]/Hβ)
log([N II]/Hα)

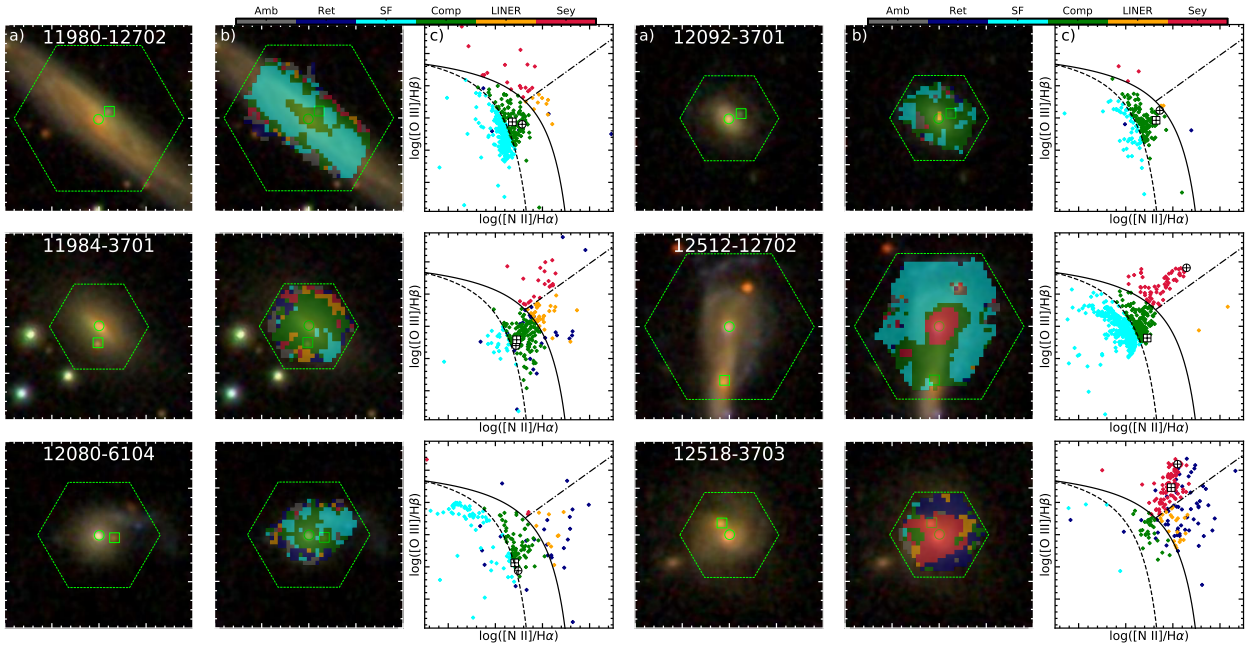

features. This object is significant as the broadened emission lines are a strong indicator that both sources are an AGN as stellar sources are not capable of creating the observed velocity dispersions. Unfortunately, the two sources are very close together, 1.″8, which is below MaNGA's 2.″5 PSF. Higher resolution data will be required to verify that this source is in fact a dual broad-line AGN. We performed a cursory search for this object is other surveys and papers but found no high resolution data for this object.

3.4 Control Galaxy Sample

If we want to see if there is an enhancement to the rate of AGN in pairs, we need know the rate of AGN in a set of isolated control galaxies. We define these controls as MaNGA target galaxies without any other galaxies in their IFU's field-of-view that have a line-of-sight velocity below $\Delta v \leq 2000$ km s^{-1}. Also, like the paired sample, we require that the control galaxies be in Main sample and to have an r-band absolute magnitude that is

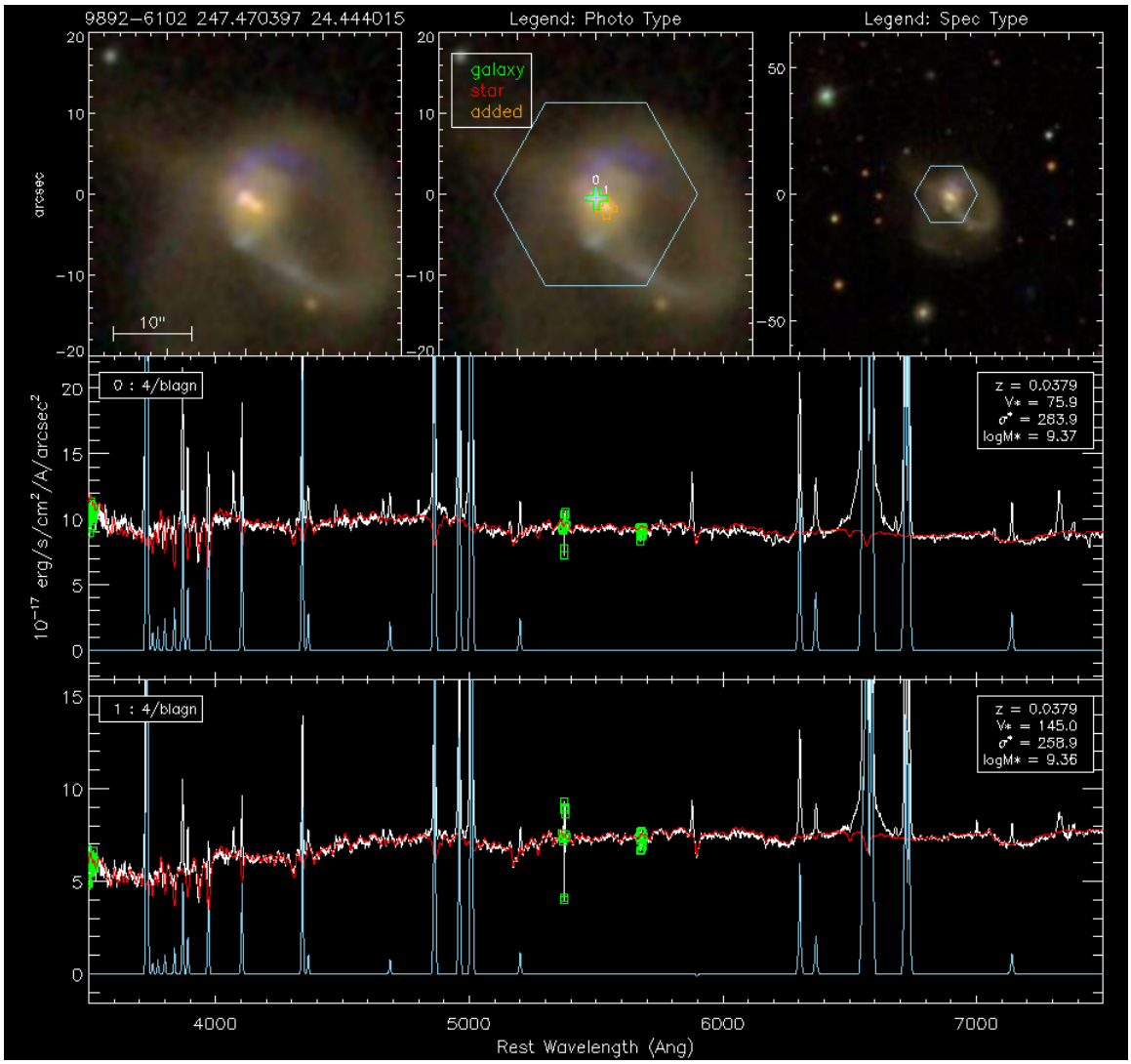

Figure 3.8. Same as Figure 3.2 but for MaNGA plate-IFU 9892-6102. Broadened emission-lines can be seen in both components of the two pairs.

less than $\mathcal{M}_r \leq$ -19. Applying these requirements, we find 7811 control galaxies. Among these we have 872 AGN of which there are 613 composite starburst/AGN, 70 LINERs, 126 type II Seyferts, and 63 type I Seyferts.

There is a known redshift and stellar mass dependence on the rate of AGN in galaxies. Therefore, we need to quantify the rate of AGN in our sample as a function of the stellar mass and redshift. In Figure 3.9, we show the 2-D AGN fraction as a function of the stellar mass and redshift. We see that the AGN fraction has a Gaussian distribution in stellar mass centered around $\log(M/M_\odot) = 10.5$, while the AGN fraction apparently has no evolution with the redshift. This is not to say that there is no redshift evolution with AGN, but that our redshift range in MaNGA is not wide enough to see a correlation.

We model AGN fraction, $f_{\rm AGN}^{\rm mod}$, with a stellar mass dependent Gaussian distribution and a redshift dependent power-law function,

$$f_{\rm AGN}^{\rm mod}(M,z) = f_0 \exp\left[-\frac{1}{2}\left(\frac{\log M/M_\odot - b}{\sigma}\right)^2\right](1+z)^4 . \tag{3.11}$$

Since we found no apparent redshift dependence in our limited redshift space, we have assumed a power-law index of 4 rather than fit this as a free parameter to be consistent with the AGN luminosity function of galaxies with $z \leq 1$ (Ueda et al., 2003). We fitted the stellar mass dependent Gaussian distribution to our sample with $f_0 = 0.12 \pm 0.0042$, $b = 10.54 \pm 0.011$, and $\sigma = 0.43 \pm 0.011$. We show this model in the inset in Panel (a) of Figure 3.9. We can now use this model to estimate the baseline stochastic fueled AGN rate in our paired AGN sample.

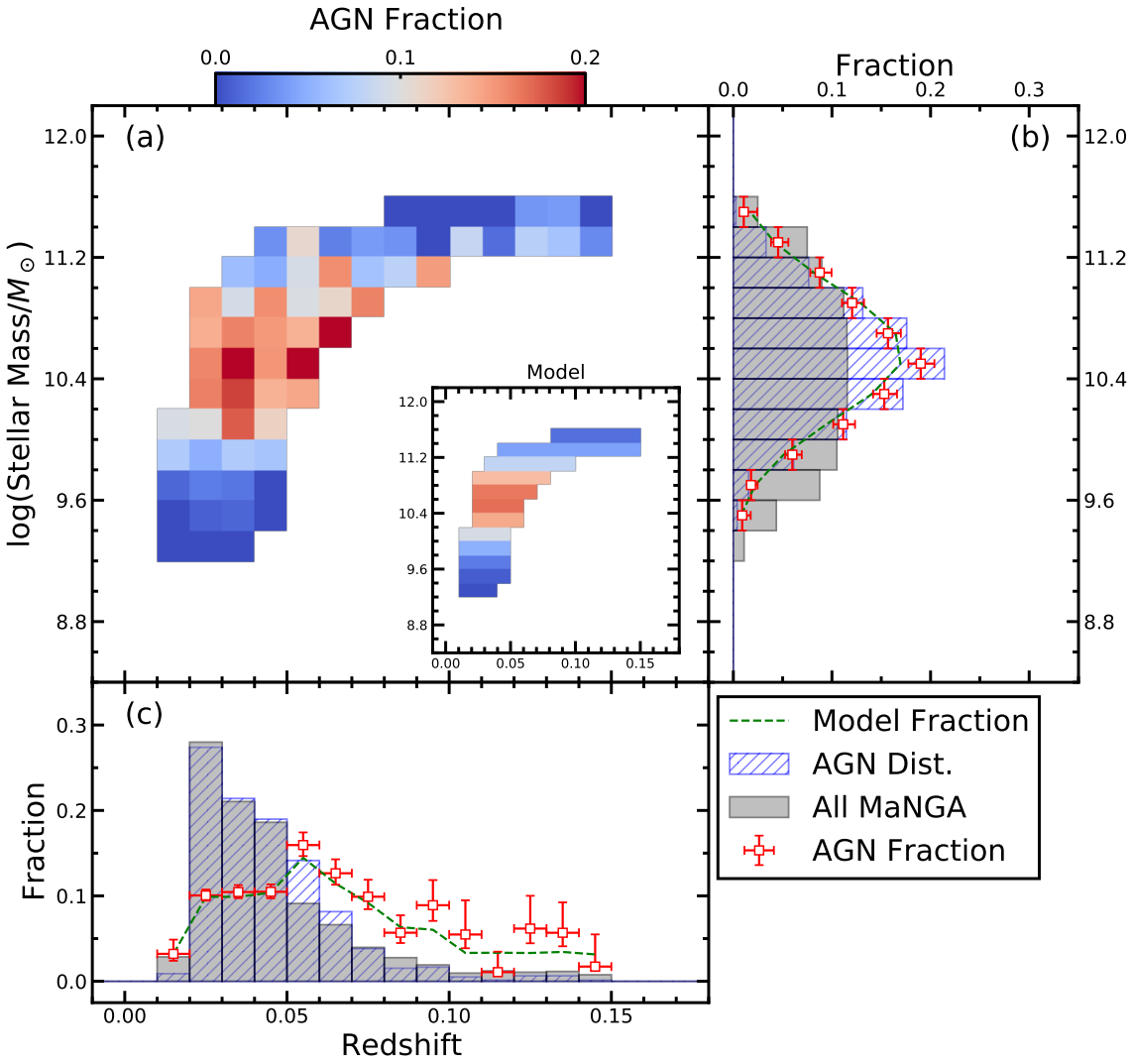

Figure 3.9. The 2D AGN fraction in our isolated control galaxies. Panel (a) shows the observed AGN fraction as a function of redshift and stellar mass. The insets shows the best-fit model from Equation 3.11. Panel (b) shows the normalized histogram of the stellar mass for the MaNGA sample (grey) and the AGN control sample (blue) along with the observed AGN fraction as a function of the stellar mass (red squares) and the modeled AGN fraction (green dashed line). Panel (c) is the same as Panel (b) but for the AGN fraction as a function of the redshift.

Table 3.1. Dual AGN in MaNGA

Plateifu	RA (deg)	DEC (deg)	Redshift	$\Delta\theta$ (arcseconds)	r_p (kpc)	Δv (km s^{-1})	Δlog(M) log($M_\odot$)	log(M) log($M_\odot$)	BPT
(1)	(2)	(3)	(4)	(5)	(6)	(7)	(8)	(9)	(10)
				Dual AGN					
7443-12703	229.52558	42.74585	0.04027	···	···	···	···	10.4	2
7443-12703	229.52653	42.74407	0.04027	6.9	5.5	90.9	-0.1	10.5	2
7975-12704	324.58641	11.34867	0.08886	···	···	···	···	11.0	2
7975-12704	324.58655	11.34961	0.08886	3.5	5.7	213.9	0.6	10.3	2
8083-9101	50.13841	-0.33996	0.03828	···	···	···	···	10.9	2
8083-9101	50.14021	-0.33923	0.03828	7.0	5.3	96.9	1.0	9.9	3
8133-12702	113.51094	43.54360	0.08310	···	···	···	···	11.2	5
8133-12702	113.51438	43.54479	0.08310	10.0	15.6	230.3	0.7	10.5	2
8133-12704	114.77573	44.40277	0.13447	···	···	···	···	10.9	3
8133-12704	114.77430	44.40287	0.13447	3.7	8.8	104.6	-0.2	11.1	3
8332-12704	209.16355	43.58561	0.10309	···	···	···	···	11.0	2
8332-12704	209.16066	43.58578	0.10309	7.6	14.4	112.0	0.8	10.2	2
8612-12705	255.10152	38.35170	0.03579	···	···	···	···	10.5	2
8612-12705	255.10322	38.35430	0.03579	10.5	7.5	239.6	0.5	10.0	2
8652-9102	331.64618	0.05643	0.04614	···	···	···	···	10.8	3
8652-9102	331.64572	0.05766	0.04614	4.7	4.3	108.3	0.3	10.6	2
9039-9101	229.00036	34.35688	0.12530	···	···	···	···	10.8	2
9039-9101	229.00243	34.35531	0.12530	8.4	18.8	248.4	-0.2	11.0	5
9088-9102	242.47148	26.62545	0.07786	···	···	···	···	11.0	2
9088-9102	242.47287	26.62491	0.07786	4.9	7.2	58.1	-0.1	11.0	2
9504-9102	121.70124	28.42148	0.14231	···	···	···	···	10.7	2
9504-9102	121.69901	28.42025	0.14231	8.3	20.8	103.4	-0.3	11.0	3
9892-6102	247.47037	24.44400	0.03787	···	···	···	···	10.4	5
9892-6102	247.46998	24.44366	0.03787	1.8	1.3	29.9	0.0	10.4	5
9892-12702	247.81469	23.88264	0.05918	···	···	···	···	10.6	4
9892-12702	247.81508	23.88313	0.05918	2.2	2.5	64.4	0.5	10.1	3
10218-12703	118.63425	16.80972	0.04609	···	···	···	···	10.8	5
10218-12703	118.63312	16.80600	0.04609	13.9	12.6	285.1	0.3	10.5	3
10518-12704	152.68067	6.20040	0.09775	···	···	···	···	11.0	5
10518-12704	152.67895	6.19949	0.09775	7.0	12.6	115.4	0.8	10.3	2
10837-9102	159.34846	2.31265	0.04021	···	···	···	···	10.8	3
10837-9102	159.34907	2.31096	0.04021	6.5	5.2	107.6	0.9	9.9	2
11867-12704	136.00426	1.45809	0.05338	···	···	···	···	10.5	2
11867-12704	136.00436	1.45942	0.05338	4.8	5.0	78.4	0.9	9.7	2
11944-12701	241.89255	36.48404	0.02983	···	···	···	···	10.3	4
11944-12701	241.89361	36.48445	0.02983	3.4	2.0	16.6	0.5	9.8	2
11980-12702	253.74259	22.14845	0.03544	···	···	···	···	10.5	2
11980-12702	253.74197	22.14883	0.03544	2.5	1.7	24.6	0.5	10.1	2
11984-3701	256.59261	21.40617	0.03096	···	···	···	···	10.1	2
11984-3701	256.59269	21.40522	0.03096	3.4	2.1	49.1	0.6	9.6	2
12080-6104	31.27009	-0.71173	0.04319	···	···	···	···	10.1	2
12080-6104	31.26918	-0.71187	0.04319	3.3	2.8	1.5	0.7	9.4	2
12092-3701	13.91369	14.77361	0.04038	···	···	···	···	9.9	2
12092-3701	13.91298	14.77390	0.04038	2.7	2.1	19.5	0.4	9.5	2
12512-12702	146.37349	-0.36520	0.05150	···	···	···	···	10.4	4
12512-12702	146.37380	-0.36844	0.05150	11.7	11.8	267.5	-0.1	10.5	2
12518-3703	159.60443	-0.39268	0.09630	···	···	···	···	11.1	4
12518-3703	159.60487	-0.39198	0.09630	3.0	5.3	96.8	0.4	10.7	4

Note. (1) MaNGA plate-IFU number. (2)-(3) Right ascension and declination in degrees. (4) Redshift from spectra extracted through a 1 kpc radius aperture. (5)-(6) Projected separation in arcseconds and kiloparsecs. (7) line-of-sight velocity offset. (8) Logarithmic stellar mass ratio. (9) Stellar mass of the galaxy calculated by splitting the stellar masses from the NSA catalog between the two components with the mass ratio. (10) BPT classification code: 0-retired, 1-star forming, 2-composite starburst/AGN, 3-LINER, 4-type I Seyfert, 5-type II Seyfert.

CHAPTER 4

SEPARATION DEPENDENT DUTY CYCLE OF AGN IN PAIRS

4.1 Uncorrelated Stochastic AGN Model in Pairs

Since the MaNGA survey is not volume limited, we cannot simply describe the duty cycle of AGN in the pairs by taking the ratio between the number of AGN in pairs to the total number of pairs. Instead, we will need to use the $1/V_{max}$ weights from Section 2.2 to recover a volume limited sample. We can use the $1/V_{max}$ weights to represent our AGN sample as a volume density instead of a number ratio. The observed volume density of AGN in the pairs sample, n_{obs}, will be calculated as sum of the volume weights of the pairs in the dAGN, single AGN, and single+dual AGN samples,

$$n_{obs} = \sum_{j=1}^{N_{AGN}} W_j. \tag{4.1}$$

The AGN in our pair sample are not necessarily induced by merger-driven processes. It is possible for the paired galaxies to possess an AGN induced by internal processes that are unrelated to galaxy interactions. We can estimate the expected volume density of AGN in our pairs that are stochastically induced using the modeled AGN fraction in our control galaxies from Equation 3.11 in Section 3.4. If we find more AGN in our pairs than what is expected by random pairing then we can assume that the excess may be due to either merger-induced AGN feeding or correlated AGN activity.

We estimate the rate of stochastic fueling in our pairs using the $1/V_{max}$ volume weights and the modeled AGN fraction in our control sample, $f_{agn}(M, z)$ from Section 3.4. We can do this by employing basic probability equations. For the dAGN sample, we need

the probability that both nuclei are active at the same time. This probability is similar to the probability of achieving two heads-up when flipping two quarters, so the probability of seeing a dAGN is the probability of both galaxies hosting an AGN multiplied together. This means that our expected volume density of dAGN, $n_{\rm st}^{\rm dagn}$, is,

$$n_{\rm st}^{\rm dagn} = \sum_{j=1}^{N_{\rm pair}} W_j \, f_{\rm agn}(M_j^t, z_j) \, f_{\rm agn}(M_j^c, z_j). \tag{4.2}$$

In the coin-toss example, each coin has a 50% chance of getting a heads-up. In our case, each paired galaxy will have its own probability of hosting an AGN, $f_{\rm AGN}$, that we calculate from our AGN fraction model in Section 3.4. M^t and M^c are the stellar masses of the MaNGA target and its companion respectively and z is the redshift of the pair. This probability is then transformed into an expected volume density by multiplying it by their $1/\mathrm{V}_{\rm max}$ weight, W_j. In the single AGN case, we need the probability that one nuclei is active while the other is not. For one galaxy, this is the probability of the one nuclei multiplied by one minus the probability of the other nuclei. This is then repeated for the other galaxy such that,

$$\begin{aligned} n_{\rm st}^{\rm sagn} = &\sum_{j=1}^{N_{\rm pair}} W_j \, f_{\rm agn}(M_j^t, z_j) \, [1 - f_{\rm agn}(M_j^c, z_j)] \\ &+ \sum_{j=1}^{N_{\rm pair}} W_j \, f_{\rm agn}(M_j^c, z_j) \, [1 - f_{\rm agn}(M_j^t, z_j)]. \end{aligned} \tag{4.3}$$

The probability that either of the nuclei are active is the probability of one plus the probability of the other minus the probability of both multiplied together such that,

$$\begin{aligned} n_{\rm st}^{\rm s+dagn} = &\sum_{j=1}^{N_{\rm pair}} W_j \, f_{\rm agn}(M_j^t, z_j) + \sum_{j=1}^{N_{\rm pair}} W_j \, f_{\rm agn}(M_j^c, z_j) \\ &- \sum_{j=1}^{N_{\rm pair}} W_j \, f_{\rm agn}(M_j^t, z_j) \, f_{\rm agn}(M_j^c, z_j). \end{aligned} \tag{4.4}$$

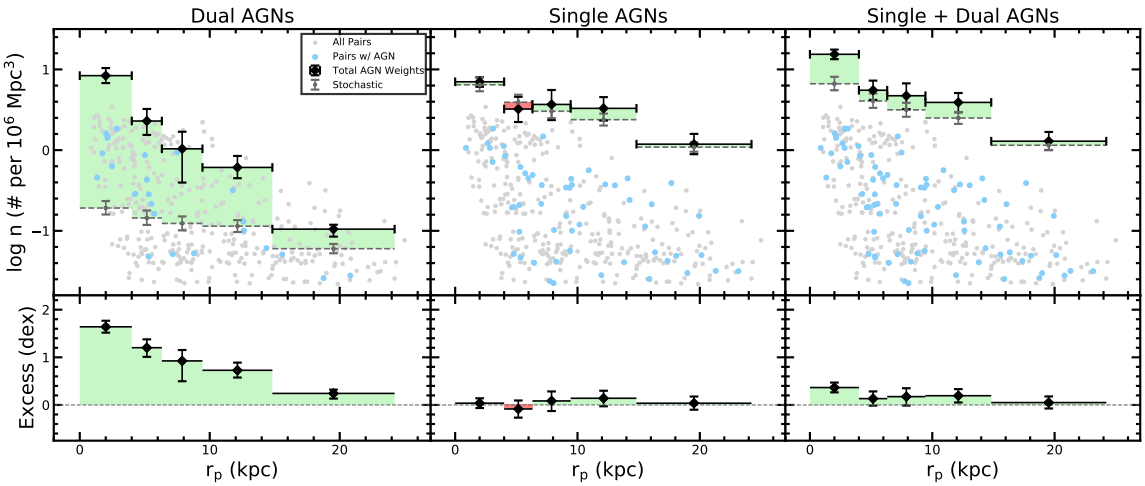

Figure 4.1. Observed versus expected AGN volumes densities as a function of projected separation in our MaNGA pair sample. In the top panels, the grey circles represent the individual $1/V_{max}$ weights for the whole pair sample and the blue circles represent the $1/V_{max}$ weights for the pairs hosting AGN. The black diamonds represent the observed volume densities, from Equation 4.1 and the dark grey diamonds represent the expected volume densities (from Equations 4.2, 4.3, and 4.4 for the dual, single, and single+dual subsamples respectively). The horizontal error bars represent the bin size and the vertical error bars represent the 1σ confidence interval. The filled color between the observed and expected volume densities represent where the observed volume density is greater than (green) or less than (red) the expected volume density. The bottom panels show the excess of observed AGN by taking the logarithmic difference between the observed and expected volume densities.

The expected volume densities of AGN from random pairing are then calculated using these equations and the weights, stellar masses, and redshifts of the whole pair sample.

We show the observed and the expected stochastic volume densities as a function of the projected separation, r_p and split by dAGN, single AGN and single+dual AGN in Figure 4.1. The grey points show the $1/V_{max}$ weights for all of the pairs in our sample while the blue points show the weights for the pairs with AGN. The observed volume density is calculated by summing the weights in discrete projected separation bins shown in the black diamonds. The expected volume densities are shown with the grey diamonds.

The pairs are not evenly distributed across the separation space. We find a high density of pairs between 5-10 kpc and a low density of pairs beyond 15 kpc. To account for this, we use an adaptive binning method that divides the sample into five evenly populated separation bins based on the distribution of the whole pair sample.

The error bars on the observed and expected volume densities represent the 1σ confidence intervals found using the bootstrap resampling method. In this method, a robust estimate of the properties of a distribution can be determined by iteratively resampling the data through replacement. In our case, we randomly select 68% of the dataset and calculate the data's mean. This process is repeated over 1000 iterations. The sample of 1000 means are then taken and the 1σ confidence interval is calculated above and below the distribution's mean. The errors of the expected volume density also receives an additional 0.01 dex error from the best-fit AGN fraction model in Equation 3.11.

In Figure 4.1, we see that the dAGN show a large excess of AGN of 0.2 dex ($\sim$1.6$\times$) at wide separations (20 kpc) and an excess of 1.6 dex ($\sim$40$\times$) at close separations (2 kpc). The distribution appears to be an inverse power-law distribution, in log space, where the volume density of AGN rapidly falls with increasing projected separation. In the single AGN, we do not see a surplus or deficit of AGN in any projected separation bin. In the single+dual AGN sample, we also see an inverse power-law distribution that is weaker than the dAGN sample. At 2 kpc there is a 0.4 dex ($\sim$2.5$\times$) surplus of AGN and by 20 kpc there is no surplus of AGN.

From this, we see that there is a separation dependent excess of AGN in the dAGN and single+dual AGN samples over what would be anticipated from stochastic processes.

This indicates to us that there must be a contribution from either or both merger-induced AGN fueling and correlated AGN activity.

4.2 Model of Merger-Induced and Correlated AGN in Pairs

In the previous section we found evidence for merger-driven AGN fueling. We now want to explain the excess AGN we see in the context of galaxies mergers. We believe that there are two different phenomena from the merger event that may be enhancing the volume density of AGN that we see. The first phenomenon is that the merger-induced gas-inflows are enhancing the baseline probability for an AGN to occur. This would boost the excess AGN we see in all three AGN subsamples and this effect is likely separation dependent, such that there will be a higher probability for AGN at close separations.

Hydrodynamical simulations have shown that much of the AGN activity in mergers in not synchronous; however, there is often a period of time in the merger event where both black holes are accreting material simultaneously (Van Wassenhove et al., 2012; Capelo et al., 2017). The second phenomenon may be from this synchronous black hole accretion period. Van Wassenhove et al. (2012) and Capelo et al. (2017) find that synchronous AGN tend to occur in the later stages of the merger, which means that this effect will biased to close separations. This effect will also remove pairs from our single AGN sample and add them to the dAGN sample so that a deficit of single AGN is created along with a surplus of dAGN.

Another possible source for correlated AGN activity is from AGN cross-ionization. It is possible for the AGN in one galaxy to ionize the gases in its neighbor, tricking the observer into thinking that the neighbor is also an AGN. An early example of this cross-ionization

was observed in Was 49ab by Moran et al. (1992) and has been discussed more recently in Liu et al. (2011) and Keel et al. (2019). These pairs will behave in a similar manner to the synchronous AGN in that is will turn single AGN into dAGN and that it will be more likely to happen in close galaxy pairs.

We qualitatively depict how the merger-induced AGN and correlated AGN interact with the observed AGN excess in Figure 4.2. The merger-induced AGN will generate excess AGN in all three subsamples and will generate more excess AGN at closer separations. The correlated AGN will remove cases from the single AGN sample and give them to the dAGN sample. The rate of correlation will increase with closer separations. In the dAGN sample, the combinations of the merger-induced AGN and correlated AGN will create a large surplus of excess AGN. In the single AGN sample, the merger-induced AGN and the AGN lost to correlated activity will roughly counteract each other so that there is no excess AGN. In the single+dual AGN, the merger-induced AGN will provide a slight excess of AGN and the sample will be unaffected by correlated AGN. Using these three terms, we can create a picture of what is likely happening in our excess AGN.

To account for the correlated AGN, we will need a term, ξ, which will convert some percentage of single AGN to dAGN. This term will also have to be separation dependent with close pairs being the most effected. We can account for this effect by having a percentage of AGN removed from the single AGN in Equation 4.3 such that,

$$\begin{aligned} n_{\rm st+corr}^{\rm sagn} = &\sum_{j=1}^{N_{\rm pair}} \left(1-\xi(r_{{\rm p},j})\right) W_j \, f_{\rm agn}(M_j^t, z_j) \left[1 - f_{\rm agn}(M_j^c, z_j)\right] \\ &+ \sum_{j=1}^{N_{\rm pair}} \left(1-\xi(r_{{\rm p},j})\right) W_j \, f_{\rm agn}(M_j^c, z_j) \left[1 - f_{\rm agn}(M_j^t, z_j)\right]. \end{aligned} \tag{4.5}$$

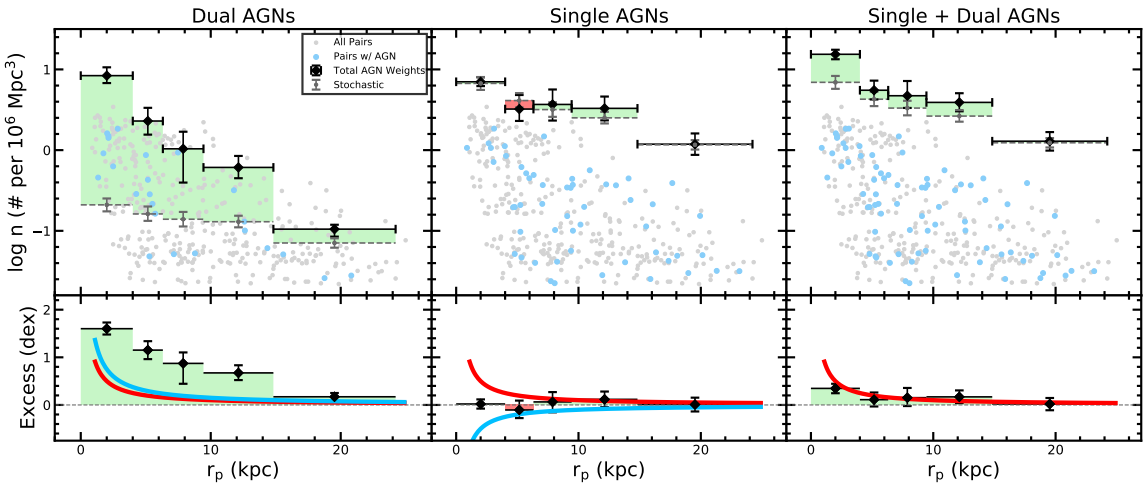

Figure 4.2. Same as Figure 4.1 but qualitatively showing the contributions of merger-induced AGN and correlated AGN in the bottom three panels. The red curves represent the contribution from merger-induced fueling and the blue curves represent how correlated AGN activity is shifting single AGN into the dAGN sample.

The percentage of AGN removed from the single AGN sample are then added to the dAGN sample such that,

$$
\begin{aligned}
n^{\mathrm{dagn}}_{\mathrm{st+corr}} = & \sum_{j=1}^{N_{\mathrm{pair}}} W_j \, f_{\mathrm{agn}}(M^t_j, z_j) \, f_{\mathrm{agn}}(M^c_j, z_j) \\
& + \sum_{j=1}^{N_{\mathrm{pair}}} \xi(r_{\mathrm{p},j}) \, W_j \, f_{\mathrm{agn}}(M^t_j, z_j) \, [1 - f_{\mathrm{agn}}(M^c_j, z_j)] \\
& + \sum_{j=1}^{N_{\mathrm{pair}}} \xi(r_{\mathrm{p},j}) \, W_j \, f_{\mathrm{agn}}(M^c_j, z_j) \, [1 - f_{\mathrm{agn}}(M^t_j, z_j)].
\end{aligned}
\tag{4.6}
$$

If ξ had a value of 0.3, that would mean that 30% of our single AGN are being converted into dAGN through correlated AGN activity. The single+dual AGN sample is agnostic to correlated AGN and will be unchanged by the term.

We attempt find a fit for $\xi(r_{\mathrm{p}})$ using SCIPY's minimization routine. The goal of the fit is the minimize the excess of dAGN seen in the dAGN, single AGN and single+dual AGN

samples. We assume that $\xi(r_{\rm p})$ follows an inverse power-law, $\xi(r_{\rm p}) = a\, r_{\rm p}^{-b}$, since we have a strong excess of dAGN at low separations which rapidly falls with increasing separation. We also impose bounds on the fit that require that ξ is between a value of 0 to 1. A ξ value of 0 means that no single AGN are being converted to dAGN and a value of 1 means that all of our single AGN are being converted into dAGN. Values outside of 0 to 1 are unphysical in this scenario. We fit the parameters, a and b, for $\xi(r_{\rm p})$ in Equations 4.2 and 4.3 with SCIPY following the Powell method (Powell, 1964; Press et al., 2007) and find that $\xi(r_{\rm p}) = 1.29\ r_{\rm p}^{-1}$.

We show the results of this in Figure 4.3. It is immediately clear that ξ alone is unable to account for the surplus AGN that we see. Higher values of ξ will remove excess AGN from the dAGN sample, but higher values of ξ will also increase the excess AGN in the single AGN sample. The solution from the fitting is the solution that evens out the excess AGN between the dAGN and single AGN samples. Remarkably, the excess AGN after accounting for correlated activity in the dAGN and single AGN sample now matches the excess AGN originally seen in the single+dual AGN sample. In all three samples, we see that there is a $\sim$0.4 dex ($\sim$2.5$\times$) excess of AGN at 2 kpc and roughly no excess of AGN at 20 kpc.

To account for this remaining AGN excess, we introduce a merger-induced parameter, λ to our model. This merger-induced parameter will enhance the baseline probability for AGN activity, $f_{\rm AGN}$, such that,

$$f'_{\rm agn}(M, z, r_{\rm p}) = (1 + \lambda(r_{\rm p}))\, f_{\rm agn}(M, z), \tag{4.7}$$

where $f'_{\rm agn}$ is the stochastic AGN rate modified by merger-induced fueling and $\lambda(r_{\rm p})$ is the projected separation dependent enhancement to AGN fueling from merger-induced effects.

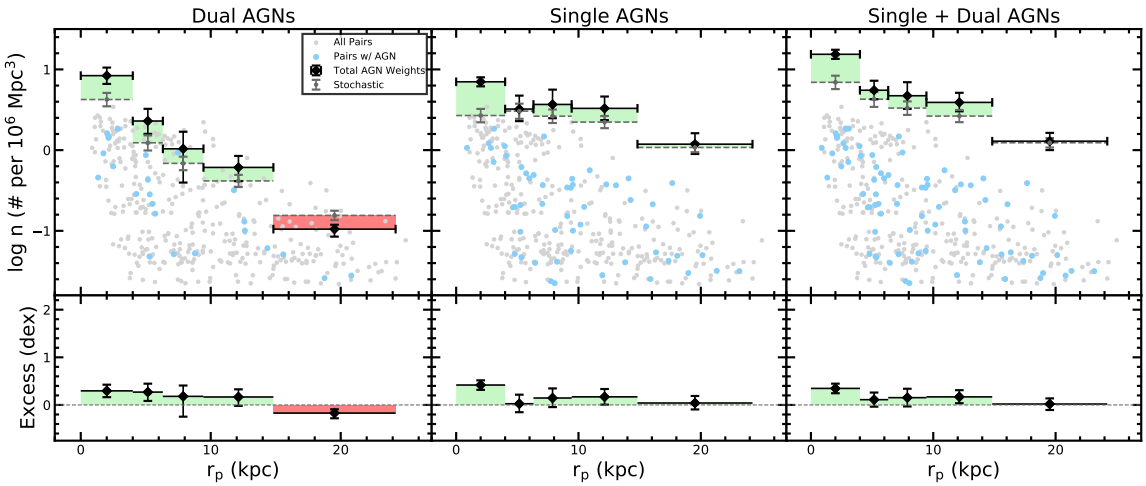

Figure 4.3. Same as Figure 4.1 but applying the correlated AGN term, $\xi(r_{\rm p})$, from Equations 4.6 and 4.5.

This term, $\lambda(r_{\rm p})$, essentially acts as an enhancement to the rate of stochastic AGN such that a value of $\lambda = 1$ would increase the stochastic rate of AGN fueling by a factor of two and a value of $\lambda = 0$ would mean that there is no merger-induced enhancement to the rate of AGN in pairs.

We first want to check if merger-induced fueling can explain the surplus AGN we see without correlated activity. We replace the stochastic fueling terms, $f_{\rm agn}$, from Equations 4.2, 4.3, and 4.4 with the terms modified for merger-induced fueling, $f'_{\rm agn}$. We then find a fit for $\lambda(r_{\rm p})$ with the same method we used for $\xi(r_{\rm p})$. We assume that λ follows an inverse power-law such that $\lambda(r_{\rm p}) = a\, r_{\rm p}^{-b}$. The bounds for $\lambda(r_{\rm p})$ are less strict than those for $\xi(r_{\rm p})$ since λ is just a scale factor for $f_{\rm agn}$. We only require that λ is positive since the factor represents an enhancement to the stochastic rate of AGN. The fit we obtain is $\lambda(r_{\rm p}) = 2.64\, r_{\rm p}^{-1}$.

We show the results of this fit in Figure 4.4. We see that the $\lambda(r_{\rm p})$ is able to resolve

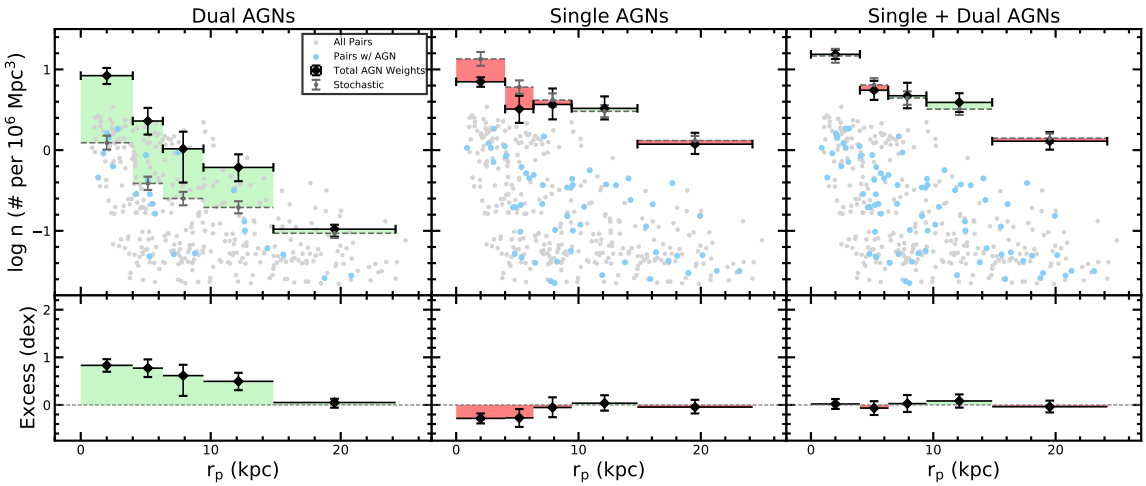

Figure 4.4. Same as Figure 4.1 but applying the merger-induced fueling term, $\lambda(r_{\rm p})$, from Equation 4.7.

the excess AGN we see in the single+dual AGN sample; however, the dAGN sample still shows an excess of AGN and the single AGN sample shows a deficit of AGN. The results seen in the dAGN and single AGN samples seem to follow what we would expect from correlated activity. We are missing a set of single AGN and we have extra dAGN in the same separation bins. This tells us that we need to use a model that includes both correlated AGN activity and merger-induced fueling.

We create a final set of equations for the expected volume density of AGN in our pairs to account for both correlated AGN and merger-induced fueling. To do this we replace $f_{\rm agn}$ with $f'_{\rm agn}$ from Equation 4.7 for the equations which account for correlated activity, Equations 4.6 and 4.5 and the original equation for the single+dual AGN, Equation 4.4 such

that,

$$n^{\rm sagn}_{\rm st+ind+corr} = \sum_{j=1}^{N_{\rm pair}} (1-\xi(r_{{\rm p},j}))\, W_j\, f'_{\rm agn}(M^t_j, z_j, r_{{\rm p},j})\, [1 - f'_{\rm agn}(M^c_j, z_j, r_{{\rm p},j})] \tag{4.8}$$
$$+ \sum_{j=1}^{N_{\rm pair}} (1-\xi(r_{{\rm p},j}))\, W_j\, f'_{\rm agn}(M^c_j, z_j, r_{{\rm p},j})\, [1 - f'_{\rm agn}(M^t_j, z_j, r_{{\rm p},j})],$$

$$n^{\rm dagn}_{\rm st+ind+corr} = \sum_{j=1}^{N_{\rm pair}} W_j\, f'_{\rm agn}(M^t_j, z_j, r_{{\rm p},j})\, f'_{\rm agn}(M^c_j, z_j, r_{{\rm p},j}) \tag{4.9}$$
$$+ \sum_{j=1}^{N_{\rm pair}} \xi(r_{{\rm p},j})\, W_j\, f'_{\rm agn}(M^t_j, z_j, r_{{\rm p},j})\, [1 - f'_{\rm agn}(M^c_j, z_j, r_{{\rm p},j})]$$
$$+ \sum_{j=1}^{N_{\rm pair}} \xi(r_{{\rm p},j})\, W_j\, f'_{\rm agn}(M^c_j, z_j, r_{{\rm p},j})\, [1 - f'_{\rm agn}(M^t_j, z_j, r_{{\rm p},j})],$$

$$n^{\rm s+dagn}_{\rm st+ind+corr} = \sum_{j=1}^{N_{\rm pair}} W_j\, f'_{\rm agn}(M^t_j, z_j, r_{{\rm p},j}) + \sum_{j=1}^{N_{\rm pair}} W_j\, f'_{\rm agn}(M^c_j, z_j, r_{{\rm p},j}) \tag{4.10}$$
$$- \sum_{j=1}^{N_{\rm pair}} W_j\, f'_{\rm agn}(M^t_j, z_j, r_{{\rm p},j})\, f'_{\rm agn}(M^c_j, z_j, r_{{\rm p},j}).$$

We now want to find a fit for both $\xi(r_{\rm p})$ and $\lambda(r_{\rm p})$ simultaneously for Equations 4.9, 4.8, and 4.10 using the same bounds we used previously for ξ and λ. We find that the correlated AGN activity, $\xi(r_{\rm p})$, follows an inverse power-law of,

$$\xi(r_{\rm p}) = 1.14\, r_{\rm p}^{-1}\, (r_{\rm p}/{\rm kpc})\,, \tag{4.11}$$

and the merger-induced enhancement, $\lambda(r_{\rm p})$, follows an inverse power-law function of,

$$\lambda(r_{\rm p}) = 3.25\, r_{\rm p}^{-1}\, (r_{\rm p}/{\rm kpc})\,. \tag{4.12}$$

The power-law index in both equations were found to be close to 1 in both cases, so we fixed the their indices to 1 and resolved their scale factors. Doing this, we find that the model fit

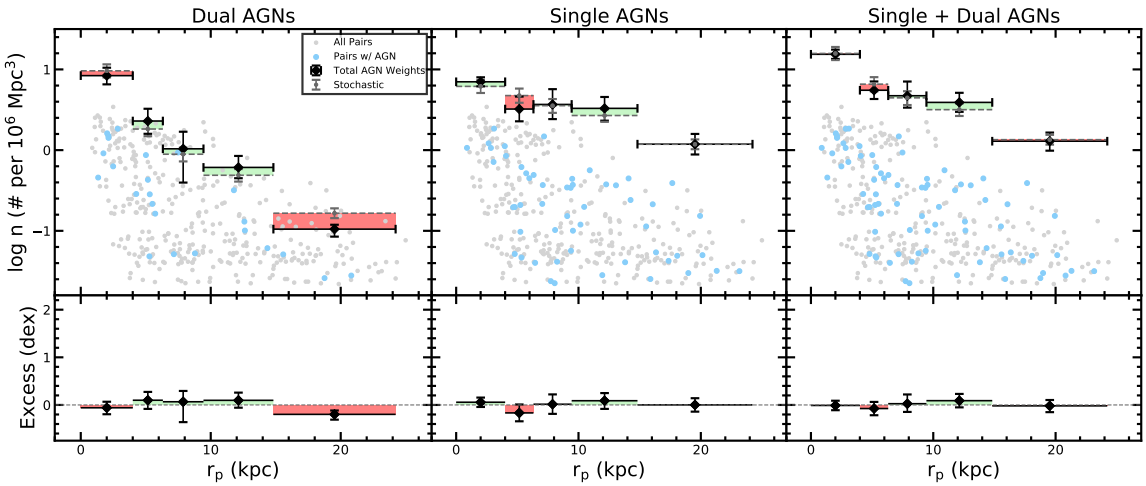

Figure 4.5. Same as Figure 4.1 but applying the correlated AGN term, $\xi(r_{\rm p})$, and the merger-induced term, $\lambda(r_{\rm p})$, from Equations 4.9, 4.8, and 4.10.

has a reduced $\chi^2 = 0.33$. Now applying both the $\lambda(r_{\rm p})$ and $\xi(r_{\rm p})$ to Figure 4.1, we are able to flatten out the excess AGN and create a complete model for the AGN in our pair sample in Figure 4.5.

From Equation 4.11 we can predict that at 10 kpc, 11.4% of single AGN will be converted into dAGN through correlated activities. The rate of correlated activities falls under 5% around 25 kpc and rises to 100% around 1 kpc. Based on our fit to ξ, separations under 1.14 kpc are technically unphysical as they would imply over 100% of single AGN are being converted into dAGN though this is not an issue with our data since our smallest separation bin is at 2 kpc. Equation 4.12 suggests that at 10 kpc we would expect merger-induced fueling to enhance the rate of stochastic fueling by a factor of 1.3×. This factor rises to 4.25× at 1 kpc and falls to 1.13× at 25 kpc.

In Figure 4.6, we show the relative contributions of each component of our AGN volume density model. Since the correlated AGN and merger-induced fueling terms mod-

ify the stochastic AGN rate, they cannot be separately shown without the contribution of stochastic fueling. We see that the baseline volume density expected from stochastic fueling increases with smaller separations. In the dAGN, we see that stochastic fueling contributes a small portion of the total model while in the single+dual AGN sample the stochastic fueling contributes a substantial portion of the model. The merger-induced fueling component is substantial at the lowest separation bin, 2.5 kpc, for both the dAGN and single+dual AGN sample but then rapidly falls with increased separation. The correlated AGN term is also strongest at low separations in the dAGN; however, it falls away at a slower rate.

In Figure 4.6, we see that the stochastic+merger-induced model can only account for about a quarter of the AGN volume density that we observe. The stochastic+correlated model is only able to account for about half of the observed volume density the we observe. Only when we use a model that accounts for stochastic fueling, merger-induced fueling, and correlated AGN activity can we reproduce the observed AGN volume density. In the single+dual AGN sample, the merger-induced fueling component accounts for about half of the model at small separations after which the model becomes increasingly dominated by stochastic fueling.

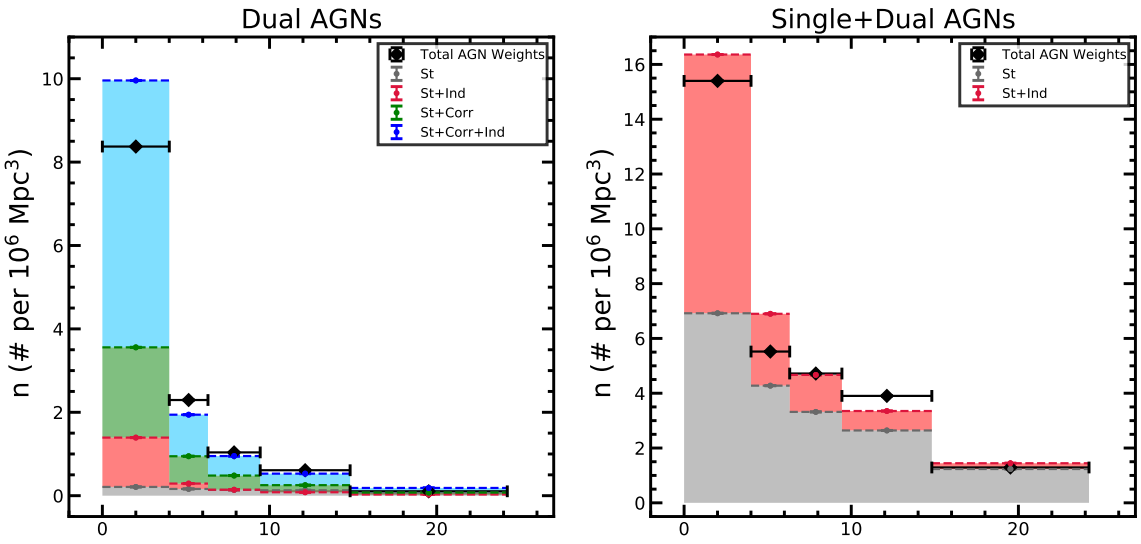

Figure 4.6. The relative contributions of stochastic fueling (grey), stochastic fueling and merger-induced fueling (red), stochastic fueling and correlated AGN (green), and stochastic fueling, merger-induced fueling, and correlated AGN (blue) in our modeled expected volume density of AGN in dAGN (left) and single+dual AGN (right).

CHAPTER 5

ELEVATED BLACK HOLE ACCRETION RATES IN PAIRED GALAXIES

The source of the powerful emission we observe from AGN is a result of material accreting onto the black hole. As the matter falls towards the black hole, gravitational potential energy is converted into kinetic energy. When the matter spirals about the black hole, the viscosity of the material converts the kinetic energy into thermal and radiant energy. We can use the observed radiant energy to estimate the rate of mass accretion onto the black hole with,

$$L_{\rm bol} = \eta \dot{M} c^2, \tag{5.1}$$

where $L_{\rm bol}$ is the bolometric luminosity, η is the accretion efficiency, $\dot{M}$ is the mass accretion rate, and c is the speed of light.

Unfortunately, direct measurements of the bolometric luminosity for AGN are difficult as they emit across several wavelength regimes and many of those wavelength regimes are obscured. While we cannot directly use the bolometric luminosity, there are some good proxies for it. In the optical regime, the [O III] luminosity is often used as a proxy for the bolometric luminosity (Heckman and Best, 2014). The [O III] line is useful as it is strong enough to be visible in most galaxies and it is linearly proportional to the bolometric luminosity. OB stars can contribute to to the [O III] luminosity observed in a galaxy; however, an AGN will produce [O III] lines that are much more luminous than those from OB stars.

Since the [O III] luminosity can be used as a tracer of the black hole accretion rate, we want to use this line to see if the black holes in paired galaxies accrete materials at higher

rates than those found in isolated galaxies. We correct our luminosities for reddening using the reddening curve from Calzetti et al. (2000), assuming $R_V = 3.1$ and case-B recombination, $H\alpha/H\beta = 2.86$. As we had shown in Figure 3.9, the fraction of AGN in our control sample is a function of the galaxy's stellar mass and redshift. This tells us that the AGN in paired galaxies will need to be compared against AGN in control galaxies with similar stellar masses and redshifts. We plot the [O III] luminosity as a function of the stellar mass and redshift in Figure 5.1. We find that the [O III] luminosity increases with both higher stellar masses and redshift.

We now use Figure 5.1 to match AGN in pairs to AGN in control galaxies. We define a grid that is 0.01 in redshift and 0.2 dex in stellar mass. For each AGN in paired galaxies, we take the median [O III] luminosity of the control AGN which share the same grid space as the AGN in the paired galaxy. We then take the logarithmic difference between the paired galaxy's luminosity and the median luminosity of the controls. We do this separately for each paired galaxy which hosts an AGN.

In Figure 5.1, we see that a number of the paired galaxies are not on MaNGA's typical stellar mass−redshift space. This is from the recalculated stellar masses where the stellar masses from the NSA catalog are being split between the two paired galaxies. Galaxy pairs with wide mass ratios will displace the paired galaxy further off of the control galaxies' distribution. To account for this, we require that each paired galaxy have at least 3 controls which share the same stellar mass−redshift space. If the paired galaxy fails to acquire 3 controls, it is removed from the subsequent analysis.

We show the excess [O III] luminosity of the AGN in paired galaxies in Figure 5.2. We

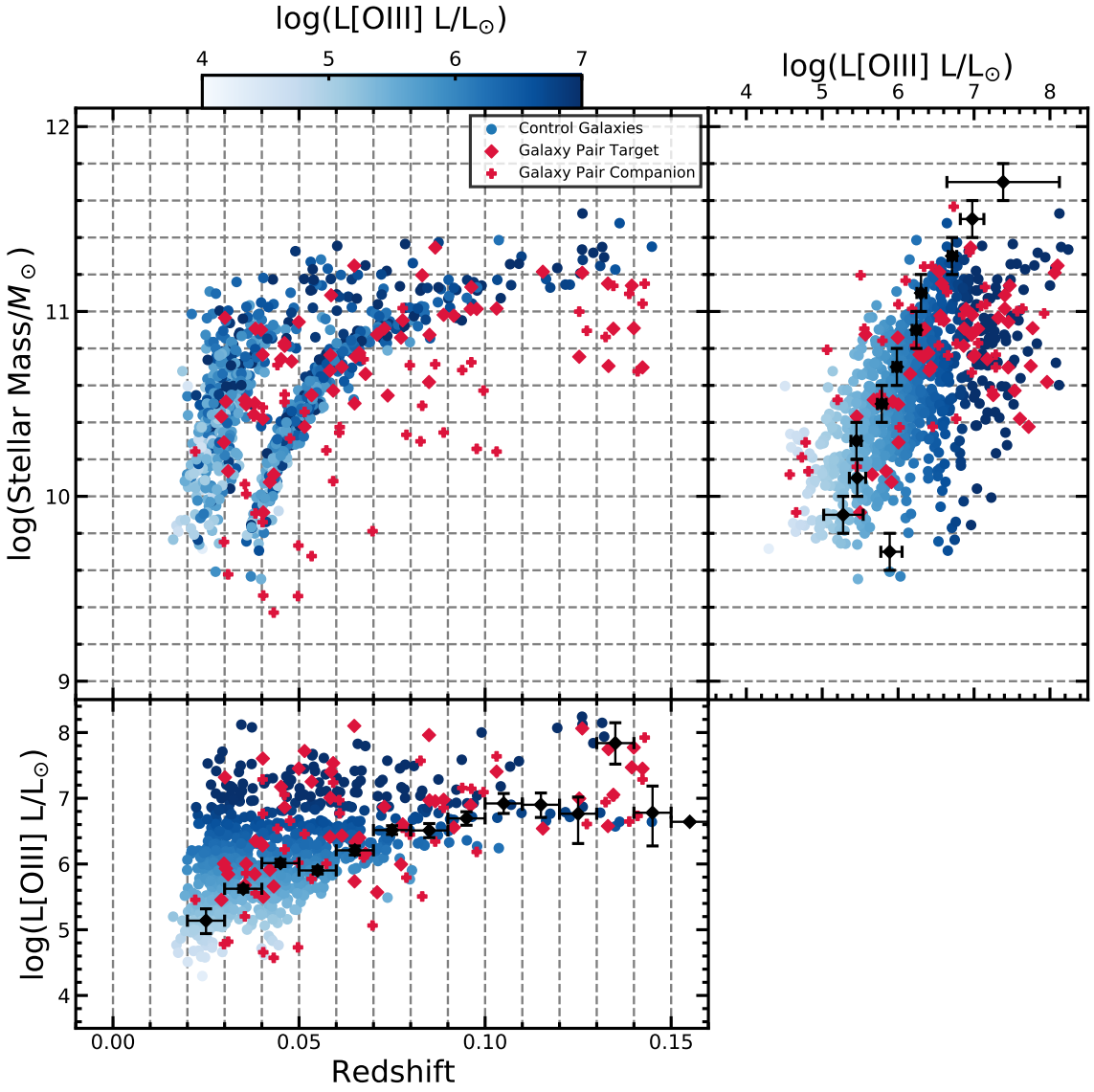

Figure 5.1. The [O III] Luminosity of the AGN in the pair and control samples as a function of the stellar mass and redshift. The central panel shows the [O III] luminosity (whose values are represented by the color-bar above the panel) as a function of the stellar mass and redshift. The red diamonds represent MaNGA targets in pairs and the red crosses represent the MaNGA target's companion galaxy. The right panel shows the [O III] luminosity as a function of the stellar mass. The black squares represent the median [O III] luminosity within a discrete stellar mass bin. The vertical bars represent the bin size and the horizontal bars represent the 1σ confidence intervals computed through bootstrap resampling. The bottom panel is identical to the right panel, but now showing the [O III] luminosity as a function of the redshift. The grey dashed lines in the panels represent the grid spacing on which we match galaxy pairs to controls.

take the median [O III] luminosity in projected separation bins, which are 5 kpc wide, and calculate the vertical error bars with the bootstrap resampling method mentioned in Section 4.1. Above a projected separation of 15 kpc, we see a $\Delta\log(L[\mathrm{O\,III}])$ that is consistent with the control AGN. Under 15 kpc, we find a mild enhancement to the $\Delta\log(L[\mathrm{O\,III}])$ between $0.1-0.4$ dex which $1.25\times-2.5\times$ higher than the [O III] luminosities of the control AGN. Along with this, we see that there are a few AGN in galaxy pairs which feature $\Delta\log(L[\mathrm{O\,III}])$ that are $10-100\times$ brighter than their control AGN. This shows us that some galaxy pairs are subject to massive enhancements to the black hole fueling rate.

Assuming Equation 5.1, we see that the luminosity and the mass accretion rate are proportional to one another. This means that we find mass accretion rates in AGN in paired galaxies that are $1.25\times-2.5\times$ higher than those in isolated control AGN. This demonstrates that galaxy mergers can play a significant role in the mass growth of the SMBH found in the centers of galaxies.

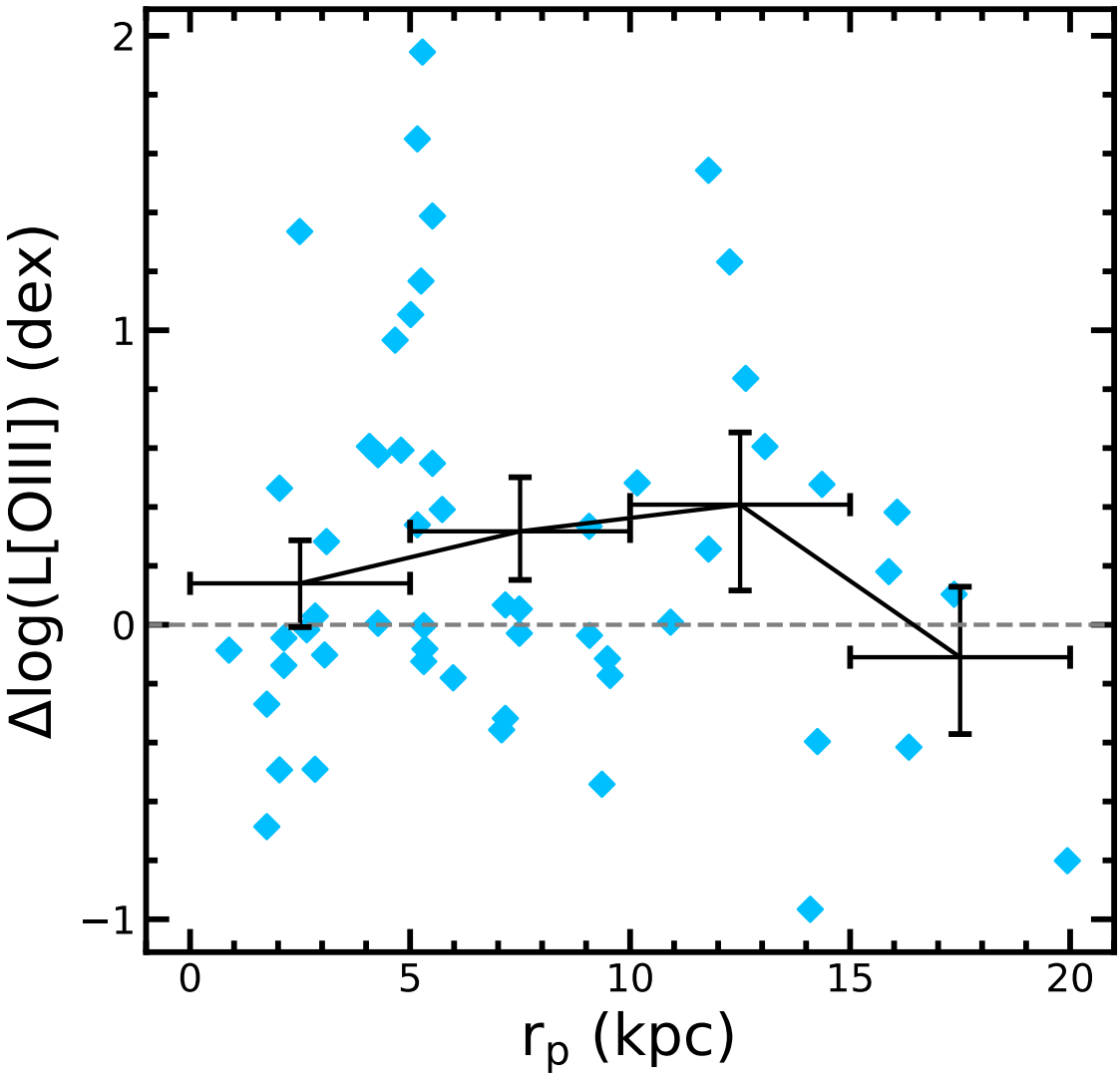

Figure 5.2. The enhancement to the [O III] in the AGN in paired galaxies with respect to those in the control AGN. The blue diamonds represent individual $\Delta\log(L[\mathrm{O\,III}])$ for a pair and its controls selected to have a similar stellar mass and redshift. The black line shows the median $\Delta\log(L[\mathrm{O\,III}])$ across separate projected separation bins. The horizontal bars represent the bin size and the vertical bars represent the 1σ confidence intervals computed through bootstrap resampling.

CHAPTER 6

DISCUSSION

6.1 Mass Ratio Dependent Duty Cycle of AGN in Pairs

In Chapter 4, we have assumed that the volume density of AGN is primarily a function of the projected separation; however, it may depend on other merger parameters. In Paper II, we observed that merger-induced star formation was dependent on both the projected separation and the mass ratio.

We rebuild Figure 4.1 but using the mass ratio between the pairs to bin the volume densities in Figure 6.1. For this figure, I expand the allowed mass ratio cut for the pair sample to $\Delta\log(M/M_{\odot}) \leq 2.0$. In the single AGN and single+dual AGN samples, we see a roughly flat enhancement to the volume density of AGN across the mass ratio range of about 0.2 dex ($\sim$1.6$\times$). In the dAGN sample, the excess volume density peaks between $\Delta\log(M/M_{\odot})$ = 0.0$-$1.0 by 1.3 dex ($\sim$20$\times$) and falls to 0.9 dex ($\sim$8$\times$) between $\Delta\log(M/M_{\odot})$ = -0.5$-$1.0 and 1.5.

Overall, we do not see any correlation between the excess volume density of AGN and the mass ratio between the galaxy pairs. This shows us that our AGN model in Section 4.2 does not need to depend on the mass ratio between the galaxy pairs.

6.2 Comparison to Fu et al. 2018

In this work we find greater excesses of AGN in the pair sample than we did in our previous work in Paper I. The work in Paper I was done using an earlier MaNGA data release (DR14) in which only $\sim$2700 of the 10,000 MaNGA datacubes have been collected.

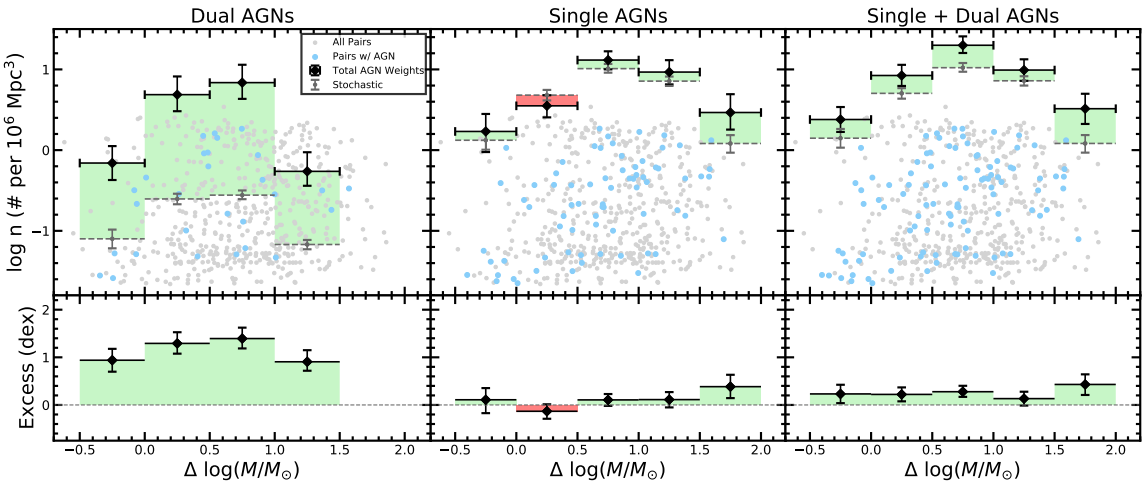

Figure 6.1. Same as Figure 4.1 but calculated the observed and expected volume densities as a function of the mass ratio.

The galaxy pairs were also selected in a slightly different way in the work. In Paper I, r-band magnitude differences of $\Delta\mathcal{M}_{\rm r} < 2.5$ in the Petrosian, Model, and PSF magnitudes (which ever one had the smallest $\Delta\mathcal{M}_{\rm r}$) were used to preselect galaxy pair candidates in MaNGA. After this preliminary stage, we visually analyzed the flagged pair candidates in the SDSS pseudocolor images to remove over-deblended sources. The objects that made it past this step then had their spectra extracted and modeled so that we could impose stricter requirements like relative line-of-sight velocities and mass ratios. Using this pair selection technique, Paper I finds 105 galaxy pairs. In Paper II, we started with the visual identification of objects in the SDSS pseudocolor images after which we extracted and modeled the spectra of all identified objects. In this work, we find 426 pair systems which is what we would expect from a MaNGA sample that is 4× larger.

In this work, we calculate the cumulative pair fraction of 4.33% ± 0.29% in Figure 3.4. Paper I performs a similar analysis and finds a cumulative pair fraction of 3.4% ± 0.5%.

The pair fraction that we find is consistent with what we found in our previous work. This tells us that the different pair selection methods that we used in this work and Paper I yield equivalent results.

The AGN selection with the BPT and WHAN diagrams are the same with the exception that we are using a stricter EW(Hα) cut of 6Å instead of the usual 3Å cut. Paper I finds 50 AGN among the 105 galaxy pairs along with a sample of 14 dAGN. We find 102 AGN with 24 dAGN. Despite the 4× larger sample size, we only find twice the AGN as we had in Paper I. This may be due to the stricter EW(Hα) cut that we employ in this work. This cut means that we will have fewer, but stronger, AGN in the sample.

We use the same method to calculate the AGN volume density; however, we find more excess AGN in this work than we did in Paper I. In Figure 6.2, we compare the excess AGN volume densities in this work in comparison to those in Paper I. For dAGN, we find an excess of 1.6 dex (40×) for close pairs while Paper I finds an excess of 0.8 dex (6.3×). In the single AGN, Paper I finds a deficit 0.1 dex (1.25×) while we find zero excess of single AGN. In the single+dual AGN sample, Paper I finds no excess AGN while we find a 0.4 dex (2.5×) excess at close separations. Overall, we find a greater excess of dAGN in this work and we find an excess of single+dual in this work where we observed none in the previous work.

These differences may be due to the larger sample size that we have access to in this work and from our more strict cuts for the AGN selection. The use of an EW(Hα) $\geq$ 6Å cut selects for stronger AGN. If galaxy mergers can induce higher rates of mass accretion onto the SMBH, we may expect a higher fraction of powerful AGN in the pair sample with

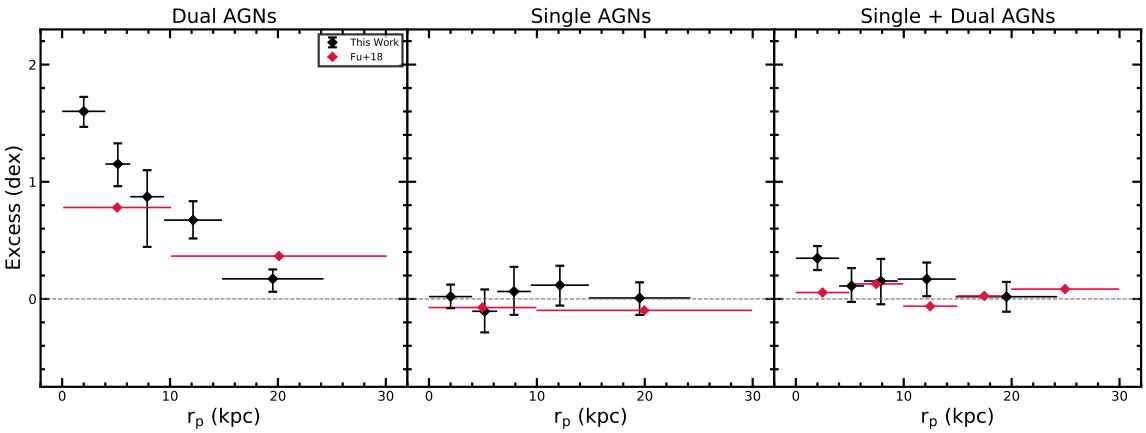

Figure 6.2. The AGN excess in comparison to the random pairing of AGN from Figure 4.1 as a function of the projected separation. The figure is split into dAGN (left) single AGN (middle) and single+dual AGN (right). The results of this work (black diamonds) are shown alongside the previous results from Paper I (blue diamonds).

respect to the isolated control galaxies.

Paper I estimates the rate of AGN correlation, ξ, based on the excess of dAGN. Paper I estimates that ξ is 15% at separations of 20 kpc and 40% at 5 kpc. In our work, Equation 4.11 predicts a rate of correlation that is 6% at 20 and kpc 20% at 5 kpc. The rates of correlation in this work are lower because we include a second term in our model, merger-induced fueling, where Paper I only includes a correlated AGN term. The results of this is that the excess of dAGN is split between correlated activity and merger-induced fueling. We are able to include the merger-induced fueling term in this work because we now observe an excess AGN in the single+dual AGN sample where we did not observe this excess in the previous work.

6.3 Comparison to Observations

Now that we have discussed the results of this work compared to our previous work, we want to compare the results with other previous works. In Figure 6.3, I show the AGN excess of the singe+dual AGN sample from our work and other previous works. These works include the optically selected AGN from Ellison et al. (2013), the optical and infrared selected AGN from Satyapal et al. (2014), the X-ray, optical, infrared, and radio selected AGN from Silva et al. (2021), and the AGN excess in pairs predicted by the Eagle simulation in McAlpine et al. (2020).

The pair samples in Ellison et al. (2013) and Satyapal et al. (2014) are based on the pair sample from Ellison et al. (2008). This sample consists of ∼1700 galaxy pairs in SDSS's spectroscopic survey. These pairs share a similar redshift range ($z < 0.15$) and relative velocity cut ($\Delta v < 500$ km s^{-1}), but it has a stricter mass ratio limit (no more than 4:1) and a wider projected separation limit ($r_{\rm p} < 115$ kpc). Because of the fiber collision in SDSS, the galaxy pairs with angular separations under 55″ must be selected in cases where there are overlapping tiling plates or in fields with repeated observations. This means that the pairs selected within 55″ are selected from a different survey area than the pairs with angular separations above 55″. Ellison et al. (2008) deals with this by randomly culling 67.5% of the pairs beyond 55″. Ellison et al. (2013) expands this sample to include 97 post-merger galaxies. These post-merger galaxies are identified through the citizen science project, Galaxy Zoo, which has volunteers classify the morphologies of the galaxies.

Ellison et al. (2013) and Satyapal et al. (2014) then build a sample of control galaxies in SDSS that have no spectroscopic companion within a projected separation of 115 kpc and

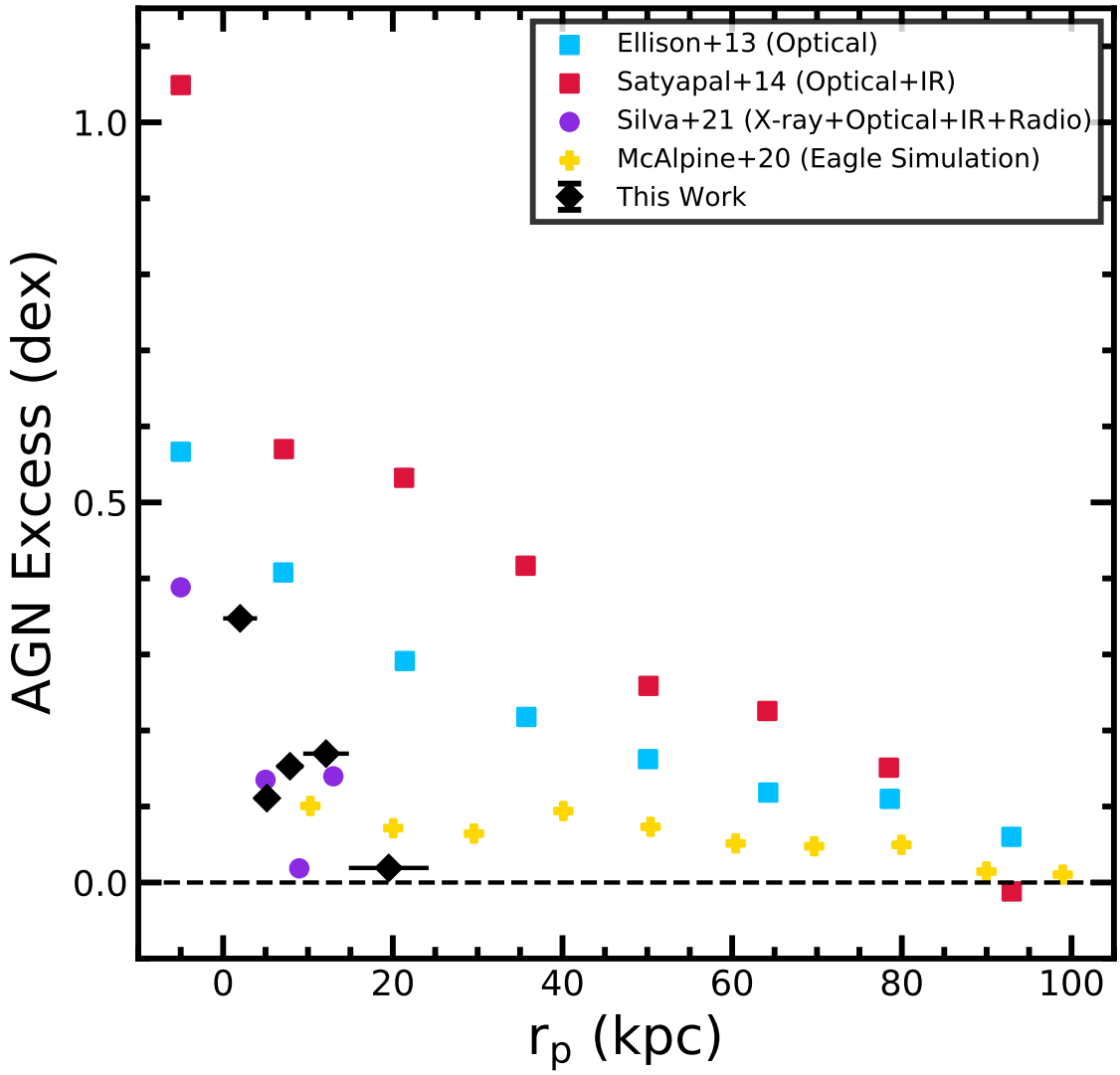

Figure 6.3. We show the AGN excess from this work (black) and other previous works; Ellison et al. (2013) (blue), Satyapal et al. (2014) (red), Silva et al. (2021) (purple), and McAlpine et al. (2020) (yellow). The data points below a projected separation of 0 kpc represent a sample of post-merger galaxies.

a line-of-sight velocity of 10,000 km s^{-1}. The paired galaxies are then matched to controls with similar stellar masses, redshifts, and environmental densities. If less than five controls are found for a paired galaxies, the limits on the stellar masses, redshifts, and environmental densities are iteratively expanded until five controls are found.

Ellison et al. (2013) uses the AGN selection cut from Stasińska et al. (2006) which is a more relaxed cut than the one from K03 (Equation 3.9) which we use. Satyapal et al. (2014) uses the same pair and control sample selections from Ellison et al. (2013). Instead of using BPT analysis to identify AGN, Satyapal et al. (2014) uses WISE color cuts to select AGN.

The resulting AGN fractions are shown in Figure 6.3. In Ellison et al. (2013), the AGN fraction in paired galaxies is $\sim$2.5$\times$ higher than controls at a projected separation of 10 kpc. This excess falls to one at a separation of 90 kpc. Their AGN excess is roughly consistent with ours at close separations; however, our excess falls to one at a projected separation of only 20 kpc. The excess AGN seen in Satyapal et al. (2014) is roughly twice the excess seen in Ellison et al. (2013) for all separations.

These two works also include a set of post-merger galaxies in their sample. These post merger galaxies are the final stage of a merging galaxy as they coalesce into a single galaxy and are expected to feature the greatest merger-induced effects. Ellison et al. (2013) finds an AGN excess of $\sim$3.75$\times$ while Satyapal et al. (2014) finds an AGN excess of $\sim$11$\times$, which is higher the the AGN excesses seen in the closest galaxy pairs.

Between our works, Ellison et al. (2013) has a stricter mass ratio cut of 4:1 while our pairs have a mass ratio cut of 10:1. Ellison et al. (2013) also uses a more relaxed AGN

selection than ours. With SDSS's redshift range, all of pairs in Ellison et al. (2013) under 40 kpc will be in overlapping tiles or repeat observations. Beyond 40 kpc the pairs will be from both overlapping tiles and the full SDSS sample. This tells us that the differences in our results are not just from SDSS's fiber collision radius.

The large excess of AGN seen in Satyapal et al. (2014) is likely due to the usage of infrared to select AGN. Infrared selection can identify AGN that have been optically obscured by dust. The AGN in galaxies undergoing mergers are likely subject to more dust obscuration than those in isolated galaxies since the merger may be able to throw dust in between the observer and the AGN. Weston et al. (2017) suggests that as many as 50% of the AGN in pairs may be optically obscured by dust, which corresponds to Satyapal et al. (2014) finding an AGN excess that is almost twice are large as the one in Ellison et al. (2013).

Ellison et al. (2013) also studies the [O III] luminosity in paired galaxies. They find that post-merger galaxies have [O III] luminosities that are 0.9 dex (8×) higher than controls. In the paired galaxies, the [O III] luminosities are 0.5 dex (3×) higher at separations of 5 kpc. This enhanced [O III] luminosity falls to 0.15 dex (1.4×) at 75 kpc. In our work, the [O III] luminosities in pairs are 0.2−0.4 dex higher than controls, but ours do not show a clear evolution with the projected separation. This may be because of our limited projected separation range.

Silva et al. (2021) builds a sample of galaxy pairs from the 3D-HST catalogs (Skelton et al., 2014; Momcheva et al., 2016). Pairs are selected to be between 3−15 kpc, within a mass ratio of 4:1, and within a redshift difference of 0.001. Doing this they find 58 galaxy pairs. Silva et al. (2021) then crossmatches this sample with Chanda (X-ray), 3D-HST

(optical), Spitzer/IRAC (Infrared), and VLA (Radio) to identify 16 AGN across several wavelength regimes. They also build a sample of post-merger galaxies by assuming that all of the starbursts in the non-merger sample are actually coalescing pairs.

Silva et al. (2021) finds an AGN excess in pairs that is less than 1.5× higher than what is seen in controls. The post-merger galaxies feature an excess that is ∼2.5× higher than controls. They find the the AGN fraction in pairs is consistent with the AGN fraction in controls, while the post-merger fraction is higher than the AGN fraction in controls. The AGN excess found in this work is roughly equivalent to the AGN excess we observe in this work; however, the pair and AGN sample in Silva et al. (2021) is much smaller than the pair and AGN samples that we use in this work.

Pan et al. (2019) builds a sample of 682 paired galaxies in MaNGA DR15 (4691 galaxies; Aguado et al. (2019)) by crossmatching MaNGA targets with the NSA catalog. The galaxies are selected within a line-of-sight velocity of $\Delta v < 500$ km s^{-1} and a projected separation limit of $r_p < 70$ kpc. They also note that 10% of these cases have both galaxies covered by a separate MaNGA IFUs. This selection method misses the paired galaxies in which both components are contained within a single IFU. To recover these, Pan et al. (2019) visually inspects the MaNGA fields for galaxies showing clear tidal features. This adds an additional 24 paired galaxies and 85 post-merger galaxies.

Jin et al. (2021) uses the paired galaxy and post-merger samples from Pan et al. (2019) to study AGN in MaNGA. They study the rate of AGN in pairs as a function of merger sequence (approach to the first pericenter, passing through the first pericenter, approach or decent from the apocenter, and then the coalescence of the two galaxies into a post-merger)

in the MaNGA survey. The study found no evolution of the AGN fraction across different merger sequences and found no difference between the rate of AGN in galaxy pairs and AGN in isolated galaxies. The AGN rates here were calculated as ratios of the number of AGN in pairs versus the number of AGN in isolated galaxies. As we showed in Figure 3.9, there is a dependence between the rate of AGN in galaxies and the stellar masses of the galaxies. There is also a known relation between the fraction of AGN in galaxies and their redshift; however, the redshift range of MaNGA is not large enough for us to see this. This means that the paired galaxies hosting the AGN need to be compared against controls that are matched in stellar mass and redshift. Further, MaNGA is not a volume limited survey as the survey's volume changes as a function of the luminosity. This means that the ratio between the number of AGN in galaxies and the number of galaxies is not representative of the actual set of galaxies in the universe. This is why we employ the $1/V_{max}$ method to recover a volume limited sample.

Jin et al. (2021) also compares the surface brightness of [O III] between the AGN in pairs and the AGN in control galaxies using the MaNGA survey. They find that the [O III] surface brightness is 0.13 dex higher in the AGN in pairs than in the AGN in isolated galaxies. If we take the median $\Delta\log(L[\mathrm{O\,III}])$ of our whole AGN pair sample, we find an enhancement to the [O III] luminosity that is 0.1 dex higher in pairs than in control galaxies which is consistent with the results found by Jin et al. (2021).

We find that our AGN excess is in good agreement with previous measurements of the AGN excess in paired galaxies. The AGN excess that we observe is generally on the lower side in comparison to previous works and our separation range is much shorter. One

potential problem is that our sample will miss galaxy pairs in which one galaxy is in the MaNGA IFU and the another is just outside of the IFU. This means that our pair sample is incomplete at certain separations depending on the IFU size. On the other hand, by using this pair selection that is entirely contained in the MaNGA survey, we can control for the well known biases of the MaNGA survey. Our pair sample also contains no post-merger galaxies since our pair selection method requires two distinct galaxy cores.

6.4 Comparison to Simulations

McAlpine et al. (2020) studies the AGN fraction in pairs with the EAGLE simulation (Evolution and Assembly of GaLaxies and their Environment; Crain et al. (2015); Schaye et al. (2015)). Paired galaxies are selected to be major mergers with 4:1 mass ratios and to have 3D physical separations under 100 kpc. The AGN are selected to have bolometric luminosities greater than $L_{\rm bol} \geq 10^{43}$ erg s^{-1} and Eddington rates greater than $\lambda_{\rm edd} \geq 10^{-2}$, where $\lambda_{\rm edd}$ is the ratio between the bolometric luminosity and the Eddington Luminosity. Control galaxies are selected to have similar redshifts, stellar masses, halo masses, gas masses, and black masses as the paired galaxies that they are matched to. In Figure 6.3, we show the AGN excess from McAlpine et al. (2020) in major mergers with redshifts under $z \leq 1.0$. The AGN excess is weaker than those found Ellison et al. (2013) and Satyapal et al. (2014) at all separations. At 10 kpc, McAlpine et al. (2020) finds a AGN excess of $\sim$1.3$\times$ which is similar to, but slightly smaller than, the excess we find at the same separation ($\sim$1.6$\times$).

There are a few key differences between observational studies and simulations like McAlpine et al. (2020). First, the separations in the simulations are real 3D separations and not 2D projected separations that assume that the two galaxies are at the same distance

along our line-of-sight. Second, the merger simulations can tell if the paired galaxies have or have not interacted yet. With observations, we only have a snapshot of the merger event. We do not know if the two galaxies are on their first approach (and have not interacted yet) or if they are between their first or second pericenter. Third, simulations can tell if a galaxy hosts an AGN without observational effects like dust obscuration. Despite these differences, our results are in good agreement with those from McAlpine et al. (2020).

High-resolution hydrodynamical simulations have predicted that AGN activity generally increases with more advanced merger-stages but especially so as the pair coalesces into a post-merger galaxy (Van Wassenhove et al., 2012; Capelo et al., 2017). Van Wassenhove et al. (2012) finds that most dAGN activity should occur below projected separations of 10 kpc. We find that most of our dAGN do have projected separations below 10 kpc; however, about a third of the sample lies between 10−20 kpc. Our model suggests that correlated activity and merger-induced AGN is most influential at close separations. This suggests that these dAGN with wide separations may be largely due to the random pairing of stochastically induced AGN.

Capelo et al. (2017) predicts that in a minor merger the less massive companion will feature more AGN activity than the more massive companion which shows little to no AGN activity. In major mergers, the secondary galaxy is large enough to not only incite AGN activity in the primary but also incite higher levels than what would be seen in minor mergers. In figure 6.1, we see that major and minor mergers display similar excesses of AGN. Also in minor mergers, we find that the more massive galaxy and less massive galaxy in the pair also display similar excesses of AGN.

CHAPTER 7

SUMMARY AND FUTURE WORK

In this work, we constructed a catalog of all spectroscopic objects which fall within the footprint of the MaNGA survey. From this, we built a sample of paired galaxies and AGN in the survey. Specifically we did and found the following.

1. We constructed a spectroscopic catalog of 15,592 objects within MaNGA's field-of-view, of which there are 11,546 galaxies, 1385 stars, and 2661 objects with poor S/N or ambiguous spectra. Among the identified galaxies we found 10,988 galaxies whose redshifts are consistent with the IFU's target galaxy (this number includes the MaNGA targets), 451 foreground/background galaxies, 23 high redshift QSOs, and 84 galaxies which host broad-line AGN.

2. We found 426 interacting galaxy systems including 387 pairs, 37 triplets, 1 quadruplet, and 1 quintuplet. With this pair sample, we found a cumulative pair fraction of 4.33% $\pm$ 0.29% in the MaNGA survey.

3. Among our 387 pairs, we found 102 AGN, among these we found; 59 composite starburst/AGN, 18 LINERs, 17 type II Seyferts, and 8 type I Seyferts. Among these galaxy pairs, we also found a sample of 24 dual AGN systems. We also found a dual AGN system, MaNGA plate-IFU 9892-6102 (Mrk 883), in which both galaxies' cores feature broadened emission line features. Alongside our galaxy pairs we create a sample of 872 AGN in isolated control galaxies. Among these AGN we found; 613 composite

starburst/AGN, 70 LINERs, 126 type II Seyferts, and 63 type I Seyferts.

4. We found that the AGN in galaxy pairs have a volume density that is 2.5× higher than what would be expected by random pairing at close separations. This excess of AGN falls to zero around 20 kpc. In dAGN, we found a volume density of AGN that is 40× higher than what would have been expected by random pairing at close separations. This excess of AGN falls to 1.6× at separations of 20 kpc. We found that the observed excess in the volume density of AGN cannot be described by correlated AGN activity or merger-induced fueling alone. Rather, a model that accounts for stochastic fueling, merger-induced fueling, and correlated AGN activity is required to model the observed volume density of AGN in our pair sample.

5. We found no correlation between the AGN volume density and the mass ratio between the two galaxies. This seems to indicate that major and minor mergers generate AGN at similar rates. We also observe that the AGN in the more massive galaxy and less massive galaxy of a minor merger show a similar excess of AGN.

6. We found that the AGN in paired galaxies feature higher levels of [O III] luminosity with respect to the AGN in isolated control galaxies by a factor of $0.1-0.4$ dex. The enhanced [O III] luminosity is linearly proportional to the mass accretion rate onto the black holes and tells us that the black holes in galaxy pairs receive more fuel than black holes in isolated galaxies.

With this, we have been able to demonstrate that galaxy mergers are able to induce AGN activity in the centers of galaxies. We also show that the AGN induced by galaxy

interactions receive more fuel in comparison to those induced by stochastic processes. This shows us the impact that galaxy mergers have had on the development of the black holes in the centers of the massive galaxies in the nearby universe.

There are a number of things that may be added to this line of study in future works. Much of the major work to be done in the future would be to crossmatch the optically selected AGN we found in pairs with surveys in other wavelength regimes. The WISE (Wide-Field Infrared Survey Explorer) source catalog (Wright et al., 2010) has been used in many previous works to select AGN by infrared color cuts. Weston et al. (2017) showed that ∼50% of AGN may be optically obscured by dust and many works found higher AGN fractions in pairs when using infrared selected AGN (Satyapal et al., 2014; Weston et al., 2017; Ellison et al., 2019; Gao et al., 2020). One potential issue when using WISE with our work is WISE's lower spatial resolution, ∼6″ in three of its color bands and 12″ in the fourth. In our closest pairs, we may not be able to separately resolve which galaxy hosts the infrared selected AGN. This is particularly problematic if we want to use WISE to confirm the dAGN in our sample.

The Chandra X-ray Observatory's source catalog (Evans et al., 2010) would be a good X-ray survey to study our sample with. Chandra's spatial resolution of 0.″5×0.″5 is comparable to MaNGA's which means that we will be able to spatially resolve most of the pairs in our sample. X-ray is useful for AGN selection because it is less effected by AGN geometry and dust obscuration. Finally, we can use the previous radio surveys; NVSS (National Radio Astronomy Observatory (NRAO) Very Large Array Sky Survey; Condon et al. (1998)) and FIRST (Faint Images of the Radio Sky at Twenty centimeters; Becker,

White, and Helfand (1995)) to crossmatch with our AGN sample. These radio surveys are useful as they are not significantly affected by dust obscuration.

Follow-up observations may be particularly interesting for the dual broad-line AGN we found, Mrk 883. We were unable to separately resolve their spectra with MaNGA; however, follow-up observations with high resolution observatories like Chandra may be able to resolve the two cores and confirm that the object is or is not a dual broad-line AGN.

Many previous works study a sample of post-merger galaxies alongside a sample of paired galaxies. Due to the pair selection methodology that we employ, we have no post-merger galaxies in our sample. These galaxies are particularly interesting as simulations predict that some of the greatest nuclear activity will happen as the two galaxies coalesce into a single galaxy. Therefore, the inclusion of a post-merger sample would be valuable in constructing a more complete image of galaxy interactions.

I would like to acknowledge support from the National Science Foundation (NSF) grants; AST-1614326 and AST-2103251.

BIBLIOGRAPHY

Abdurro'uf et al. (Dec. 2021). "The Seventeenth Data Release of the Sloan Digital Sky Surveys: Complete Release of MaNGA, MaStar and APOGEE-2 Data". In: *arXiv e-prints*, arXiv:2112.02026, arXiv:2112.02026. arXiv: 2112.02026 [astro-ph.GA].

Abolfathi, Bela et al. (Apr. 2018). "The Fourteenth Data Release of the Sloan Digital Sky Survey: First Spectroscopic Data from the Extended Baryon Oscillation Spectroscopic Survey and from the Second Phase of the Apache Point Observatory Galactic Evolution Experiment". In: 235.2, 42, p. 42. DOI: 10.3847/1538-4365/aa9e8a. arXiv: 1707.09322 [astro-ph.GA].

Aguado, D. S. et al. (Feb. 2019). "The Fifteenth Data Release of the Sloan Digital Sky Surveys: First Release of MaNGA-derived Quantities, Data Visualization Tools, and Stellar Library". In: 240.2, 23, p. 23. DOI: 10.3847/1538-4365/aaf651. arXiv: 1812.02759 [astro-ph.IM].

Alonso, Sol et al. (Oct. 2018). "The impact of bars and interactions on optically selected AGNs in spiral galaxies". In: 618, A149, A149. DOI: 10.1051/0004-6361/201832796. arXiv: 1808.05536 [astro-ph.GA].

Antonucci, Robert (Jan. 1993). "Unified models for active galactic nuclei and quasars." In: 31, pp. 473–521. DOI: 10.1146/annurev.aa.31.090193.002353.

Athanassoula, E. (Apr. 2005). "On the nature of bulges in general and of box/peanut bulges in particular: input from N-body simulations". In: 358.4, pp. 1477–1488. DOI: 10.1111/j.1365-2966.2005.08872.x. arXiv: astro-ph/0502316 [astro-ph].

— (Oct. 2008). "Disc instabilities and semi-analytic modelling of galaxy formation". In: 390.1, pp. L69–L72. DOI: 10.1111/j.1745-3933.2008.00541.x. arXiv: 0808.0016 [astro-ph].

Baldwin, J. A., M. M. Phillips, and R. Terlevich (Feb. 1981). "Classification parameters for the emission-line spectra of extragalactic objects." In: 93, pp. 5–19. DOI: 10.1086/130766.

Ballo, L. et al. (Jan. 2004). "Arp 299: A Second Merging System with Two Active Nuclei?" In: 600.2, pp. 634–639. DOI: 10.1086/379887. arXiv: astro-ph/0306436 [astro-ph].

Barnes, Joshua E. and Lars Hernquist (Nov. 1996). "Transformations of Galaxies. II. Gasdynamics in Merging Disk Galaxies". In: 471, p. 115. DOI: 10.1086/177957.

Barnes, Joshua E. and Lars E. Hernquist (Apr. 1991). "Fueling Starburst Galaxies with Gas-rich Mergers". In: 370, p. L65. DOI: 10.1086/185978.

Barrera-Ballesteros, J. K. et al. (July 2015). "Central star formation and metallicity in CALIFA interacting galaxies". In: 579, A45, A45. DOI: 10.1051/0004-6361/201425397. arXiv: 1505.03153 [astro-ph.GA].

Becker, Robert H., Richard L. White, and David J. Helfand (Sept. 1995). "The FIRST Survey: Faint Images of the Radio Sky at Twenty Centimeters". In: 450, p. 559. DOI: 10.1086/176166.

Belfiore, Francesco et al. (Oct. 2019). "The Data Analysis Pipeline for the SDSS-IV MaNGA IFU Galaxy Survey: Emission-line Modeling". In: 158.4, 160, p. 160. DOI: 10.3847/1538-3881/ab3e4e. arXiv: 1901.00866 [astro-ph.GA].

Bianchi, Stefano et al. (May 2008). "Chandra unveils a binary active galactic nucleus in Mrk 463". In: 386.1, pp. 105–110. DOI: 10.1111/j.1365-2966.2008.13078.x. arXiv: 0802.0825 [astro-ph].

Bundy, Kevin et al. (Jan. 2015). "Overview of the SDSS-IV MaNGA Survey: Mapping nearby Galaxies at Apache Point Observatory". In: 798.1, 7, p. 7. DOI: 10.1088/0004-637X/798/1/7. arXiv: 1412.1482 [astro-ph.GA].

Burbidge, G. R. (June 1961). "Galactic Explosions as Sources of Radio Emission". In: 190.4781, pp. 1053–1056. DOI: 10.1038/1901053a0.

Calzetti, Daniela et al. (Apr. 2000). "The Dust Content and Opacity of Actively Star-forming Galaxies". In: 533.2, pp. 682–695. DOI: 10.1086/308692. arXiv: astro-ph/9911459 [astro-ph].

Capelo, Pedro R. et al. (Aug. 2017). "A survey of dual active galactic nuclei in simulations of galaxy mergers: frequency and properties". In: 469.4, pp. 4437–4454. DOI: 10.1093/mnras/stx1067. arXiv: 1611.09244 [astro-ph.GA].

Cappellari, Michele (Apr. 2017). "Improving the full spectrum fitting method: accurate convolution with Gauss-Hermite functions". In: 466.1, pp. 798–811. DOI: 10.1093/mnras/stw3020. arXiv: 1607.08538 [astro-ph.GA].

Cappellari, Michele and Eric Emsellem (Feb. 2004). "Parametric Recovery of Line-of-Sight Velocity Distributions from Absorption-Line Spectra of Galaxies via Penalized Likelihood". In: 116.816, pp. 138–147. DOI: 10.1086/381875. arXiv: astro-ph/0312201 [astro-ph].

Chandrasekhar, S. (Mar. 1943). "Dynamical Friction. I. General Considerations: the Coefficient of Dynamical Friction." In: 97, p. 255. DOI: 10.1086/144517.

Cid Fernandes, R. et al. (May 2011). "A comprehensive classification of galaxies in the Sloan Digital Sky Survey: how to tell true from fake AGN?" In: 413.3, pp. 1687–1699. DOI: 10.1111/j.1365-2966.2011.18244.x. arXiv: 1012.4426 [astro-ph.CO].

Cisternas, Mauricio et al. (Oct. 2013). "X-Ray Nuclear Activity in S^4G Barred Galaxies: No Link between Bar Strength and Co-occurrent Supermassive Black Hole Fueling". In: 776.1, 50, p. 50. DOI: 10.1088/0004-637X/776/1/50. arXiv: 1307.7709 [astro-ph.CO].

Comerford, Julia M. et al. (Aug. 2011). "Chandra Observations of a 1.9 kpc Separation Double X-Ray Source in a Candidate Dual Active Galactic Nucleus Galaxy at z = 0.16". In: 737.1, L19, p. L19. DOI: 10.1088/2041-8205/737/1/L19. arXiv: 1106.0746 [astro-ph.CO].

Comerford, Julia M. et al. (July 2012). "Kiloparsec-scale Spatial Offsets in Double-peaked Narrow-line Active Galactic Nuclei. I. Markers for Selection of Compelling Dual Active Galactic Nucleus Candidates". In: 753.1, 42, p. 42. DOI: 10.1088/0004-637X/753/1/42. arXiv: 1111.2862 [astro-ph.CO].

Comerford, Julia M. et al. (Nov. 2013). "Dual Supermassive Black Hole Candidates in the AGN and Galaxy Evolution Survey". In: 777.1, 64, p. 64. DOI: 10.1088/0004-637X/777/1/64. arXiv: 1309.2284 [astro-ph.CO].

Comerford, Julia M. et al. (June 2015). "Merger-driven Fueling of Active Galactic Nuclei: Six Dual and Offset AGNs Discovered with Chandra and Hubble Space Telescope

Observations". In: 806.2, 219, p. 219. DOI: 10.1088/0004-637X/806/2/219. arXiv: 1504.01391 [astro-ph.GA].

Comerford, Julia M. et al. (Nov. 2018). "The Origin of Double-peaked Narrow Lines in Active Galactic Nuclei. IV. Association with Galaxy Mergers". In: 867.1, 66, p. 66. DOI: 10.3847/1538-4357/aae2b4. arXiv: 1810.11543 [astro-ph.GA].

Condon, J. J. et al. (May 1998). "The NRAO VLA Sky Survey". In: 115.5, pp. 1693–1716. DOI: 10.1086/300337.

Crain, Robert A. et al. (June 2015). "The EAGLE simulations of galaxy formation: calibration of subgrid physics and model variations". In: 450.2, pp. 1937–1961. DOI: 10.1093/mnras/stv725. arXiv: 1501.01311 [astro-ph.GA].

Croom, Scott M. et al. (July 2021). "The SAMI Galaxy Survey: the third and final data release". In: 505.1, pp. 991–1016. DOI: 10.1093/mnras/stab229. arXiv: 2101.12224 [astro-ph.GA].

Di Matteo, P. et al. (June 2007). "Star formation efficiency in galaxy interactions and mergers: a statistical study". In: 468.1, pp. 61–81. DOI: 10.1051/0004-6361:20066959. arXiv: astro-ph/0703212 [astro-ph].

Drory, N. et al. (Feb. 2015). "The MaNGA Integral Field Unit Fiber Feed System for the Sloan 2.5 m Telescope". In: 149.2, 77, p. 77. DOI: 10.1088/0004-6256/149/2/77. arXiv: 1412.1535 [astro-ph.IM].

Ellison, Sara L. et al. (May 2008). "Galaxy Pairs in the Sloan Digital Sky Survey. I. Star Formation, Active Galactic Nucleus Fraction, and the Mass-Metallicity Relation". In: 135.5, pp. 1877–1899. DOI: 10.1088/0004-6256/135/5/1877. arXiv: 0803.0161 [astro-ph].

Ellison, Sara L. et al. (Dec. 2011). "Galaxy pairs in the Sloan Digital Sky Survey - IV. Interactions trigger active galactic nuclei". In: 418.3, pp. 2043–2053. DOI: 10.1111/j.1365-2966.2011.19624.x. arXiv: 1108.2711 [astro-ph.CO].

Ellison, Sara L. et al. (Nov. 2013). "Galaxy pairs in the Sloan Digital Sky Survey - VIII. The observational properties of post-merger galaxies". In: 435.4, pp. 3627–3638. DOI: 10.1093/mnras/stt1562. arXiv: 1308.3707 [astro-ph.CO].

Ellison, Sara L. et al. (Aug. 2019). "A definitive merger-AGN connection at z $\sim$ 0 with CFIS: mergers have an excess of AGN and AGN hosts are more frequently disturbed". In: 487.2, pp. 2491–2504. DOI: 10.1093/mnras/stz1431. arXiv: 1905.08830 [astro-ph.GA].

Evans, Ian N. et al. (July 2010). "The Chandra Source Catalog". In: 189.1, pp. 37–82. DOI: 10.1088/0067-0049/189/1/37. arXiv: 1005.4665 [astro-ph.HE].

Fabbiano, G. et al. (Sept. 2011). "A close nuclear black-hole pair in the spiral galaxy NGC3393". In: 477.7365, pp. 431–434. DOI: 10.1038/nature10364. arXiv: 1109.0483 [astro-ph.CO].

Fu, Hai et al. (June 2011). "Mergers in Double-peaked [O III] Active Galactic Nuclei". In: 733.2, 103, p. 103. DOI: 10.1088/0004-637X/733/2/103. arXiv: 1009.0767 [astro-ph.CO].

Fu, Hai et al. (Jan. 2012). "The Nature of Double-peaked [O III] Active Galactic Nuclei". In: 745.1, 67, p. 67. DOI: 10.1088/0004-637X/745/1/67. arXiv: 1107.3564 [astro-ph.CO].

Fu, Hai et al. (Apr. 2018). "SDSS-IV MaNGA: Galaxy Pair Fraction and Correlated Active Galactic Nuclei". In: 856.2, 93, p. 93. DOI: 10.3847/1538-4357/aab364. arXiv: 1801.00792 [astro-ph.GA].

Gao, F. et al. (May 2020). "Mergers trigger active galactic nuclei out to z $\sim$ 0.6". In: 637, A94, A94. DOI: 10.1051/0004-6361/201937178. arXiv: 2004.00680 [astro-ph.GA].

García-Benito, R. et al. (Apr. 2015). "CALIFA, the Calar Alto Legacy Integral Field Area survey. III. Second public data release". In: 576, A135, A135. DOI: 10.1051/0004-6361/201425080. arXiv: 1409.8302 [astro-ph.GA].

Glikman, Eilat et al. (June 2015). "Major Mergers Host the Most-luminous Red Quasars at z ~2: A Hubble Space Telescope WFC3/IR Study". In: 806.2, 218, p. 218. DOI: 10.1088/0004-637X/806/2/218. arXiv: 1504.02111 [astro-ph.GA].

Greenstein, Jesse L. (Mar. 1963). "Red-Shift of the Unusual Radio Source: 3C 48". In: 197.4872, pp. 1041–1042. DOI: 10.1038/1971041a0.

Hazard, C., M. B. Mackey, and A. J. Shimmins (Mar. 1963). "Investigation of the Radio Source 3C 273 By The Method of Lunar Occultations". In: 197.4872, pp. 1037–1039. DOI: 10.1038/1971037a0.

Heckman, Timothy M. and Philip N. Best (Aug. 2014). "The Coevolution of Galaxies and Supermassive Black Holes: Insights from Surveys of the Contemporary Universe". In: 52, pp. 589–660. DOI: 10.1146/annurev-astro-081913-035722. arXiv: 1403.4620 [astro-ph.GA].

Ho, L. C. (Sept. 2008). "Nuclear activity in nearby galaxies." In: 46, pp. 475–539. DOI: 10.1146/annurev.astro.45.051806.110546. arXiv: 0803.2268 [astro-ph].

Hopkins, Philip F. et al. (Mar. 2006). "A Unified, Merger-driven Model of the Origin of Starbursts, Quasars, the Cosmic X-Ray Background, Supermassive Black Holes, and Galaxy Spheroids". In: 163.1, pp. 1–49. DOI: 10.1086/499298. arXiv: astro-ph/0506398 [astro-ph].

Hopkins, Philip F. et al. (Apr. 2008). "A Cosmological Framework for the Co-Evolution of Quasars, Supermassive Black Holes, and Elliptical Galaxies. I. Galaxy Mergers and Quasar Activity". In: 175.2, pp. 356–389. DOI: 10.1086/524362. arXiv: 0706.1243 [astro-ph].

Hoyle, F. and W. A. Fowler (Jan. 1963a). "On the nature of strong radio sources". In: 125, p. 169. DOI: 10.1093/mnras/125.2.169.

Hoyle, F. and William A. Fowler (Feb. 1963b). "Nature of Strong Radio Sources". In: 197.4867, pp. 533–535. DOI: 10.1038/197533a0.

Jin, Gaoxiang et al. (Dec. 2021). "An IFU View of the Active Galactic Nuclei in MaNGA Galaxy Pairs". In: 923.1, 6, p. 6. DOI: 10.3847/1538-4357/ac2901. arXiv: 2109.11084 [astro-ph.GA].

Jogee, S. (2006). "The Fueling and Evolution of AGN: Internal and External Triggers". In: *Physics of Active Galactic Nuclei at all Scales*. Ed. by Danielle Alloin. Vol. 693, p. 143. DOI: 10.1007/3-540-34621-X_6.

Junkkarinen, V. et al. (Mar. 2001). "LBQS 0103-2753: A 0.3" Binary Quasar". In: 549.2, pp. L155–L159. DOI: 10.1086/319173. arXiv: astro-ph/0102501 [astro-ph].

Kauffmann, Guinevere and Martin Haehnelt (Jan. 2000). "A unified model for the evolution of galaxies and quasars". In: 311.3, pp. 576–588. DOI: 10.1046/j.1365-8711.2000.03077.x. arXiv: astro-ph/9906493 [astro-ph].

Kauffmann, Guinevere et al. (Dec. 2003). "The host galaxies of active galactic nuclei". In: 346.4, pp. 1055–1077. DOI: 10.1111/j.1365-2966.2003.07154.x. arXiv: astro-ph/0304239 [astro-ph].

Keel, William C. et al. (Mar. 2019). "AGN photoionization of gas in companion galaxies as a probe of AGN radiation in time and direction". In: 483.4, pp. 4847–4865. DOI: 10.1093/mnras/sty3332. arXiv: 1711.09936 [astro-ph.GA].

Kewley, L. J. et al. (July 2001). "Theoretical Modeling of Starburst Galaxies". In: 556.1, pp. 121–140. DOI: 10.1086/321545. arXiv: astro-ph/0106324 [astro-ph].

Komossa, S. et al. (Jan. 2003). "Discovery of a Binary Active Galactic Nucleus in the Ultraluminous Infrared Galaxy NGC 6240 Using Chandra". In: 582.1, pp. L15–L19. DOI: 10.1086/346145. arXiv: astro-ph/0212099 [astro-ph].

Kormendy, John and Luis C. Ho (Aug. 2013). "Coevolution (Or Not) of Supermassive Black Holes and Host Galaxies". In: 51.1, pp. 511–653. DOI: 10.1146/annurev-astro-082708-101811. arXiv: 1304.7762 [astro-ph.CO].

Kormendy, John and Jr. Kennicutt Robert C. (Sept. 2004). "Secular Evolution and the Formation of Pseudobulges in Disk Galaxies". In: 42.1, pp. 603–683. DOI: 10.1146/annurev.astro.42.053102.134024. arXiv: astro-ph/0407343 [astro-ph].

Law, David R. et al. (Oct. 2016). "The Data Reduction Pipeline for the SDSS-IV MaNGA IFU Galaxy Survey". In: 152.4, 83, p. 83. DOI: 10.3847/0004-6256/152/4/83. arXiv: 1607.08619 [astro-ph.IM].

Lee, Gwang-Ho et al. (May 2012). "Do Bars Trigger Activity in Galactic Nuclei?" In: 750.2, 141, p. 141. DOI: 10.1088/0004-637X/750/2/141. arXiv: 1203.1693 [astro-ph.CO].

Liang, E. P. T. and R. H. Price (Nov. 1977). "Accretion disk coronae and Cygnus X-1." In: 218, pp. 247–252. DOI: 10.1086/155677.

Liu, Xin, Yue Shen, and Michael A. Strauss (Jan. 2012). "Active Galactic Nucleus Pairs from the Sloan Digital Sky Survey. II. Evidence for Tidally Enhanced Star Formation and Black Hole Accretion". In: 745.1, 94, p. 94. DOI: 10.1088/0004-637X/745/1/94. arXiv: 1104.0951 [astro-ph.CO].

Liu, Xin et al. (May 2010). "Discovery of Four kpc-scale Binary Active Galactic Nuclei". In: 715.1, pp. L30–L34. DOI: 10.1088/2041-8205/715/1/L30. arXiv: 1003.3467 [astro-ph.CO].

Liu, Xin et al. (Aug. 2011). "Active Galactic Nucleus Pairs from the Sloan Digital Sky Survey. I. The Frequency on ~5-100 kpc Scales". In: 737.2, 101, p. 101. DOI: 10.1088/0004-637X/737/2/101. arXiv: 1104.0950 [astro-ph.CO].

Liu, Xin et al. (Jan. 2013). "Chandra X-Ray and Hubble Space Telescope Imaging of Optically Selected Kiloparsec-scale Binary Active Galactic Nuclei. I. Nature of the Nuclear Ionizing Sources". In: 762.2, 110, p. 110. DOI: 10.1088/0004-637X/762/2/110. arXiv: 1209.5418 [astro-ph.CO].

Lynden-Bell, D. (Aug. 1969). "Galactic Nuclei as Collapsed Old Quasars". In: 223.5207, pp. 690–694. DOI: 10.1038/223690a0.

Magorrian, John et al. (June 1998). "The Demography of Massive Dark Objects in Galaxy Centers". In: 115.6, pp. 2285–2305. DOI: 10.1086/300353. arXiv: astro-ph/9708072 [astro-ph].

Malkan, Matthew A., Varoujan Gorjian, and Raymond Tam (July 1998). "A Hubble Space Telescope Imaging Survey of Nearby Active Galactic Nuclei". In: 117.1, pp. 25–88. DOI: 10.1086/313110. arXiv: astro-ph/9803123 [astro-ph].

Mazzarella, J. M. et al. (Nov. 2012). "Investigation of Dual Active Nuclei, Outflows, Shock-heated Gas, and Young Star Clusters in Markarian 266". In: 144.5, 125, p. 125. DOI: 10.1088/0004-6256/144/5/125. arXiv: 1208.3248 [astro-ph.GA].

McAlpine, Stuart et al. (June 2020). "Galaxy mergers in EAGLE do not induce a significant amount of black hole growth yet do increase the rate of luminous AGN". In: 494.4, pp. 5713–5733. DOI: 10.1093/mnras/staa1123. arXiv: 2002.00959 [astro-ph.GA].

McGurk, R. C. et al. (Sept. 2015). "Spatially Resolved Imaging and Spectroscopy of Candidate Dual Active Galactic Nuclei". In: 811.1, 14, p. 14. DOI: 10.1088/0004-637X/811/1/14.

Mihos, J. Christopher and Lars Hernquist (June 1996). "Gasdynamics and Starbursts in Major Mergers". In: 464, p. 641. DOI: 10.1086/177353. arXiv: astro-ph/9512099 [astro-ph].

Momcheva, Ivelina G. et al. (Aug. 2016). "The 3D-HST Survey: Hubble Space Telescope WFC3/G141 Grism Spectra, Redshifts, and Emission Line Measurements for ~100,000 Galaxies". In: 225.2, 27, p. 27. DOI: 10.3847/0067-0049/225/2/27. arXiv: 1510.02106 [astro-ph.GA].

Montero-Dorta, Antonio D. and Francisco Prada (Nov. 2009). "The SDSS DR6 luminosity functions of galaxies". In: 399.3, pp. 1106–1118. DOI: 10.1111/j.1365-2966.2009.15197.x. arXiv: 0806.4930 [astro-ph].

Moran, Edward C. et al. (Sept. 1992). "WAS 49: Mirror for a Hidden Seyfert 1 Nucleus". In: 104, p. 990. DOI: 10.1086/116292.

Moreno, Jorge et al. (Apr. 2015). "Mapping galaxy encounters in numerical simulations: the spatial extent of induced star formation". In: 448.2, pp. 1107–1117. DOI: 10.1093/mnras/stv094. arXiv: 1501.03573 [astro-ph.GA].

Moreno, Jorge et al. (May 2021). "Spatially resolved star formation and fuelling in galaxy interactions". In: 503.3, pp. 3113–3133. DOI: 10.1093/mnras/staa2952. arXiv: 2009.11289 [astro-ph.GA].

Müller-Sánchez, F. et al. (Nov. 2015). "The Origin of Double-peaked Narrow Lines in Active Galactic Nuclei. I. Very Large Array Detections of Dual AGNs and AGN Outflows". In: 813.2, 103, p. 103. DOI: 10.1088/0004-637X/813/2/103. arXiv: 1509.04291 [astro-ph.GA].

Nelson, D. et al. (Nov. 2015). "The illustris simulation: Public data release". In: *Astronomy and Computing* 13, pp. 12–37. DOI: 10.1016/j.ascom.2015.09.003. arXiv: 1504.00362 [astro-ph.CO].

Nevin, R. et al. (Nov. 2016). "The Origin of Double-peaked Narrow Lines in Active Galactic Nuclei. II. Kinematic Classifications for the Population at z ¡ 0.1". In: 832.1, 67, p. 67. DOI: 10.3847/0004-637X/832/1/67. arXiv: 1609.04018 [astro-ph.GA].

Oke, J. B. (Mar. 1963). "Absolute Energy Distribution in the Optical Spectrum of 3C 273". In: 197.4872, pp. 1040–1041. DOI: 10.1038/1971040b0.

Owen, F. N. et al. (July 1985). "VLA observations of the multiple jet galaxy 3C 75." In: 294, pp. L85–L88. DOI: 10.1086/184514.

Pan, Hsi-An et al. (Aug. 2019). "SDSS-IV MaNGA: Spatial Evolution of Star Formation Triggered by Galaxy Interactions". In: 881.2, 119, p. 119. DOI: 10.3847/1538-4357/ab311c. arXiv: 1907.04491 [astro-ph.GA].

Perez, Josefa, Leo Michel-Dansac, and Patricia B. Tissera (Oct. 2011). "Chemical evolution during gas-rich galaxy interactions". In: 417.1, pp. 580–590. DOI: 10.1111/j.1365-2966.2011.19300.x. arXiv: 1106.4556 [astro-ph.CO].

Pillepich, Annalisa et al. (Mar. 2018). "First results from the IllustrisTNG simulations: the stellar mass content of groups and clusters of galaxies". In: 475.1, pp. 648–675. DOI: 10.1093/mnras/stx3112. arXiv: 1707.03406 [astro-ph.GA].

Powell, M. J. D. (Jan. 1964). "An efficient method for finding the minimum of a function of several variables without calculating derivatives". In: *The Computer Journal* 7.2, pp. 155–162. ISSN: 0010-4620. DOI: 10.1093/comjnl/7.2.155. eprint: https://academic.oup.com/comjnl/article-pdf/7/2/155/959784/070155.pdf. URL: https://doi.org/10.1093/comjnl/7.2.155.

Press, William H. et al. (2007). *Numerical Recipes 3rd Edition: The Art of Scientific Computing*. 3rd ed. Cambridge University Press. ISBN: 0521880688. URL: http://www.amazon.com/Numerical-Recipes-3rd-Scientific-Computing/dp/0521880688/ref=sr_1_1?ie=UTF8&s=books&qid=1280322496&sr=8-1.

Robotham, A. S. G. et al. (Nov. 2014). "Galaxy And Mass Assembly (GAMA): galaxy close pairs, mergers and the future fate of stellar mass". In: 444.4, pp. 3986–4008. DOI: 10.1093/mnras/stu1604. arXiv: 1408.1476 [astro-ph.GA].

Rodriguez, C. et al. (July 2006). "A Compact Supermassive Binary Black Hole System". In: 646.1, pp. 49–60. DOI: 10.1086/504825. arXiv: astro-ph/0604042 [astro-ph].

Rodriguez-Gomez, Vicente et al. (May 2016). "The stellar mass assembly of galaxies in the Illustris simulation: growth by mergers and the spatial distribution of accreted stars". In: 458.3, pp. 2371–2390. DOI: 10.1093/mnras/stw456. arXiv: 1511.08804 [astro-ph.GA].

Rubinur, K., M. Das, and P. Kharb (Apr. 2019). "Searching for dual AGN in galaxies with double-peaked emission line spectra using radio observations". In: 484.4, pp. 4933–4950. DOI: 10.1093/mnras/stz334. arXiv: 1902.00689 [astro-ph.GA].

Rupke, David S. N., Lisa J. Kewley, and L. H. Chien (Nov. 2010). "Gas-phase Oxygen Gradients in Strongly Interacting Galaxies. I. Early-stage Interactions". In: 723.2, pp. 1255–1271. DOI: 10.1088/0004-637X/723/2/1255. arXiv: 1009.0761 [astro-ph.GA].

Salpeter, E. E. (Aug. 1964). "Accretion of Interstellar Matter by Massive Objects." In: 140, pp. 796–800. DOI: 10.1086/147973.

Sánchez, S. F. et al. (Aug. 2017). "The mass-metallicity relation revisited with CALIFA". In: 469.2, pp. 2121–2140. DOI: 10.1093/mnras/stx808. arXiv: 1703.09769 [astro-ph.GA].

Sarzi, Marc et al. (Mar. 2006). "The SAURON project - V. Integral-field emission-line kinematics of 48 elliptical and lenticular galaxies". In: 366.4, pp. 1151–1200. DOI: 10.1111/j.1365-2966.2005.09839.x. arXiv: astro-ph/0511307 [astro-ph].

Satyapal, Shobita et al. (June 2014). "Galaxy pairs in the Sloan Digital Sky Survey - IX. Merger-induced AGN activity as traced by the Wide-field Infrared Survey Explorer". In: 441.2, pp. 1297–1304. DOI: 10.1093/mnras/stu650. arXiv: 1403.7531 [astro-ph.GA].

Schawinski, Kevin et al. (Dec. 2007). "Observational evidence for AGN feedback in early-type galaxies". In: 382.4, pp. 1415–1431. DOI: 10.1111/j.1365-2966.2007.12487.x. arXiv: 0709.3015 [astro-ph].

Schaye, Joop et al. (Jan. 2015). "The EAGLE project: simulating the evolution and assembly of galaxies and their environments". In: 446.1, pp. 521–554. DOI: 10.1093/mnras/stu2058. arXiv: 1407.7040 [astro-ph.GA].

Schmidt, M. (Mar. 1963). "3C 273 : A Star-Like Object with Large Red-Shift". In: 197.4872, p. 1040. DOI: 10.1038/1971040a0.

Schmidt, Maarten (Feb. 1968). "Space Distribution and Luminosity Functions of Quasi-Stellar Radio Sources". In: 151, p. 393. DOI: 10.1086/149446.

Scudder, Jillian M. et al. (Oct. 2012). "Galaxy pairs in the Sloan Digital Sky Survey - V. Tracing changes in star formation rate and metallicity out to separations of 80 kpc". In: 426.1, pp. 549–565. DOI: 10.1111/j.1365-2966.2012.21749.x. arXiv: 1207.4791 [astro-ph.CO].

Secrest, Nathan J. et al. (Feb. 2017). "Was 49b: An Overmassive AGN in a Merging Dwarf Galaxy?" In: 836.2, 183, p. 183. DOI: 10.3847/1538-4357/836/2/183. arXiv: 1612.03163 [astro-ph.GA].

Sellwood, J. A. (Jan. 2014). "Secular evolution in disk galaxies". In: *Reviews of Modern Physics* 86.1, pp. 1–46. DOI: 10.1103/RevModPhys.86.1. arXiv: 1310.0403 [astro-ph.GA].

Seyfert, Carl K. (Jan. 1943). "Nuclear Emission in Spiral Nebulae." In: 97, p. 28. DOI: 10.1086/144488.

Shah, Ekta A. et al. (Dec. 2020). "Investigating the Effect of Galaxy Interactions on the Enhancement of Active Galactic Nuclei at 0.5 ¡ z ¡ 3.0". In: 904.2, 107, p. 107. DOI: 10.3847/1538-4357/abbf59. arXiv: 2010.02710 [astro-ph.GA].

Shen, Yue et al. (July 2011). "Type 2 Active Galactic Nuclei with Double-peaked [O III] Lines. II. Single AGNs with Complex Narrow-line Region Kinematics are More Common than Binary AGNs". In: 735.1, 48, p. 48. DOI: 10.1088/0004-637X/735/1/48. arXiv: 1011.5246 [astro-ph.CO].

Silva, Andrea et al. (Mar. 2021). "Galaxy Mergers up to z ¡ 2.5. II. AGN Incidence in Merging Galaxies at Separations of 3-15 kpc". In: 909.2, 124, p. 124. DOI: 10.3847/1538-4357/abdbb1. arXiv: 2101.05000 [astro-ph.GA].

Silverman, J. D. et al. (Dec. 2011). "The Impact of Galaxy Interactions on Active Galactic Nucleus Activity in zCOSMOS". In: 743.1, 2, p. 2. DOI: 10.1088/0004-637X/743/1/2. arXiv: 1109.1292 [astro-ph.CO].

Skelton, Rosalind E. et al. (Oct. 2014). "3D-HST WFC3-selected Photometric Catalogs in the Five CANDELS/3D-HST Fields: Photometry, Photometric Redshifts, and Stellar Masses". In: 214.2, 24, p. 24. DOI: 10.1088/0067-0049/214/2/24. arXiv: 1403.3689 [astro-ph.GA].

Smith, K. L. et al. (June 2010). "A Search for Binary Active Galactic Nuclei: Double-peaked [O III] AGNs in the Sloan Digital Sky Survey". In: 716.1, pp. 866–877. DOI: 10.1088/0004-637X/716/1/866. arXiv: 0908.1998 [astro-ph.CO].

Smith, K. L. et al. (June 2012). "Double-peaked Narrow-line Active Galactic Nuclei. II. The Case of Equal Peaks". In: 752.1, 63, p. 63. DOI: 10.1088/0004-637X/752/1/63.

Stasińska, G. et al. (Nov. 2008). "Can retired galaxies mimic active galaxies? Clues from the Sloan Digital Sky Survey". In: 391.1, pp. L29–L33. DOI: 10.1111/j.1745-3933.2008.00550.x. arXiv: 0809.1341 [astro-ph].

Stasińska, Grażyna et al. (Sept. 2006). "Semi-empirical analysis of Sloan Digital Sky Survey galaxies - III. How to distinguish AGN hosts". In: 371.2, pp. 972–982. DOI: 10.1111/j.1365-2966.2006.10732.x. arXiv: astro-ph/0606724 [astro-ph].

Steffen, Joshua L. et al. (Mar. 2021). "SDSS-IV MaNGA: The Radial Profile of Enhanced Star Formation in Close Galaxy Pairs". In: 909.2, 120, p. 120. DOI: 10.3847/1538-4357/abe2a5. arXiv: 2102.03398 [astro-ph.GA].

Stockton, Alan et al. (Jan. 2004). "Two Active Nuclei in 3C 294". In: 600.2, pp. 626–633. DOI: 10.1086/380096. arXiv: astro-ph/0310107 [astro-ph].

Thorp, Mallory D. et al. (Jan. 2019). "Spatially resolved star formation and metallicity profiles in post-merger galaxies from MaNGA". In: 482.1, pp. L55–L59. DOI: 10.1093/mnrasl/sly185. arXiv: 1810.00897 [astro-ph.GA].

Torrey, Paul et al. (Feb. 2012). "The Metallicity Evolution of Interacting Galaxies". In: 746.1, 108, p. 108. DOI: 10.1088/0004-637X/746/1/108. arXiv: 1107.0001 [astro-ph.GA].

Ueda, Yoshihiro et al. (Dec. 2003). "Cosmological Evolution of the Hard X-Ray Active Galactic Nucleus Luminosity Function and the Origin of the Hard X-Ray Background". In: 598.2, pp. 886–908. DOI: 10.1086/378940. arXiv: astro-ph/0308140 [astro-ph].

Urrutia, Tanya, Mark Lacy, and Robert H. Becker (Feb. 2008). "Evidence for Quasar Activity Triggered by Galaxy Mergers in HST Observations of Dust-reddened Quasars". In: 674.1, pp. 80–96. DOI: 10.1086/523959. arXiv: 0709.2805 [astro-ph].

Van Wassenhove, Sandor et al. (Mar. 2012). "Observability of Dual Active Galactic Nuclei in Merging Galaxies". In: 748.1, L7, p. L7. DOI: 10.1088/2041-8205/748/1/L7. arXiv: 1111.0223 [astro-ph.CO].

Vazdekis, A. et al. (July 2012). "MIUSCAT: extended MILES spectral coverage - I. Stellar population synthesis models". In: 424.1, pp. 157–171. DOI: 10.1111/j.1365-2966.2012.21179.x. arXiv: 1205.5496 [astro-ph.CO].

Veilleux, S. et al. (Aug. 2009). "A Deep Hubble Space Telescope H-Band Imaging Survey of Massive Gas-Rich Mergers. II. The QUEST QSOs". In: 701.1, pp. 587–606. DOI: 10.1088/0004-637X/701/1/587. arXiv: 0906.3157 [astro-ph.CO].

Wake, David A. et al. (Sept. 2017). "The SDSS-IV MaNGA Sample: Design, Optimization, and Usage Considerations". In: 154.3, 86, p. 86. DOI: 10.3847/1538-3881/aa7ecc. arXiv: 1707.02989 [astro-ph.GA].

Wang, Jian-Min et al. (Nov. 2009). "Active Galactic Nuclei with Double-Peaked Narrow Lines: Are they Dual Active Galactic Nuclei?" In: 705.1, pp. L76–L80. DOI: 10.1088/0004-637X/705/1/L76. arXiv: 0910.0580 [astro-ph.CO].

Westfall, Kyle B. et al. (Dec. 2019). "The Data Analysis Pipeline for the SDSS-IV MaNGA IFU Galaxy Survey: Overview". In: 158.6, 231, p. 231. DOI: 10.3847/1538-3881/ab44a2. arXiv: 1901.00856 [astro-ph.GA].

Weston, Madalyn E. et al. (Feb. 2017). "Incidence of WISE -selected obscured AGNs in major mergers and interactions from the SDSS". In: 464.4, pp. 3882–3906. DOI: 10.1093/mnras/stw2620. arXiv: 1609.04832 [astro-ph.GA].

Wright, Edward L. et al. (Dec. 2010). "The Wide-field Infrared Survey Explorer (WISE): Mission Description and Initial On-orbit Performance". In: 140.6, pp. 1868–1881. DOI: 10.1088/0004-6256/140/6/1868. arXiv: 1008.0031 [astro-ph.IM].

Zeldovich, Ya. B. (1964). "The Fate of a Star, and the Liberation of Gravitation Energy in Accretion". In: *Dokl. Akad. Nauk SSSR* 155, p. 67.

Zhou, Hongyan et al. (Mar. 2004). "Obscured Binary Quasar Cores in SDSS J104807.74 +005543.5?" In: 604.1, pp. L33–L36. DOI: 10.1086/383310. arXiv: astro-ph/0411167 [astro-ph].